# Optical and electronic properties of graphene quantum dots in the Terahertz spectral range

Sylvain Massabeau

LPENS
LABORATOIRE DE PHYSIQUE
DE L'ÉCOLE NORMALE SUPÉRIEURE

SORBONNE
UNIVERSITÉS

**THÈSE DE DOCTORAT**
**DE SORBONNE UNIVERSITÉS**

**Spécialité : Physique**

**École doctorale nº397: Physique et chimie des matériaux**

**réalisée**

**au Laboratoire de Physique de l'Ecole Normale Supérieure**

**sous la direction de Juliette MANGENEY**

**présentée par**


# Sylvain Massabeau


**pour obtenir le grade de :**

**DOCTEUR DE SORBONNE UNIVERSITÉS**

**Sujet de la thèse :**

# Optical and electronic properties of graphene quantum dots in the Terahertz spectral range

**soutenue le 24 Novembre 2020**

**devant le jury composé de :**

| | | |
|---|---|---|
| M. | Frederic TEPPE | Rapporteur |
| M. | Christoph STAMPFER | Rapporteur |
| Ms. | Claire BERGER | Examinatrice |
| M. | Nicolas REGNAULT | Examinateur |
| Ms. | Valia VOLIOTIS | Examinatrice |
| M. | Daniel DOLFI | Examinateur |
| Ms. | Juliette MANGENEY | Directrice de thèse |
| M. | Kazuhiko HIRAKAWA | Membre invité |

# Remerciements

Au-delà de l'aspect scientifique, il est clair et indéniable que cette thèse n'aurait pu être ce qu'elle est sans le soutien de nombreuses personnes, que je me dois de remercier chaleureusement.

Dans un premier temps, je remercie évidemment Juliette Mangeney, ma directrice de thèse. J'ai tout de suite apprécié l'ambiance de travail dans l'équipe lorsque je suis arrivé en stage en 2016, ce qui m'a convaincu de poursuivre pour une thèse. Je ne peux que remercier mille fois Juliette pour son encadrement de haut niveau, pour la liberté scientifique qu'elle m'a accordée lors de mon/notre travail ensemble, les nombreuses collaborations scientifiques que j'ai pu effectuer grâce à elle, ainsi que pour sa bonne humeur, ses encouragements dans "le(s) creux de la vague" et pour le plaisir que j'avais au quotidien de travailler avec elle.
Il s'ensuit que je remercie également tous les membres de l'équipe (les chefs, ou plutôt permanents comme on dit): Jérôme, Sukhdeep, Nicolas, Robson et Louis-Anne. Je sais que j'ai eu beaucoup de chance de tomber sur une équipe aussi chaleureuse et qualifiée que la vôtre, je vous en remercie !
Viennent maintenant mes camarades de galère, et pour commencer les post-docs: Hanond, Kenneth, Niloufar et bien sûr, ma post-doc préférée: Elisa, qui a littéralement sauvé ma thèse grâce aux réseaux d'anniversaire qu'elle m'a offert. Passons maintenant aux thésards, et d'abord "les anciens": Matthieu qui m'a formé et avec qui j'ai passé de supers moments, ainsi que Sarah, toujours de bonne humeur et qui m'a super bien accueilli lors de mon arrivée. La nouvelle génération enfin: PanHui mon co-bureau avec qui j'ai vécu de folles aventures au Japon, Valentino qui a comme PanHui commencé en même temps que moi et avec qui j'ai vécu de folles aventures à Paris, Jacques, avec qui j'ai vécu de folles aventures tout court, Chao, et la Dream Team THz: Simon, Romaine et Thibault, mon poulain. Merci à vous tous, ce fut un plaisir de partager votre quotidien pendant toutes ces années.
Je remercie finalement tous les autres membres du laboratoire avec qui j'ai partagé des bons moments, à la fois pour le boulot ainsi qu'autour de la machine à café/autre, pêle-mêle: Romaric, Théo, Matthieu, Holger, Gauthier, Raphaël, Pascal, Aurélie, Michaël, José, Anne et Olga.

Lors de ce long voyage de 4 ans, de nombreuses autres personnes dans mon entourage m'ont apporté leur soutien, et je tiens aussi à les remercier.
La mafia marseillaise à Paris pour commencer: Faris, Galli, Arthur, Benoît, Manon et Marion, ainsi que mes très chers Gabou, Matthieu et Alexandre. Nous sommes venus, nous avons vaincu !
Toute cette aventure a commencé alors que je me trouvais dans un environnement tout à fait propice au travail, j'ai nommé la Collow'd ! Je remercie tout particulièrement mon bibi, qui m'accompagne depuis mon arrivée à Paris, c'est bien sûr Aziz (ou Jean-Aziz depuis pas très longtemps). Cher bibi, j'ai l'impression que notre objectif avant de commencer notre thèse a été très largement rempli ! Viennent ensuite les autres membres de la coloc, passé,

présent et futur, en ordre quasi-chronologique: Thibault, Amaury et Célia (mention spéciale en tant que pères et mère fondateurs), Adrien, Tony, Théo, Jacques, Arthur (double remerciement du coup), et Ségo. Mention spéciale à Tony, dont les précieux conseils lors de la dernière ligne droite de ma rédaction m'ont permis de débloquer la situation et ainsi tracer de merveilleuses courbes aux résultats très intéressants, merci à toi !
Pour finir sur la partie "Paris", je termine avec toutes les personnes qui m'ont accompagné ces dernières années: Amine, Acil, Lina, Marie, Lucie, Wei, Setsen, Antoine, Jérôme, David, Théophile, ainsi que tous mes amis de l'ESPCI que je ne peux citer ici (ça va coûter trop cher à l'impression).

Passons maintenant à l'avant dernière partie de mes remerciements: tous mes amis de Marseille qui m'ont soutenu malgré la distance. Pour commencer Guillaume, qui m'a fait l'honneur d'être tout le temps disponible dès lors que j'étais de retour à la mère-patrie, et qui est venu me voir à Paris de nombreuses fois, un très grand merci mon pote ! Puis viennent Thibault et Amandine, je suis tellement heureux de votre soutien également, j'avais besoin de vous voir à chaque fois que je revenais, et aussi merci d'avoir donné de votre temps pour être présent à ma soutenance ! Egalement Yoann et Lionel, que j'ai malheureusement dû abandonner dans notre aventure musicale, mais qui malgré cela ont toujours été présents, un grand merci !
Et enfin, toute la bande des scouts: Lucie, Oncle Vince, Camille, Victor, Robin, Nathan, Nico, Margot, Arnaud, Romane, Alice, Pierrot, toutes les Sophie, Alice, Julia, le David, Jubi, Clem, Fab', Laurène et tous les autres. Vous revoir à chaque fois que j'étais sur Marseille a été d'un très très grand soutien pour moi, un soutien indispensable je pense. C'était des moments inoubliables, qui m'ont donné de la force pour finir cette thèse, merci mille fois !

Et bien sûr, pour terminer, je remercie très affectueusement ma famille: mes parents et mon frère Rémy. Mes parents m'ont mis au monde, et mon frère m'a accompagné ces 25 dernières années. Ils ont été d'un soutien sans faille lors de mon doctorat, et je suis heureux de pouvoir passer plus de temps avec eux maintenant que j'ai fini. Un très grand merci à vous trois, je vous aime.

Et maintenant, bonne lecture !

# Introduction

It is quite surprising to think that for almost 500 years after the invention of the pencil, whose lead is made of graphite, almost everyone had in their hands a material that was going to be the subject of almost 2 million publications. Four centuries later, the first diffraction measurements of this three-dimensional allotrope of carbon revealed its lamellar structure. Although graphite did not seem to exhibit any particular electronic properties, the first theoretical work [1] by P. R. Wallace in 1946 indicated that it would be quite different if it were possible to isolate an atomically-thick layer. His works on band theory applied to a graphite monolayer – graphene – were subsequently completed by other theoretical studies [2, 3] and observations. It was however at this time rather difficult to experimentally isolate a monolayer graphene from graphitic clusters to properly examine its properties.

This technological barrier was finally crossed in 2004 by Geim and Novoselov, whose work was awarded the Nobel Prize in Physics in 2010. By mechanical exfoliation of graphite, they obtained large samples (several tens of $\mu$m) of high quality graphene [4]. The control of the manufacturing process was subsequently supplemented by other techniques, as for example chemical vapor deposition [5] or epitaxial growth on silicon carbide [6]. It allowed the fabrication of stable graphene samples, thus paving the way to different characterizations – optical, electronic, magnetic – of graphene.

The wide variety of physical properties of this material mainly derives from its crystalline structure. Graphene is made up of a monoatomic layer of carbon atoms arranged on a honeycomb structure made of hexagons, with 2 carbon atoms per unit cell. On each atom, three electrons occupy the hybrid orbitals $sp^2$, shared with its three neighboring carbon atoms, thus forming $\sigma$-bonds which give graphene its remarkable mechanical properties (Young's modulus $\sim 1$ TPa [7]). The last electron occupies the $sp^2$ orbital, perpendicular to the plane of graphene. These $sp^2$ orbitals between neighboring atoms hybridize to form two $\pi$-bands, which are responsible for most of the electronic properties of graphene.

Indeed, the hexagonal crystalline structure of graphene leads to a linear low energy band, in contrast with the parabolic structure observed in most semiconductors. It follows that the electrons which occupy this band are quasi-relativistic, i.e. they behave like massless fermions, which can move at a speed $v_F = c/300 \sim 10^6\ m.s^{-1}$ comparable to that of photons. By analogy with the Dirac equation describing such relativistic particles, these electrons are called Dirac fermions. This results in the observation of a number of very peculiar electronic properties such as fractional quantum Hall effect [8, 9], ballistic transport properties on a micron scale [10] and Klein tunnelling [11].

Graphene also has a very broadband optical response. A single monoatomic layer of graphene leads to an absorption of 2.3% of light from visible to infrared [12]. The absence of gap in graphene and the linear dispersion of low energy electrons also implies that interband tran-

sitions can be induced by Terahertz (THz) radiation, i.e. low energy photons of a few meV. Therefore, graphene uniquely matches the semiconductor-laser model for THz generation. This makes graphene a very promising material to support the development of the THz technology that severely lacks of compact powerful sources. This perspective has stimulated intensive experimental and theoretical works that have lead to the demonstration of population inversion and optical gain in graphene under intense optical excitation, suggesting that THz lasing may be possible [13]. However, the lifetime of the optical gain in monolayer graphene is limited to a few hundreds of femtoseconds due to non-radiative processes, in particular Auger recombination that dominate the carrier dynamics [14]. Auger recombination is a scattering process in which the recombination of an electron–hole pair pushes another electron to higher energies. This short-lived optical gain in graphene is detrimental for the development of THz lasers. Nonetheless, this process can be cancelled by limiting the available final states for the scattered electron.

The strategy carried out by my research team is to realize the full discretization of electronic states through graphene quantum dots (GQDs) with the aim to inhibit Auger recombination processes. Besides, graphene is a semi-metal, which constitutes a severe limitation for many applications. This issue can be overcome in GQDs as a band gap opens up owing to the quantum confinement. That is why GQDs have raised considerable interest in nanoelectronics and optics. Finally, GQDs exhibit interesting phenomena due to quantum confinement and edge effects.

The aim of the present thesis is to investigate the electronic and optical properties in the THz spectral range of GQDs with diameters of few tens of nanometers.

When graphene dimensions are reduced to a few nanometers in all directions of the plane, the De Broglie wavelength of the charge carriers becomes comparable to the dimensions of the structure. Such quasi-zero-dimensional nanostructures are called GQDs. Since the electrons are confined in all three directions of space, the energy levels of the GQD become completely discrete, as in an isolated atom. These "artificial atoms" are of great interest because of their adjustable properties. Indeed, for a GQD of typical size $D$, the boundary conditions of the wavefunction gives an estimation of the interlevel spacing $\Delta E \propto \hbar v_F/D$. Thus, one can vary the size of a GQD from a few nm to several tens of nm in order to tune $\Delta E \sim 1\ eV - 1\ meV$ and explore its interaction (absorption, emission) with photons of energies covering the whole electromagnetic spectrum (see Figure 1).

In the case of small GQDs of few nanometers, the interlevel spacing $\Delta E$ is about few eV, i.e. in the visible and near infrared range. Due to their very small size, these materials can be manufactured in a controlled manner by bottom-up synthesis and their edges can be selectively functionalized. Their optical properties can also be precisely determined due to the wide variety of instruments operating in the visible and infrared range. Finally, it is possible to support the experimental data by various quantum computation methods, since these structures have only few carbon atoms. An example of the high potential of small GQDs is the recent demonstration of single optical photon emission from a GQD of about 2 nm at room temperature [15].

Larger GQDs have been less investigated mainly because the number of atoms becomes too large to use *ab initio* calculation methods and also because their fabrication requires top-down techniques that do not allow to control neither the size nor the chemical nature of the edges of the quantum dots. In spite of this, simpler theoretical models of large GQDs

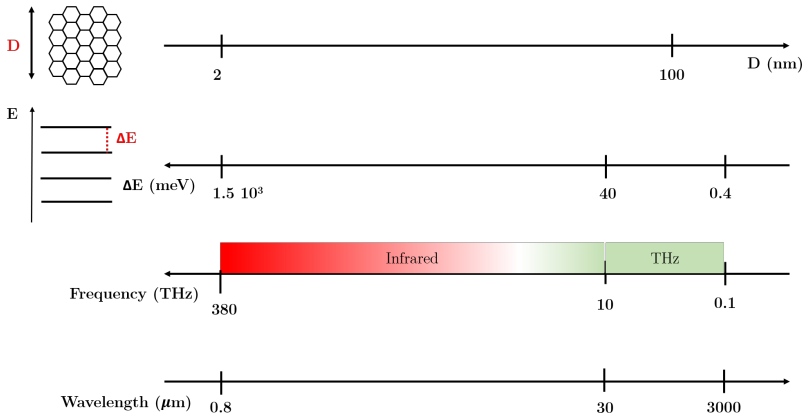


Figure 1: *Sketch of the evolution of the typical interlevel spacing $\Delta E$ of a graphene quantum dot of size $D$. Below the $\Delta E$ axis is shown the frequency (in THz) and the wavelength (in $\mu m$) of an electromagnetic wave of energy $\Delta E$. While increasing the GQD size from few nm to few tens of nm, its typical interlevel spacing is shifted from infrared to THz frequencies.*

have been carried out, revealing a rich variety of effects from these original objects [16]. The GQD shape and the structure of its edges – difficult to control experimentally at this scale – become critical boundary conditions that modify the discrete energy spectrum. A main effect is the existence of localized wavefunctions at the edges of the nanostructure. However, very few works have been reported on the optical properties of the large GQDs. Most of the studies focus on small GQDs ($D < 10\ nm$) and fixed geometries [17].

When the GQD size reaches several tens of nanometers, the separation between its discrete energy levels reaches the few meV range and therefore absorption in the THz spectral range may be achievable. Large GQDs are thus very promising candidates for the development of THz lasers and THz detectors. Indeed, as discussed previously, non-radiative Auger recombination processes, which inhibit the development of THz lasers, could be reduced by the energy level discretization. Moreover, the opening of a gap on the order of meV could reduce the Zener Klein dark current that limit performances of graphene-based photodetectors [18, 19].

Extrapolating the optical properties of small GQDs to get an accurate description of these large GQDs is however difficult. For instance, the edge effects are expected to play a distinct role on the electronic structure of GQDs as their size increases [20] and also can contribute to light-matter interaction in contrast to small GQDs. Secondly, the electron distribution – the doping – drives optical absorption at low energy, in contract to small GQDs. Finally, it becomes experimentally difficult to probe the optical properties of large GQDs at THz frequencies, as the wavelength of the electromagnetic field is extremely large compared to the size of the dot ($\lambda_{THz} \sim 1\ mm - 30\ \mu m \gg 10 - 100\ nm$).

In this thesis, we study experimentally and theoretically the electronic states and the optical absorption in the THz spectral range of these original large GQDs. For the fabrication, we use both exfoliated graphene and epitaxially grown graphene performed by C. Berger and W. de Heer (Atlanta). For the theoretical investigation, we have calculated the electronic state distribution and the absorption probability using a tight-binding modelling. Then, we experimentally probe the absorption properties of arrays of GQDs using THz time-domain spectroscopy experiments. The GQDs were fabricated from epitaxially grown graphene, which allows large dimensions with a high number of layers. Finally, we perform transport

spectroscopy measurements of a single GQD under THz illumination. These single GQDs were made from exfoliated graphene, as the technique provides monolayer graphene of very high quality (low disorder, high mobility) that is critical for studying a single GQD.

The present thesis is organized in three chapters:

**Chapter 1** is devoted to the theoretical investigation of electronic and optical properties of large GQDs based on a tight-binding modelling. We calculate the energy levels of GQDs of diameters ranging from 6 to 50 nm and analyse the different nature of the energy states. We further calculate the coupling of these energy levels to low energy photons and determine the absorption probability spectra in the THz spectral range. We finally explore how the size, the temperature and the doping of the GQDs affect their absorption spectra. This study has been performed in close collaboration with Robson Ferreira and Nicolas Regnault (Theory of Condensed Matter at LPENS).

**Chapter 2** describes an in-depth investigation of the interband and intraband conductivity of multilayer epitaxial graphene performed using THz-TDS system. Then, we present the fabrication of GQDs arrays and the absorption spectra at THz frequencies obtained by THz time-domain spectroscopy measurements. These results are then compared to the theoretical predictions of Chapter 1.

**Chapter 3** is devoted to the measurement of the dark quantum transport in a single GQD and of the photo-transport under incoherent THz illumination. We first present the fabrication process of a single GQD inserted within single electron transistors coupled to a bow-tie THz antenna. We then report dark transport measurements in the GQD-based transistors that show Coulomb blockade regime and excited states of the GQD. Finally, we provide the photoresponse of the GQD in the Coulomb blockade regime under incoherent THz illumination. This study has been performed in close collaboration with Takis Kontos and Sebastien Balibar (Mesoscopic Physic's group at LPENS).

# Contents

# Chapter 1

# Graphene quantum dots modelling

This chapter presents the electronic structures and the optical absorption of graphene quantum dots (GQDs) with diameter of few tens of nanometers, which are very promising for the development of innovative THz devices. I first present a description of our calculation based in nearest-neighbor tight-binding model. A main originality of our approach is to not impose any condition on the edge shape for a closer description of fabricated GQDs as fabrication process of GQDs does not allow the exact control of their edge shape. Based on our calculation, we explore the complex electronic structure of GQDs of various radii and identify three main types of energy states: edge states, mixed states and bulk states. We further calculate the coupling of these energy levels to low energy photons. We demonstrate that intraband transitions dominate the absorption spectra, resulting in a large absorption resonance in the few tens of meV range. Based on our calculation results, we explore how the size, the temperature and the doping of the GQDs affect their absorption spectra. This study has been performed in close collaboration with Robson Ferreira and Nicolas Regnault (Theory of Condensed Matter at LPENS).

## 1.1 Theoretical studies of GQDs

During the past decade, a steady rise of interest has been devoted to GQDs owing to the possibility of engineering their energy spectrum and therefore their optical properties. GQDs are very promising for several applications in fields ranging from quantum computation to biosensing and solar energy [21] [22]. These on going research is largely supported by the important advances in GQD fabrication [23].

Regarding theoretical studies, most of the works were carried out on small GQDs with absorption peaks in the optical or mid-infrared spectral ranges [24]. These studies have revealed that the energy dispersion as well as the optical conductivity in such small fractions of graphene strongly depends on the size, the shape and the edge structures [25], [17], [26], [27], as illustrated in Figure 1.1. In particular, the optical absorption spectra are red-shifted with the increasing sizes of the GQD [28], [29]. The absorption spectrum of GQDs with zigzag edges shows distinct features from the one of GQDs with armchair edges as bound edge state at zero energy appears only for GQDs with zigzag edges [17]. Also, studies on disordered GQDs have shown that they support a number of edge states proportional to circumference of the dot [20]. An analysis on the effect of edge distortion on the optical properties of GQDs have demonstrated their weak influence that moreover vanishes with GQD size increasing [26]. Besides, the investigation of GQDs in the presence of a perpendicular magnetic field have highlighted the transition from the linear density of states at B=0 to the Landau-level regime at high fields [30] and the possibility to tune the optical properties of the GQDs by an

external magnetic field [31], [32], [33]. As well, the dependence of the optical selection rules of a small GQD in external electric fields has been reported [34]. In addition, a redshift or blueshift of the absorption peaks can be observed in the optical spectrum by uniaxial tensile or compressive strain [35].

In spite of this intensive work on small GQDs, very little work has been reported on the electronic and the optical properties of GQDs of diameters of up to few tens of nanometers. This attribute to the difficulty of computing GQD composed by typically $10^5$ atoms. Moreover, studies on more realistic case of GQD with random termination, where, in principle, both the armchair and zigzag edge geometries coexist remains elusive.

The work presented in this chapter goes beyond the state of the art by reporting new insights on the electronic state distribution and the associated wavefunctions of GQDs with a diameter of few tens of nanometers and also on their coupling to low energy photons.

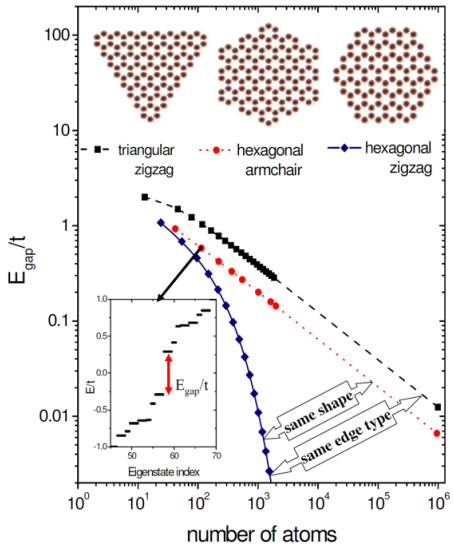


Figure 1.1: *Tight-binding bandgap energy as a function of total number of atoms N for a triangular zigzag quantum dot (dashed line with black squares), hexagonal armchair quantum dot (dotted line with circles), and hexagonal zigzag quantum dot (solid line with diamonds). The inset shows the tight-binding energy spectrum in the vicinity of the Fermi level for the hexagonal armchair dot. From reference [29].*

## 1.2 Tight-binding model

### 1.2.1 Infinite graphene sheet

Graphene is composed by carbon atoms arranged in space in a hexagonal lattice of parameter $a = 0.142\ nm$, as represented in Figure 1.2, with the notations used in the following chapter. Neighbouring atoms are bound by covalent bonds between the $sp^2$ hybrid orbitals of carbon. The remaining electrons, one per atom of the lattice, occupy the $p_z$ orbitals, where z is the axis perpendicular to the graphene plane. The hexagonal lattice is not a Bravais lattice. Nevertheless, we can define it as two interlaced triangular sublattices A and B. The graphene Bravais lattice unit cell thus contains 2 carbon atoms A and B, separated by the vector

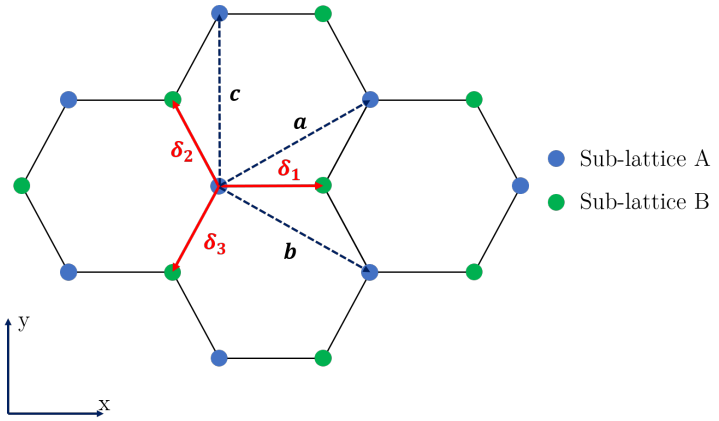


Figure 1.2: *Sketch of the hexagonal lattice of graphene. Atoms constitutive of the sublattices A and B are depicted in blue and green, respectively. Vectors* $\boldsymbol{\delta}_1$, $\boldsymbol{\delta}_2$ *and* $\boldsymbol{\delta}_3$ *between nearest neighbor atoms (red arrows) and* $\mathbf{a}$, $\mathbf{b}$ *and* $\mathbf{c}$ *between next-nearest neighbor atoms (dark arrows) are also represented.*

$\boldsymbol{\delta}_1 = (a, 0)$. The basis vectors are:

$$\mathbf{a} = \left(\frac{3a}{2}, \frac{\sqrt{3}a}{2}\right) \quad \text{and} \quad \mathbf{b} = \left(\frac{3a}{2}, -\frac{\sqrt{3}a}{2}\right)$$

We describe the graphene properties within the framework of the tight binding model: the electrons located on the $p_z$ orbitals can hop between the different neighbour sites of the hexagonal lattice, with an amplitude related to the inter-site coupling energy $t = 2.8\ eV$. We restrict our study only to the nearest neighbour interaction. In order to get the band structure of graphene, we use the Bloch theorem to find the stationnary states of the Schrödinger equation $H|\psi_{\mathbf{k}}(\mathbf{r})\rangle = \epsilon_{\mathbf{k}}|\psi_{\mathbf{k}}(\mathbf{r})\rangle$ on the form [1, 36]:

$$|\psi_{\mathbf{k}}(\mathbf{r})\rangle = \alpha_{\mathbf{k}}^A|\psi_{\mathbf{k}}^A(\mathbf{r})\rangle + \alpha_{\mathbf{k}}^B|\psi_{\mathbf{k}}^B(\mathbf{r})\rangle$$

The wave functions $|\psi_{\mathbf{k}}^A(\mathbf{r})\rangle$ and $|\psi_{\mathbf{k}}^B(\mathbf{r})\rangle$ are defined by:

$$|\psi_{\mathbf{k}}^A(\mathbf{r})\rangle = \frac{1}{\sqrt{N}} \sum_{\mathbf{R}=n\mathbf{a}+m\mathbf{b}} e^{i\mathbf{k}.\mathbf{R}}|\phi(\mathbf{r}-\mathbf{R})\rangle$$

$$|\psi_{\mathbf{k}}^B(\mathbf{r})\rangle = \frac{1}{\sqrt{N}} \sum_{\mathbf{R}=n\mathbf{a}+m\mathbf{b}} e^{i\mathbf{k}.\mathbf{R}}|\phi(\mathbf{r}-\mathbf{R}-\boldsymbol{\delta}_1)\rangle$$

where $\phi$ is the $p_z$ orbital wavefunction and N the number of unit cells of the lattice. The matrix elements of the aforementioned Hamiltonian are thus:

$$\begin{cases} \langle\phi(\mathbf{r})|H|\phi(\mathbf{r})\rangle = E_0 \\ \\ \langle\phi(\mathbf{r})|H|\phi(\mathbf{r}-\boldsymbol{\delta}_i)\rangle = -t \simeq -2.8\ eV \end{cases} \tag{1.1}$$

By restricting the tight-binding approach only to the nearest neighbours, the orbital wavefunctions overlapping terms $\langle\phi(\mathbf{r})|\phi(\mathbf{r}-\boldsymbol{\delta}_i)\rangle$ between neighbours and the matrix elements of H between atoms separated by more than $a$ are neglected. We can also redefine the problem by setting $E_0 = 0$, and thus rewrite the Hamiltonian of the system using the second quantization formalism:

$$\widehat{H} = -t \sum_{\langle i,j\rangle} \left[\hat{c}_i^\dagger \hat{c}_j + h.c.\right] \tag{1.2}$$

The sum is here indexed on nearest neighbours. One can still write the Hamiltonian by summing on the vectors $\mathbf{r}_A$ of the sub-lattice A:

$$\widehat{H} = -t \sum_{\mathbf{r}_A} \sum_{\alpha=1,2,3} \left[ \hat{c}_B^\dagger(\mathbf{r}_A + \boldsymbol{\delta}_\alpha) \hat{c}_A(\mathbf{r}_A) + h.c. \right]$$

In order to diagonalize this Hamiltonian and obtain the dispersion relation, one can write the operators in Fourier space:

$$\hat{c}_A(\mathbf{r}_i) = \frac{1}{\sqrt{N}} \sum_{\mathbf{k}} e^{-i\mathbf{k}.\mathbf{r}_i} \hat{c}_A(\mathbf{k})$$

By inserting this expression in the Hamiltonian (1.2), we can write:

$$\widehat{H} = -t \sum_{\mathbf{k}} \left[ \gamma(\mathbf{k}) \hat{c}_B^\dagger(\mathbf{k}) \hat{c}_A(\mathbf{k}) + h.c. \right]$$

with:

$$\gamma(\mathbf{k}) = \sum_{\alpha=1,2,3} e^{i\boldsymbol{\delta}_\alpha.\mathbf{k}} = 2\cos\left(\frac{\sqrt{3}ak_y}{2}\right) e^{-i\frac{a}{2}k_x} + e^{iak_x}$$

Finally, the Hamiltonian can be expressed as a product of matrix and vectors:

$$\widehat{H} = t \sum_{\mathbf{k}} \begin{pmatrix} \hat{c}_A^\dagger(\mathbf{k}) & \hat{c}_B^\dagger(\mathbf{k}) \end{pmatrix} \begin{pmatrix} 0 & \gamma^*(\mathbf{k}) \\ \gamma(\mathbf{k}) & 0 \end{pmatrix} \begin{pmatrix} \hat{c}_A(\mathbf{k}) \\ \hat{c}_B(\mathbf{k}) \end{pmatrix}$$

and the dispersion relation is obtained by diagonalizing the matrix in the above expression, which gives:

$$E_{\mathbf{k},\lambda} = \lambda t |\gamma(\mathbf{k})| = \lambda t \sqrt{1 + 4\cos\left(\frac{\sqrt{3}a}{2}k_y\right)\cos\left(\frac{3a}{2}k_x\right) + 4\cos^2\left(\frac{\sqrt{3}a}{2}ky\right)} \quad \text{with} \quad \lambda = \pm 1 \tag{1.3}$$

As the tight-binding model does not take into account the spin, each state will be spin degenerated. Furthermore, as each atom brings an electron, the Fermi level lies at $E_F = 0$ eV without doping. It leads to the fact that, at zero temperature, all the states with a negative energy ($\lambda = -1$) are filled and all the states with a positive energy ($\lambda = +1$) are empty. The valence band is related to all the states with a negative energy and the conduction band to all the states with a positive energy, even if there is no band gap in graphene. The energy bands are represented in Figure 1.3.
At the points:

$$\mathbf{K} = \left(0, \frac{4\pi}{3\sqrt{3}a}\right) \quad \text{and} \quad \mathbf{K'} = \left(0, -\frac{4\pi}{3\sqrt{3}a}\right) = -\mathbf{K}$$

and at the equivalent points in reciprocal space, $\gamma(\mathbf{k})$ and thus $E_{\mathbf{k},\boldsymbol{\lambda}}$ cancels out and the two bands are joining each other. In the vicinity of $\mathbf{K}$ and $\mathbf{K'}$, also called Dirac points, the dispersion is conical. Indeed, the development at order 1 in $\mathbf{k}$ gives:

$$\begin{aligned} \gamma(\pm\mathbf{K} + \mathbf{k}) &= 2\cos\left(\frac{2\pi}{3} \pm \frac{\sqrt{3}ak_y}{2}\right) e^{-i\frac{a}{2}k_x} + e^{iak_x} \\ &\sim 2\left(-\frac{1}{2} \mp \frac{3a}{4}k_x\right)\left(1 - i\frac{a}{2}k_x\right) + (1 + iak_x) \\ &\sim \frac{3a}{2}\left(\mp k_y + ikx\right) \end{aligned}$$

By defining the Fermi velocity as $v_F = 3at/2\hbar \sim 10^6\ m.s^{-1}$, the energy in the vicinity of the Dirac points $\mathbf{K}$ and $\mathbf{K'}$ follows the linear relation:

$$E_{\pm\mathbf{K}+\mathbf{k},\lambda} = \lambda \hbar v_F k \tag{1.4}$$

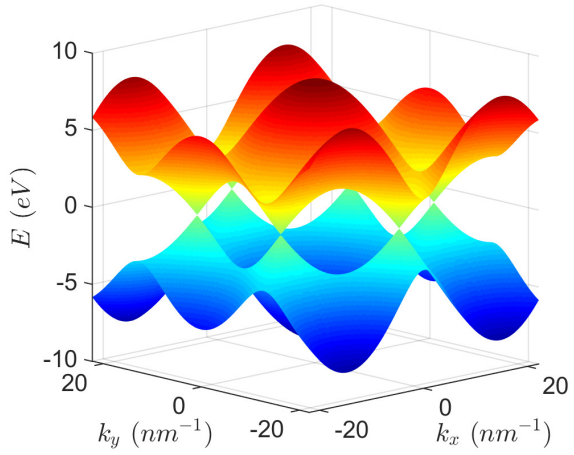


Figure 1.3: *Graphene band diagram (first Brillouin zone) within the nearest neighbor tight-binding model. The valence band is shown in blue and the conduction band in red.*

### 1.2.2 Graphene quantum dot

We define a graphene quantum dot (GQD) of radius $R$ as the graphene structure contained in a circle of radius $R$, with an origin set in the middle of the bond between the A and B atoms of the unit cell of an ideal infinite graphene lattice, as represented in Figure 1.4.

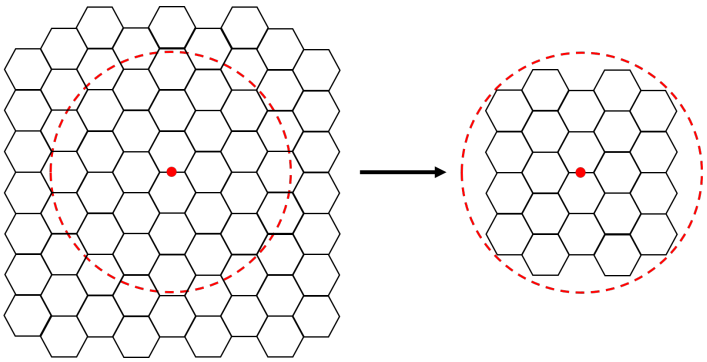

Figure 1.4: *Geometrical definition of a graphene quantum dot, by cutting a circular structure from an infinite graphene sheet.*

In the way we define a GQD, we do not impose any condition on the edge shape and cut dangling bonds by supposing that simply connected carbon atoms in the border most probably do not survive the lithography step. As our fabrication process of GQDs does not allow the exact control of their edge shape, this definition is very important to better describe the fabricated GQDs.

#### Tight-binding approach applied to a GQD

A GQD is no longer an infinite two-dimensional graphene. Nevertheless, a discrete tight-binding model is relevant, showing similar results to a continuous model for small GQDs [32] and large ones, as the spectrum is expected to tend toward that of graphene. Because of its finite size which break the translational symmetry of the crystal, the Bloch theorem is not valid anymore. Nevertheless, we can still start from the Hamiltonian (1.1) and find the

stationary states $|\Psi_i(\mathbf{r})\rangle$ of energy $E_i$ on the form:

$$|\Psi_i(\mathbf{r})\rangle = \frac{1}{N}\left\{\sum_{\mathbf{R_A}} c_i(\mathbf{R_A})|\phi(\mathbf{r}-\mathbf{R_A})\rangle + \sum_{\mathbf{R_B}} c_i(\mathbf{R_B})|\phi(\mathbf{r}-\mathbf{R_B})\rangle\right\} \tag{1.5}$$

solutions of the equations

$$\widehat{H}|\Psi_i(\mathbf{r})\rangle = E_i|\Psi_i(\mathbf{r})\rangle \tag{1.6}$$

where $N$ denotes here the number of carbon atoms of the GQD. From the diagonalization of the tight-binding matrix, we extract the spectrum and the associated wavefunctions for different GQD radii, ranging from 3 nm to 25 nm.

In the case of ideal graphene, the Hilbert space dimension can be reduced to 2. For a GQD, the wavefunctions must be expressed in the finite $|\phi(\mathbf{r}-\mathbf{R_{A/B}})\rangle$ basis, thereby setting the Hilbert space dimension to $N$. Consequently, the tight-binding matrix to diagonalize is of dimension $N$, which grows exponentially with the size of the GQD (see Table 1.1). This fact has an huge consequence on the numerical work, which involves diagonalization of extremely large matrices. The strategy proposed by N. Regnault (LPENS) consists in focusing on a limited spectral region of interest.

| *Radius (nm)* | 3 | 7 | 11 | 15 | 19 | 25 |
|---|---|---|---|---|---|---|
| $N$ | 1052 | 5850 | 14446 | 26936 | 43186 | 74866 |

Table 1.1: *Number of carbon atoms and thus order of the tight-binding matrix for distinct GQD radii.*

### 1.2.3 Density of states

It is convenient to compute the density of states (DOS) to get a first insight on the theoretical predictions. In the nearest neighbor tight-binding frame, using 1.3, it is possible to get an analytical expression [37] for the DOS of an infinite graphene sheet $\rho_{graphene}(E) = \int_{\mathbb{R}} \frac{dk_x dk_y}{(2\pi)^2}\delta(E - E_{\mathbf{k}})$, plotted in Figure 1.5. We see that the density of states is linear in $E$ around the Dirac point and reach its maximum when $E = \pm t$ (red dashed line). As discussed in detail in the following section, the first effect of setting a finite size for graphene is the appearance of numerous zero-energy or very low energy states close to the Dirac point. To highlight this outcome it is thus more convenient to use a different definition to compute the DOS for GQDs.

For a GQD composed of $N$ atoms, we set an energy step $\Delta$ and compute for each energy level $E_n$ the following DOS $\rho_{GQD}$[1]:

$$\rho_{GQD}(E_n) = \begin{cases} \dfrac{2}{N}\dfrac{2}{E_{n+1}-E_{n-1}} \text{ if } E_{n+1}-E_n > \Delta \text{ or } E_n - E_{n-1} > \Delta \\ \\ \dfrac{2}{N}\dfrac{number\ of\ states\ in\ E_n \pm \dfrac{\Delta}{2}}{\Delta} \text{ otherwise} \end{cases} \tag{1.7}$$

This definition tends to the usual DOS definition when $\Delta$ tends to zero and emphasizes the DOS variations when a high number of states lies in a small energy range. Figure 1.6[2]

[1] The factor 2 accounts for the spin.

[2] Whereas the spectrum is symetrical in energy, the small asymmetry observed in the DOS is an artefact of computation of (1.7) that depends on how the energy levels are browsed (increasing or decreasing order) and arises when they are very dense in a small energy range.

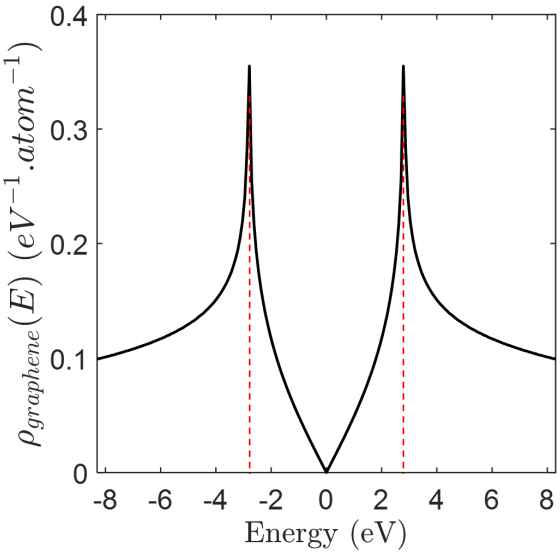


Figure 1.5: *Density of states of an infinite graphene sheet within the nearest neighbor tight-binding model. Red dashes lines denotes* $E = \pm t = \pm 2.8\ eV$

shows the computed DOS using (1.7) for $R = 8\ nm$ (blue curves), for different values of $\Delta$, compared with the usual DOS of an infinite graphene sheet (black curve).

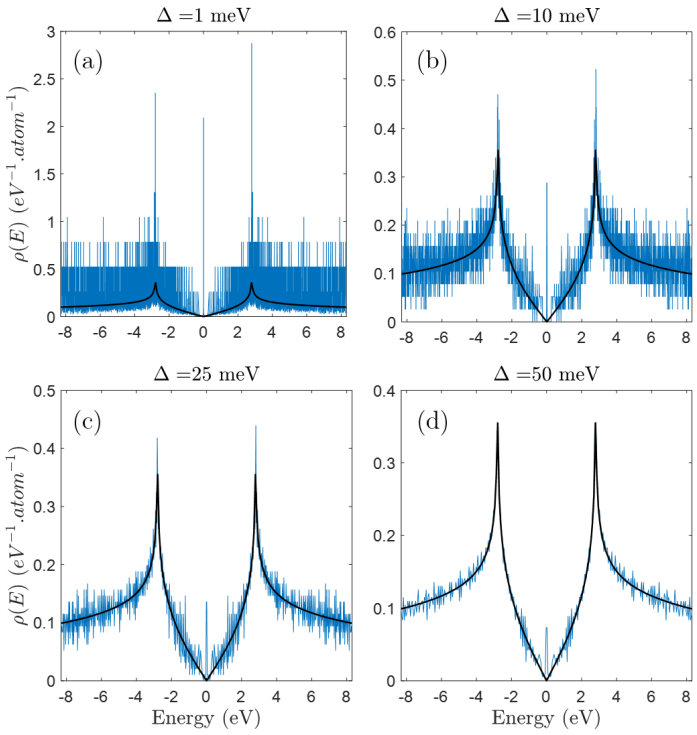


Figure 1.6: *Graphene DOS (black curve) compared to the DOS of a GQD of radius* 8 *nm (blue line) for different values of* $\Delta$.

The full discretization of the electronic states is clearly observed. Moreover, we see that a high DOS around the Dirac point is observed for a GQD whereas $\rho_{graphene}$ tends to zero as the energy tends to zero. Smaller values of $\Delta$ better reveal local variations of the DOS induced by the electronic confinement and show the presence of a large number of states

lying near the Dirac point. As shown in Figure 1.7, the high DOS around $E = 0\ eV$ is observed whatever the size of the GQDs, from $R = 3\ nm$ to $R = 25\ nm$.

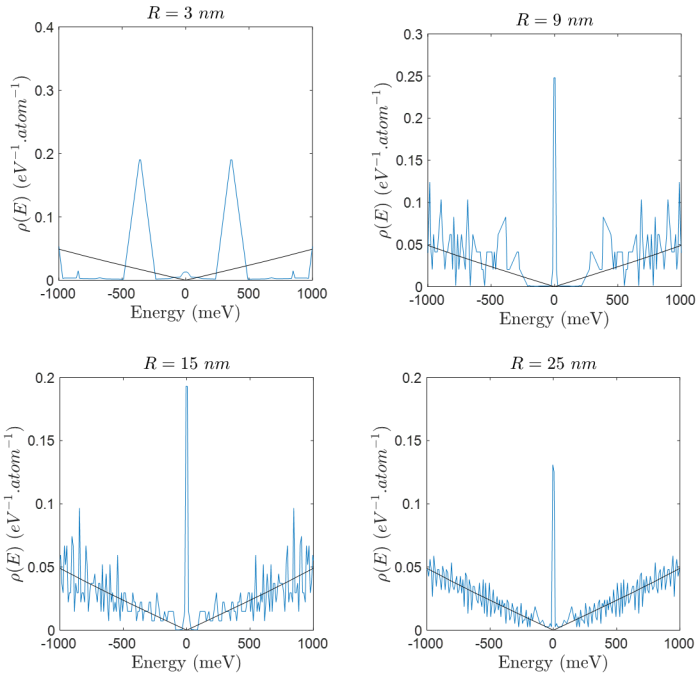


Figure 1.7: *Graphene DOS (black curve) compared to the DOS of a GQD of different radius (blue lines), with* $\Delta = 10\ meV$.

However, how $\rho_{GQD}(E \sim 0)$ evolves when the GQD size is increased remains unclear. As this peak in the DOS appears when the graphene has a finite size and thus boundaries, it should emerge from the existence edges of the GQDs. Furthermore, we see that the deviation from $\rho_{graphene}$ occurs in a definite range of energy, which depends on the GQD size. From these observations, it appears that a deeper study of the many discrete electronic states of these large GQDs is needed.

## 1.3 Analysis of the energy levels

In this section, we analyze the different types of energy states that are observed in the total energy spectrum of the GQDs. A main originality of our study is that we do not impose the edge configuration of the GQDs, meaning they possess different kinds of termination, which randomly fluctuate with their size. Consequently, such systems are hardly described analytically.

### 1.3.1 Wavefunction spatial integrals

For all GQDs with a radius ranging from $R = 3\ nm$ to $R = 25\ nm$, we have determined the eigen energies $E_{i,R}$ and the associated eigen wavefunctions $\Psi_{i,R}(r)$ from the tight-binding hamiltonian (1.1). In this section, we present an analysis of the wavefunctions and examine their spatial extension to better classify the many eigen states.

Instead of manually viewing all the probability densities $|\Psi_{i,R}(r)|^2$, we use a numerical parameter to evaluate the spatial extension of a wavefunction. As depicted on Figure 1.8, we

define the following overlap integral:

$$I_x = 2\pi \int_0^{xR} |\Psi_{i,R}(r)|^2 r dr \tag{1.8}$$

with $0 < xR \leq 1$ the fraction of the radius on which we integrate the probability density. Consequently, $0 < I_x \leq 1$.

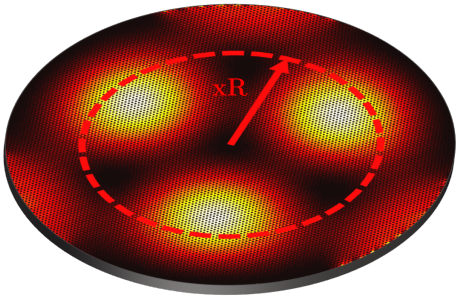


Figure 1.8: *Definition of the overlap integral* (1.8)*: the probability density* $\Psi_R(r)$ *is integrated over a disk of radius* $xR$*.*

Figure 1.9 shows the energy spectrum of each GQD as function of their radius. The color code indicates the value of $I_{0.85}$ for each eigen energy. We restrict the plot to the positive energies as the spectrum is symmetrical due to electron-hole symmetry. The $I_{0.85}$ values for negative energies are also following the same variations.

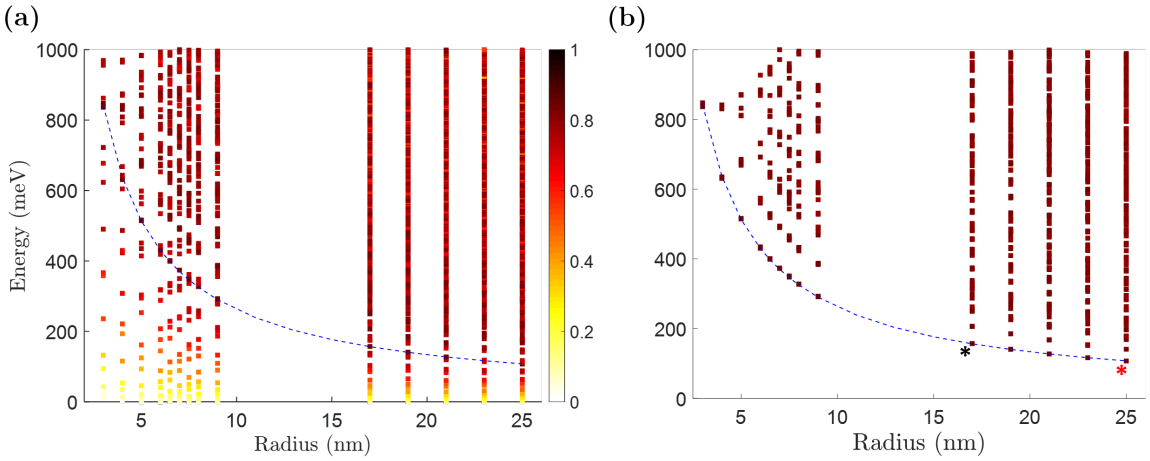


Figure 1.9: *(a) Energy (left scale) and probability amplitude over 85% of the radius (color scale) of GQDs states for a few radii values. The dashed line is a guide for the eyes: states below the line have small* $I_{0.85}$ *values, and some states above have large* $I_{0.85}$ *values. (b) States such as* $I_{0.85} > 0.8$ *are plotted while keeping the energy and color scale. The dashed line actually follows the lowest energy bulk states. The probability density of the states denoted by black and red stars are shown in Figure 1.10*

As expected, a multitude of energy levels are observed which become denser and denser as the radius of the GQD increases. To get a clearer picture, we report in Figure 1.9 (b) only the states such as $I_{0.85} > 0.8$. These energy levels correspond to the energy modes of the GQDs mainly localised on the bulk and that originate from the finite size of the GQD.

We refer the energy states as bulk states. The dashed line is a guide for eye of the lowest energy levels that verify $I_{0.85} > 0.8$, i.e. of bulk states. This lowest energy bulk states for R=17 nm and 25 nm, denoted by black and red stars respectively, are shown in Figure 1.10.

Below the dashed line, in the lower energy range, we observe that for all GQD sizes,

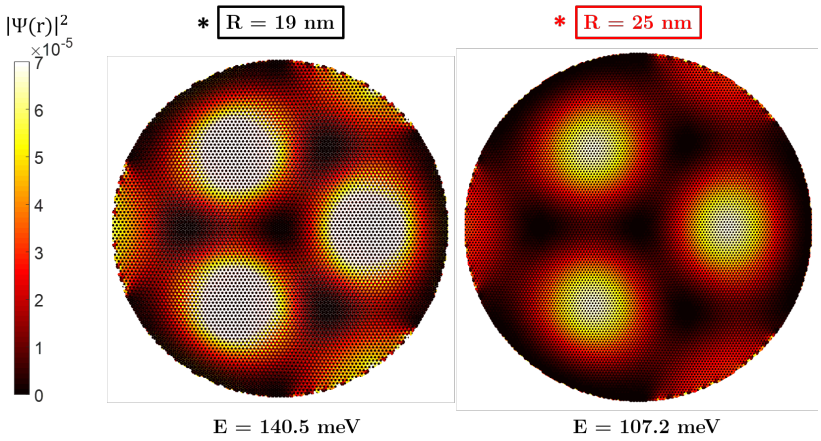


Figure 1.10: *Probability density* $|\Psi(r)|^2$ *(left color bar) for the lowest energy bulk state of a GQD of radius* $R = 19$ *and 25 nm, pointed out respectively by dark and red stars in Figure 1.9 (b). Their respective energies are reported below each probability density.*

$I_{0.85}$ smoothly and continuously decreases from 0.8 to $\sim 0$ at very low energies. We select few states at very low energy, close to the Dirac point, and note that their probability density is distributed only on the edges. In agreement with previous reports, a large density of states close to zero energy is introduced by the edges. Two edge configurations are of particular interest in finite size graphene: zigzag and armchair (see Figure 1.11). It has been

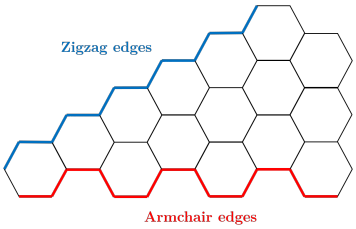


Figure 1.11: *Sketch of two possible graphene edge configurations: armchair and zigzag.*

well established, in GQD, that zigzag edges lead to a zero-energy density of states that are spatially localized near the zigzag edges, resulting in a sharp peak at $E = 0\ eV$ in the density of states. However, contradictory results have been reported [38, 39] on the localisation and energy of the wavefunctions that lie in the vicinity of armchair edges. In Figure 1.12, we observe that the probability density is high only for some parts of the edges corresponding mainly to zigzag edges. These low energy states are referred as edge states.

If now we focus on states with $0.5 \leq I_{0.85} \leq 0.7$, we observe that are distributed at intermediate energies starting above edge states up to high energy (see Figure 1.13). Their probability density, reported in Figure 1.14, indicates a non-negligible spatial extension ($I_{0.85} \sim 0.66 - 0.7$) both on the edges and over the GQD surface. We define these states as "mixed states", as they seem to be in an edge-bulk intermediate regime. These states are by far the most numerous and thus dominate the spectrum of the GQD in the few tens of nanometer radius range.

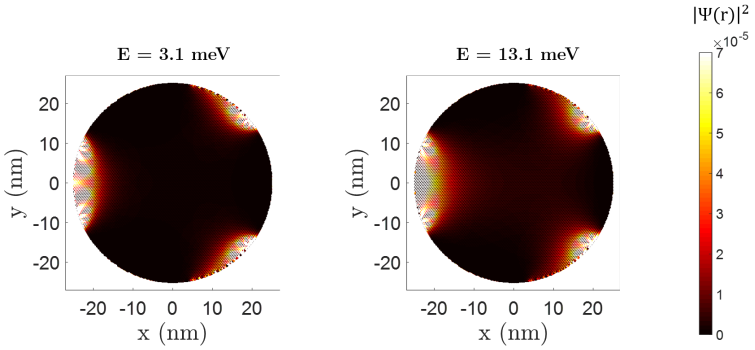


Figure 1.12: *Probability density (right color bar) for selected low energy states of a GQD of radius 25 nm.* $|\Psi(r)|^2$ *is high only for some peculiar parts of the edges. We identify these wavefunctions to be edge states.*

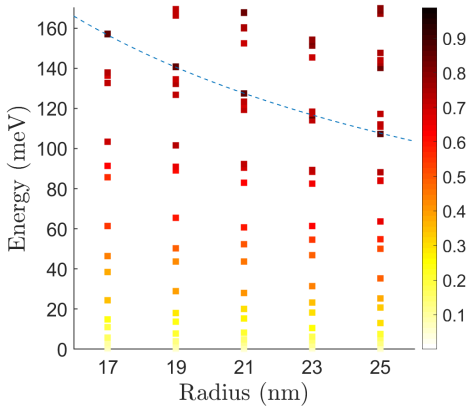


Figure 1.13: *Energy (left scale) and probability amplitude over 85% of the radius (color scale) of GQDs states for large radii values. The dashed line is a guide for the eyes: numerous states below the line have a non-negligible spatial extension (*$0.5 \leq I_{0.85} \leq 0.7$ *: red squares) over the GQD surface.*

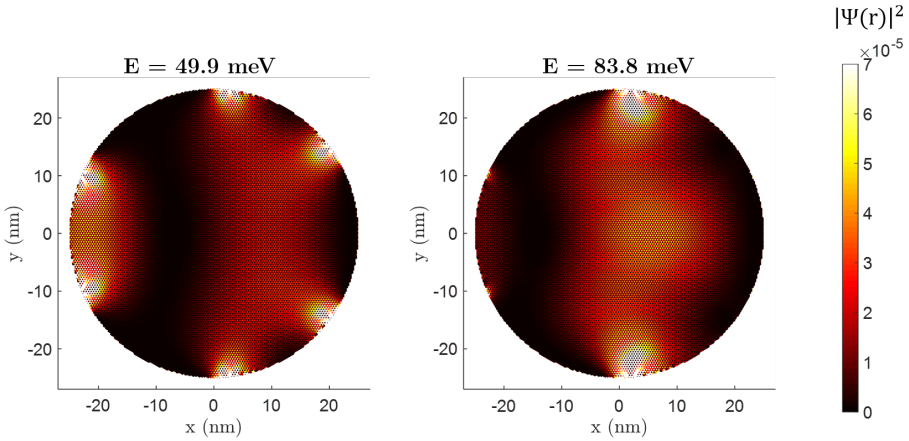


Figure 1.14: *Probability density (right color bar) for selected states of a GQD of radius 25 nm with a non-negligible spatial extension over the GQD surface. We define these wavefunctions to be "mixed states".*

### 1.3.2 Mixed states

We represent on Figure 1.15 and 1.16 the probability density $|\Psi_{i,R}(r)|^2$ of few energy wavefunctions, for $R = 19$ $nm$ and $R = 25$ $nm$ respectively. In each Figure, we compare the mixed states $|\Psi(r)|^2$ profile (right) with the probability density of two typical cases (left): an edge state of energy $\sim 0$ eV (bottom), where the electrons lie on the edges and the lowest energy bulk state (top), with a well defined bulk mode.

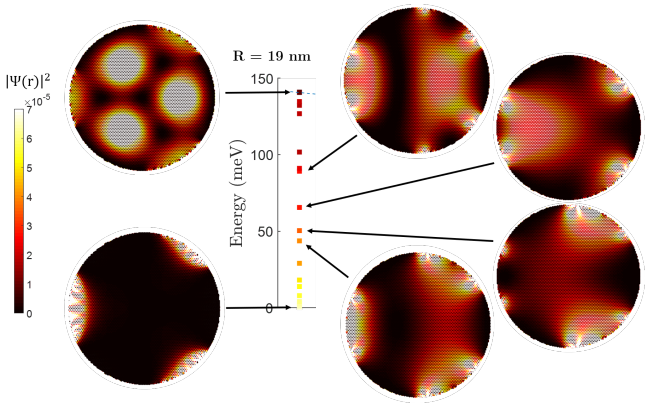


Figure 1.15: *Probability density* $|\Psi(r)|^2$ *(left color bar) for selected low energy states on the central vertical panel (which gives again the spectral dependence of* $I_{0.85}$ *in color scale of Figure 1.13), for a GQD of radius 19 nm.*

For both GQD sizes, we observe that the mixed state probability density exhibits a different signature compared to the limit examples (edge state and bulk state): $|\Psi(r)|^2$ is high for some peculiar parts of the edges but also extends from these edge parts into the bulk part of the quantum dot. A closer look at the edges reveals that the peculiar parts of the edges where the probability density is high are armchair borders.

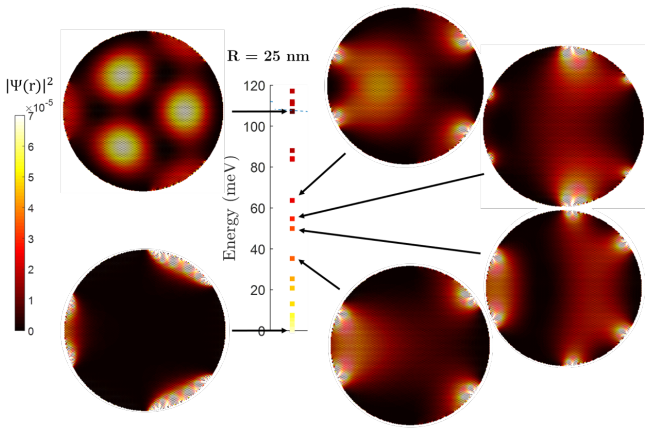


Figure 1.16: *Probability density* $|\Psi(r)|^2$ *(left color bar) for selected low energy states on the central vertical panel (which gives again the spectral dependence of* $I_{0.85}$ *in color scale of Figure 1.13), for a GQD of radius 25 nm.*

We interpret this observation as a direct consequence of the graphene finite size structure. Indeed, a recent work has reported theoretical results on the existence of localised states near

the armchair edges of an infinite graphene sheet [38]. Unlike zigzag edge states, which have zero energy and are strongly localised on the zigzag edges, the armchair edge state wavefunctions show non-monotonous (oscillating) decay by moving away from the edge. Interestingly, applied to our finite-size system, it might suggest that if their typical localization length is on the order of the GQD radius, armchair edge states from different borders of the dot can cover the entire bulk surface.

Furthermore, these mixed states lie in the energy range above the zero-energy edge (zigzag) states. Depending on their typical localization length, these states are expected to show a pronounced energy dispersion. Using the analytical expressions of [38], we compute on Figure 1.17 the normalised density of states of armchair edge states in the case of ideal graphene with armchair edges, for various values of their typical spatial extension from the armchair edges to the bulk $\xi$. We see that the armchair edge states, which extend far from the edge

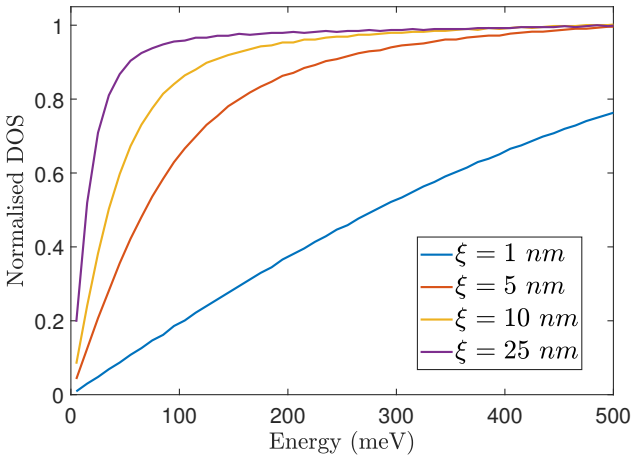


Figure 1.17: *Computed normalised density of states for localised electron states near the archmair edges of graphene, as function of their typical spatial extension from the armchair edges to the bulk $\xi$, for positive energies. Their dispersion in energy strongly depend on their localization lengyh $\xi$.*

exhibit the higher density. In addition, when $\xi \geq 10\ nm$, the density quickly tends to a constant for the wavefunctions of energies $E \geq 150\ nm$. This suggests that armchair edge states with a localization length on the order of the GQD radius might be predominant in the high energy spectrum, meaning above the first bulk state. This result is confirmed by selecting few states in this quasi-continuum (see Figure 1.18): we observe $|\Psi(r)|^2$ features similar to those of Figure 1.15 and 1.16.

Note that the wavefunctions that are strongly localised in the bulk, refereed as bulk states, are totally distinct in their nature from the mixed states even when the spectrum is sparse. However, it becomes difficult to distinguish them in the higher energy continuum only with a criteria on the overlap integral parameter $I_x$.

### 1.3.3 Bulk states

#### Continuous low-energy model

In this section, we explore a different method for the identification of the bulk states of the GQD based on a continuous model [40]. At low energy, the Hamiltonian of the system has

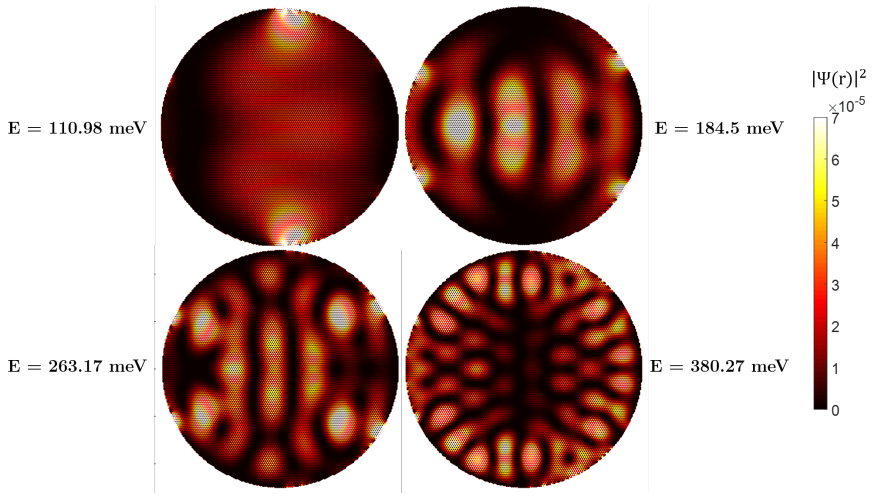


Figure 1.18: *Probability density (right color bar) for few states lying in the quasi-continuum of energy levels above the dashed line in Figure 1.9, for GQD of radius 25 nmn with their respective energy.* $|\Psi(r)|^2$ *is high for some armchair borders and extends from these parts into the bulk part of the dot.*

the structure of a Dirac Hamiltonian:

$$H = \hbar v_F \begin{pmatrix} 0 & -i\left(\frac{\partial}{\partial x} - i\frac{\partial}{\partial y}\right) \\ -i\left(\frac{\partial}{\partial x} + i\frac{\partial}{\partial y}\right) & 0 \end{pmatrix} \tag{1.9}$$

We then write $H\Psi(\mathbf{r}) = E\Psi(\mathbf{r})$, with $\Psi(\mathbf{r})$ as a two-component wavefunction:

$$\Psi(\mathbf{r}) = \begin{pmatrix} A(\mathbf{r}) \\ B(\mathbf{r}) \end{pmatrix} \tag{1.10}$$

Taking into account the cylindrical symmetry of the problem, we can write the first component of $\Psi(\mathbf{r})$ as $A(\mathbf{r}) = A(r, \varphi)$, which leads to the following differential equation:

$$\left(\frac{\partial^2}{\partial r^2} + \frac{1}{r}\frac{\partial}{\partial r} + \frac{1}{r^2}\frac{\partial^2}{\partial \varphi^2}\right) A(r,\varphi) = -\left(\frac{E}{\hbar v_F}\right)^2 A(r,\varphi) \tag{1.11}$$

Even if the GQDs are not perfect circles, we consider a circle symmetry and thus assume the following angular dependance of the wavefunction component:

$$A(r,\varphi) = e^{im\varphi} a(r) \tag{1.12}$$

where the integer $m$ stands for the eigenstate angular momentum. It converts Equation (1.11) into:

$$\left(\frac{\partial^2}{\partial r^2} + \frac{1}{r}\frac{\partial}{\partial r} - \frac{m^2}{r^2}\right) a(r) = -\left(\frac{E}{\hbar v_F}\right)^2 a(r) \tag{1.13}$$

One simple solution of Eq.(1.13) is the Bessel function of first kind[3] $J_m\left(\frac{Er}{\hbar v_F}\right)$. Thus, the boundary condition, which is $\Psi(r = R) = 0$, leads to:

$$J_m\left(\frac{ER}{\hbar v_F}\right) = 0 \tag{1.14}$$

and we obtain a quantification of the eigenvalues solutions of our problem:

$$E_m(R) = \frac{\hbar v_F \Theta_J^1(m)}{R} \tag{1.15}$$

where $\Theta_J^1(m)$ stands for the first zero of the Bessel function $J_m$.

[3]The Bessel function of second kind $Y_m(Er/\hbar v_F)$ is not included, as it is singular at $r = 0$

**Normal modes of graphene quantum dots**

On Figure 1.19, we plot the $E_m(R)$ curves for different values of $m$ on the calculated energy spectra of the GQDs, by holding only the states such as $I_{0.85} \geq 0.8$ for clarity. We see that

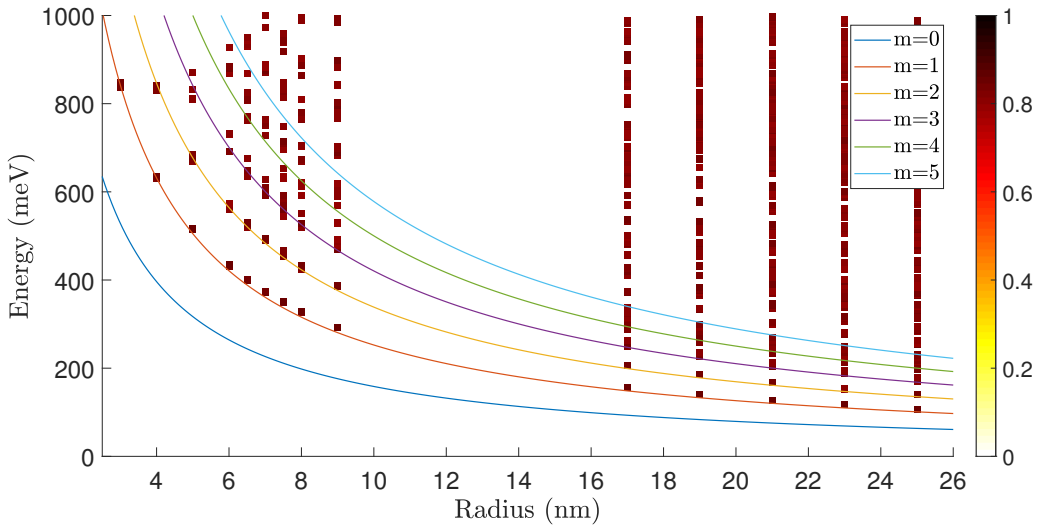


Figure 1.19: *Eigenvalues $E_m$ as function of $R$ for different values of the angular momentum $m$, plotted on Figure 1.9 (b) (Energy and probability amplitude over 85% of the radius (color scale) of GQDs states such as $I_{0.85} > 0.79$, for a few radii values).*

this model well describes the states spatially concentrated in the bulk for $1 \leq m \leq 3$, namely those with $I_{0.85} \geq 0.8$, labelled as bulk states. Furthermore, it confirms the relevance of the overlap integral criteria to distinguish the different energy states: the lowest energy bulk state $E_{m=1}(25\ nm) = 107.2\ meV$ shown in Figure 1.10 is clearly different from the nearest energy level $E = 110.98\ meV$ above shown in Figure 1.18, for which $I_{0.85} \leq 0.7$ and thus refereed as a mixed state.

The normal mode of angular momentum $m = 0$ is probably not supported by the GQD geometry as the graphene-based material we modelled is not a circle but made by cutting a circular shape on a lattice of incommensurate geometry. In contrast, the states with an angular momentum $m \geq 1$ have at least one node in the bulk and therefore capture a certain reality of the system. We finally note that the higher energy bulk states cannot be described by this model as the normal modes for high values of the angular momentum $m$ are found to have eigen energies $E_m$ far from the Dirac point, which does not correspond to valid solutions of the low-energy effective model 1.9 we used.

Our analysis of the electronic state distribution of large GQDs shows the existence of three different types of states. The first type refers to edge states that are strongly localised on the edge of the GQDs. The second type corresponds to wavefunctions mostly localised on the bulk and that are thus defined as bulk states. The third type corresponds to mixed-states as they extend from the edges to the centered of the GQD. Based on this knowledge, we now investigate how THz photons can be coupled to these various energy states.

## 1.4 Light-matter interaction

In this section, we investigate the absorption probability $\alpha(\hbar\omega)$ of monolayer GQDs of radii $17\ nm \leq R \leq 25\ nm$ excited by low energy photons $\hbar\omega \leq 1\ eV$. We explore how their

absorption spectra depends on the size, the temperature and the doping levels of the GQDs.

### 1.4.1 Absorption probability of a GQD

In order to get the absorption probability $\alpha$ of a GQD, we treat as a perturbation the dipole interaction potential $V_{dip} = \frac{e}{m_e}\hat{\mathbf{p}}.\mathbf{A}$ with the electromagnic field $\mathbf{E}(t) = -\frac{\partial \mathbf{A}}{\partial t}$, where $\mathbf{A}(t)$ is the potential vector associated to an electromagnetic plane wave $\mathbf{E}(t)$, at normal incidence on the GQD, using the Coulomb gauge:

$$\mathbf{A}(t) = \boldsymbol{\epsilon}(A_0 e^{-i\omega.t} + h.c)$$

with $A_0$ a constant and $\boldsymbol{\epsilon}$ a unitary polarization vector, assuming a linearly polarised wave. We have neglected the spatial dependence of the potential vector, given the fact that in the case of an illumination by photons of energy $\hbar\omega < 1\ eV$, the wavelength of the incident radiation is much higher than any dimension of the GQD.

Hence, the transition probability per unit of time $\Gamma_{if}$ from a state $|\Psi_i(\mathbf{r})\rangle$ to a state $|\Psi_f(\mathbf{r})\rangle$ (using the Kubo linear response formula [12]) is written:

$$\Gamma_{if}(\omega) = \frac{2\pi}{\hbar}\left(\frac{e}{m_e}\right)^2 |A_0|^2 |\langle\Psi_i(\mathbf{r})|\hat{\mathbf{p}}.\boldsymbol{\epsilon}|\Psi_f(\mathbf{r})\rangle|^2 \Delta\delta_{i,f}(\omega)[f(E_i) - f(E_f)] \times 2 \tag{1.16}$$

with $m_e$ the electron mass, $f$ the Fermi-Dirac distribution and $\Delta\delta_{i,f}(\omega) = \delta\left(E_f - E_i - \hbar\omega\right) - \delta\left(E_f - E_i + \hbar\omega\right)$. The factor 2 comes from the fact that spin interactions are neglected.

We thus need to calculate the matrix elements of $\hat{\mathbf{p}}$. Using expression 1.5 for $|\Psi_{i/f}(\mathbf{r})\rangle$, the matrix elements are expressed as[4]:

$$\begin{aligned}
\langle\Psi_i(\mathbf{r})|\hat{\mathbf{p}}|\Psi_f(\mathbf{r})\rangle = &\sum_{\mathbf{R_A}} c_i^*(\mathbf{R_A}) c_f(\mathbf{R_A}) \langle\phi(\mathbf{r}-\mathbf{R_A})|\hat{\mathbf{p}}|\phi(\mathbf{r}-\mathbf{R_A})\rangle \\
&+ \sum_{\mathbf{R_A}}\sum_{\mathbf{R_B}} c_i^*(\mathbf{R_B}) c_f(\mathbf{R_A}) \langle\phi(\mathbf{r}-\mathbf{R_B})|\hat{\mathbf{p}}|\phi(\mathbf{r}-\mathbf{R_A})\rangle \\
&+ \sum_{\mathbf{R_B}} c_i^*(\mathbf{R_B}) c_f(\mathbf{R_B}) \langle\phi(\mathbf{r}-\mathbf{R_B})|\hat{\mathbf{p}}|\phi(\mathbf{r}-\mathbf{R_B})\rangle \\
&+ \sum_{\mathbf{R_B}}\sum_{\mathbf{R_A}} c_i^*(\mathbf{R_A}) c_f(\mathbf{R_B}) \langle\phi(\mathbf{r}-\mathbf{R_A})|\hat{\mathbf{p}}|\phi(\mathbf{r}-\mathbf{R_B})\rangle
\end{aligned} \tag{1.17}$$

The first and third terms are zero because in the nearest neighbour tight-binding model, only the matrix elements of $\hat{\mathbf{p}}$ between two neighboring atoms are non zero. In addition, considering the relation [41]:

$$\begin{aligned}
\langle\phi(\mathbf{r}-\mathbf{R_B})|\hat{\mathbf{p}}|\phi(\mathbf{r}-\mathbf{R_A})\rangle &= -\langle\phi(\mathbf{r}-\mathbf{R_A})|\hat{\mathbf{p}}|\phi(\mathbf{r}-\mathbf{R_B})\rangle \\
&= -\langle\phi(\mathbf{r})|\hat{\mathbf{p}}|\phi(\mathbf{r}-(\mathbf{R_B}-\mathbf{R_A}))\rangle \\
&= -\langle\phi(\mathbf{r})|\hat{\mathbf{p}}|\phi(\mathbf{r}-\boldsymbol{\delta_\alpha})\rangle \\
&= +\frac{im_e t}{\hbar}\boldsymbol{\delta_\alpha}
\end{aligned}$$

Equation (1.17) becomes:

$$\langle\Psi_i(\mathbf{r})|\hat{\mathbf{p}}|\Psi_f(\mathbf{r})\rangle = \frac{im_e t}{\hbar}\sum_{\alpha=1,2,3}\boldsymbol{\delta_\alpha}\left\{-\sum_{\mathbf{R_A}} c_i^*(\mathbf{R_A}) c_f(\mathbf{R_A}+\boldsymbol{\delta_\alpha}) + \sum_{\mathbf{R_B}} c_i^*(\mathbf{R_B}) c_f(\mathbf{R_B}-\boldsymbol{\delta_\alpha})\right\} \tag{1.18}$$

[4]For clarity, we include the normalisation factor in the coefficients $c_{i,f}(\mathbf{R})$

We then express the $\mathbf{X}$ and $\mathbf{Y}$ components of $\hat{\mathbf{p}}$ as:

$$\langle\Psi_i(\mathbf{r})|\hat{\mathbf{p}}|\Psi_f(\mathbf{r})\rangle = \frac{im_e t a_0}{\hbar}\left(C_x^{i,f}\mathbf{X} + C_y^{i,f}\mathbf{Y}\right) \tag{1.19}$$

by defining the dimensioneless quantities $C_x^{i,f}$ and $C_y^{i,f}$ as:

$$C_x^{i,f} = \sum_{\alpha=1,2,3}\frac{\boldsymbol{\delta_\alpha}.\mathbf{X}}{a_0}\left\{-\sum_{\mathbf{R_A}} c_i^*(\mathbf{R_A})c_f(\mathbf{R_A}+\boldsymbol{\delta_\alpha}) + \sum_{\mathbf{R_B}} c_i^*(\mathbf{R_B})c_f(\mathbf{R_B}-\boldsymbol{\delta_\alpha})\right\} \tag{1.20}$$

and:

$$C_y^{i,f} = \sum_{\alpha=1,2,3}\frac{\boldsymbol{\delta_\alpha}.\mathbf{Y}}{a_0}\left\{-\sum_{\mathbf{R_A}} c_i^*(\mathbf{R_A})c_f(\mathbf{R_A}+\boldsymbol{\delta_\alpha}) + \sum_{\mathbf{R_B}} c_i^*(\mathbf{R_B})c_f(\mathbf{R_B}-\boldsymbol{\delta_\alpha})\right\} \tag{1.21}$$

For non-polarized laser excitation, one can average over different in-plane orientations to get:

$$\begin{aligned}|\langle\Psi_i(\mathbf{r})|\hat{\mathbf{p}}.\boldsymbol{\epsilon}|\Psi_f(\mathbf{r})\rangle|^2 &= \left(\frac{m_e t a_0}{\hbar}\right)^2\left(C_x^2\cos^2\theta + C_y^2\sin^2\theta + 2C_xC_y\cos\theta\sin\theta\right)_{i,f}\\ &\simeq \frac{1}{2}\left(\frac{m_e t a_0}{\hbar}\right)^2\left(C_x^2 + C_y^2\right)_{i,f}\end{aligned}$$

Finally, the absorbed power $W_{abs}(\omega)$ is given by:

$$W_{abs}(\omega) = \hbar\omega\sum_{i,f}\Gamma_{if} \tag{1.22}$$

The incident power $W_{inc}(\omega)$ on a dot of area $S = \pi R^2$ is:

$$W_{inc}(\omega) = 2\epsilon_0\omega^2 S|A_0|^2 c = 2\epsilon_0\omega^2\pi R^2|A_0|^2 c \tag{1.23}$$

Thus, the absorption probability coefficient $\alpha(\omega) = \frac{W_{abs}(\omega)}{W_{inc}(\omega)}$ is expressed as:

$$\alpha(\omega) = \frac{e^2t^2a_0^2}{\hbar\epsilon_0 cR^2}\sum_{i,f}\frac{1}{\hbar\omega}\left(C_x^2 + C_y^2\right)_{i,f}\Delta\delta_{i,f}(\omega)[f(E_i) - f(E_f)] \tag{1.24}$$

### 1.4.2 Influence of the GQD size on the absorption spectrum

We first start by studying the dependence of the size of the GQD on the absorption spectrum for large GQDs ($17\ nm \leq R \leq 25\ nm$) without taking into account the occupancy of the energy levels. For a given couple of initial and final states $|\Psi_i(\mathbf{r})\rangle$ and $|\Psi_f(\mathbf{r})\rangle$ with respective energies $E_i$ and $E_f$, we thus define the following dimensionless quantity:

$$\begin{aligned}f_{i,f} &= \frac{a_0^2}{R^2}\int_{-\infty}^{+\infty}\frac{t}{\hbar\omega}\left(C_x^2 + C_y^2\right)_{i,f}\delta\left(E_f - E_i - \hbar\omega\right)d(\hbar\omega)\\ &= \frac{a_0^2}{R^2}\frac{t}{E_f - E_i}\left(C_x^2 + C_y^2\right)_{i,f}\end{aligned} \tag{1.25}$$

which represents the absorption efficiency of the transition $|\Psi_i(\mathbf{r})\rangle \rightarrow |\Psi_f(\mathbf{r})\rangle$ for a photon of energy $\hbar\omega = E_f - E_i$. Figure 1.20 represents the $f_{i,f}$ values as function of $E_f - E_i$ for $R = 17\ nm$ and $R = 25\ nm$. One clearly see that for both GQD sizes, photons mainly couple with energy levels separated by few tens of meV. The maximum probability and the energy range of efficient transitions clearly depend on the radius of the GQD.

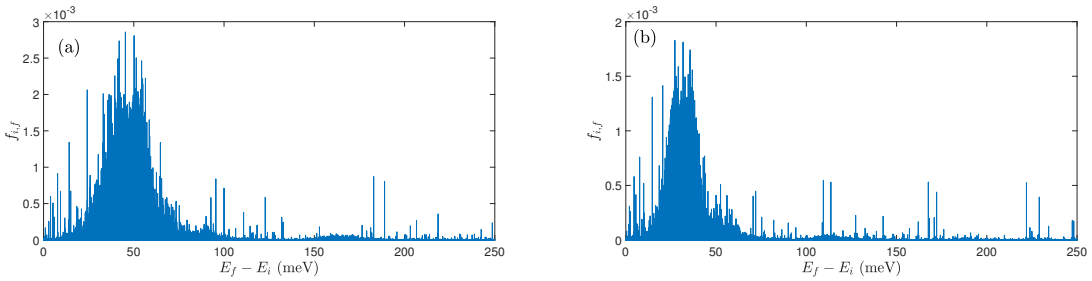


Figure 1.20: *Dimensionless parameter $f_{i,f}$ related to the absorption probability (see Eq.* (1.25)*) for $R = 17$ nm (left) and 25 nm (right), computed for each state of the GQD considered as a possible initial state, towards all of its higher energy states, considered as possible final states, plotted as function of their energy seperation.*

In order to better visualize how the absorption efficiency evolves when the GQD radius is increased, we smooth the $f_{i,f}$ curve by a Lorentzian filter of half-width-at-half maximum $\Gamma$:

$$\mathcal{F}_\Gamma(\hbar\omega) = \frac{e^2 t}{\hbar\epsilon_0} \sum_{i<f} f_{i,f} \frac{\Gamma/\pi}{\Gamma^2 + (E_f - E_i - \hbar\omega)^2} \tag{1.26}$$

Note that this quantity differs from the absorption probability defined in Equation (1.24) by the absence of population effects and the consideration of a single broadened $\delta$ distribution instead of the two non-broadened $\delta$ (and by the lack of a $1/c$ multiplicative factor). Thus, the quantity (1.26) does not describe the real absorption probability of the GQD, but more likely all the possible transitions $E_i \to E_f$, weighted by their efficiency $f_{i,f}$. The influence of temperature and the Fermi distribution will be discussed in section 1.4.4.
Given the observed energy range of efficient transitions, we set $\Gamma = 1\ meV$ to preserve the curve shape. Figure 1.21 shows the normalised values of $\mathcal{F}_{\Gamma=1}(\hbar\omega)$ for different GQD sizes $R$.

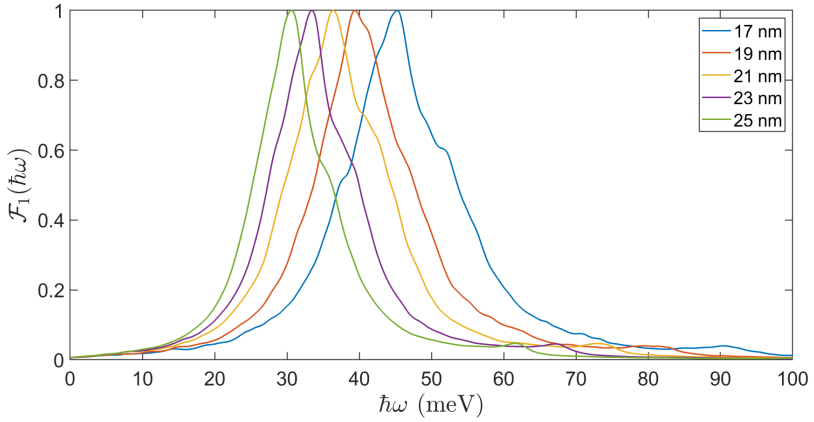


Figure 1.21: *Averaged spectrum of the dimensionless parameter related to the absorption probability (see Eq.* (1.26)*), for different GQD radii (from 17 to 25 nm).*

The averaged spectra in Figure 1.21 exhibit a bell-like shape for all considered sizes. We note that the maximum occurs for a photon energy $E_{max}(R) = \hbar\omega_{max}$, which decreases when $R$ is increased. Additionally, the broadening (spectral width at half maximum) also decreases when the GQD size is increased. These evolutions and the order of magnitude of

the energy $E_{max}(R)$ seem to indicate that a part of the absorption results from the coupling of an incident photon to two bulk states together.
We propose to confirm this assumption using the analytical expression of the bulk state energies of section 1.3.3. Therefore, we extract from the calculated absorption profile of Figure 1.21 the relevant following quantities $E_{max}(R)$, $E^{+}_{max}(R) = \hbar\omega^{+}_{max}$ and $E^{-}_{max}(R) = \hbar\omega^{-}_{max}$. Using (1.15), we consider the intraband transition $E_{m=0}(R) \rightarrow E_{m=1}(R)$ as the transition of highest energy:

$$E^{+}_{Bulk}(R) = \frac{\hbar v_F \left(\Theta^1_J(m=2) - \Theta^1_J(m=1)\right)}{R} \tag{1.27}$$

The lowest energy transition from a bulk state to another one can be expressed as:

$$E^{-}_{Bulk}(R) = \lim_{m\to\infty} \frac{\hbar v_F \left(\Theta^1_J(m+1) - \Theta^1_J(m)\right)}{R} \tag{1.28}$$

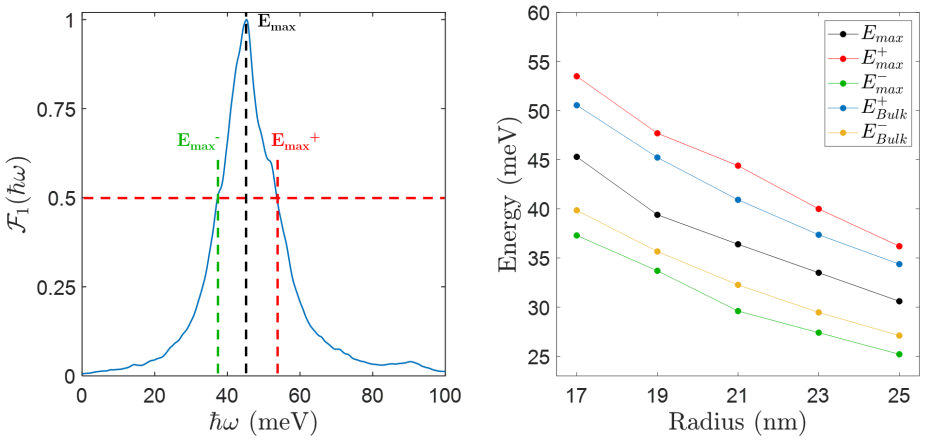


Figure 1.22: *(Left panel) For each averaged spectrum plotted in Figure 1.21, we extract the photon energy $E_{max}$ corresponding to highest value of $\mathcal{F}_\Gamma$, as well as the photon energies $E^{+}_{max}$ and $E^{-}_{max}$ such as $\mathcal{F}_\Gamma\left(E^{+}_{max} > E_{max}\right) = \mathcal{F}_\Gamma\left(E^{-}_{max} < E_{max}\right) = 0.5$, which illustrates the energy range of efficient absorption. The $\mathcal{F}_\Gamma$ curve for a GQD of radius $R = 17$ nm is plotted as an example. (Right panel) Evolution of the aforementioned quantities with respect to the GQD radius, with the same color code. The evolution of $E^{+/-}_{Bulk}$ as function of the GQD radius are also plotted, as illustrative examples of the absorption energy range if we only consider bulk $\rightarrow$ bulk transitions.*

We see on Figure 1.22 that $E_{max}$ belongs to the energy range $\left[E^{-}_{Bulk}, E^{+}_{Bulk}\right]$ and seems to scale as $1/R$. The upper energy limit $E^{+}_{max}$ is close to the considered highest energy intraband transition between two consecutive bulk states $E^{+}_{Bulk}$, indicating that the $Bulk \rightarrow Bulk$ transitions describe well the states involved in the absorption profile for $\hbar\omega \geq E_{max}$. However, when $\hbar\omega \leq E^{-}_{max}$, we note the existence of lower energy transitions contributing also efficiently to the absorption. These transitions cannot result from bulk states coupling as we see that $E^{-}_{max} < E^{-}_{Bulk}$, suggesting that other types of states couple efficiently to low-energy photons. We thus propose in the next section to investigate more in the detail which states are involved in the absorption and the nature of these efficient transitions.

### 1.4.3 Low energy intraband transitions

#### Interband and intraband transitions

In this section, we get back to the dimensionless quantity $f_{i,f}$ defined in (1.25). Figure 1.23 represents the normalised $f_{i,f}$ values in color scale for all possible initial and final energies

$(E_i, E_f)$, for $R = 25\ nm$[5].

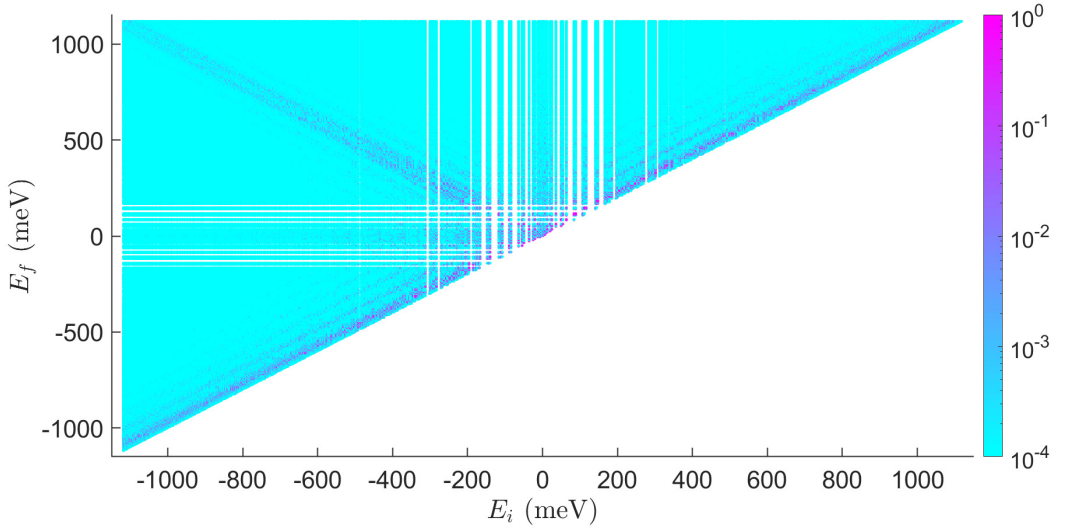


Figure 1.23: *Dimensionless parameter $f_{i,f}$ (color scale at the right) of Figure 1.20 (b) for $R = 25$ nm, plotted for each state of the GQD considered as a possible initial state $E_i$ (horizontal axis), towards all of its high energy states considered as possible final states $E_f$ (vertical axis).*

We note that a large proportion of state pairs are poorly coupled to light (cyan area). For highlighting the main energy levels involved in the absorption processes, we represent on Figure 1.24 only the $(E_i, E_f)$ pairs such as $f_{i,f} \geq 10^{-2}$. As a guide for the eyes, the dark and red dashed lines represent the transitions such as $E_f = E_i$ and $E_f = -E_i$ respectively.

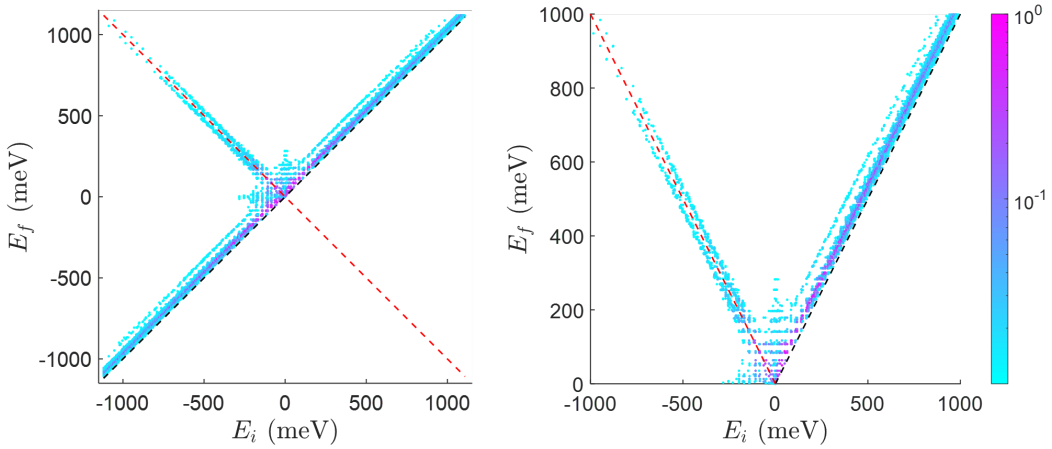


Figure 1.24: *(Left) Dimensionless parameter $f_{i,f}$ as plotted on Figure 1.23, by keeping the $(E_i, E_f)$ pairs such as $f_{i,f} \geq 10^{-2}$ and (right) restricted to positive final energies.*

Two different types of efficient transitions emerge from these plots. The points around the red dashed curve are similar to the interband transitions in graphene as they correspond to transitions for $E_i < 0$ such as $E_i \rightarrow E_f = -E_i \pm \epsilon$, with $0 \leq \epsilon \leq 40\ meV$ for $R = 25\ nm$. The same graphene-like feature is also present for smaller GQDs with $\epsilon$ smoothly decreasing

[5] As show in the previous section, the $f_{i,f}$ values show similar features for smaller GQDs. We thus restrict the discussion to one GQDs size for clarity.

when $R$ is increased. In the present case, we note that the interband transitions[6] are concentrated within the range $-750\ meV \leq E_i \leq -250\ meV$ and are less intense at lower energy. In the low-energy range, even if they have a non-negligible contribution to the absorption ($f_{i,f} \sim 0.1$), they do not represent its major part.

In contrast, the more efficient transitions ($f_{i,f} \sim 0.7$) appear to be concentrated in a line parallel to the dark dashed curve. These transitions are such as $E_f - E_i = cst$ all over the energy range, between same sign energies, and can thus be interpretated as intraband transitions by analogy with an infinite graphene sheet. We recover the previous section results $E_f - E_i = E_{max}(R = 25\ nm) \approx 30\ meV$ which indicates that the main contribution to the GQDs absorption comes from intraband transitions. The additional parallel line also refers to intraband transitions, less efficient, with $E_f - E_i \approx 110\ meV$, which are also visible in Figure 1.20.

### State identification

In previous section, based on the wavefunctions spatial integral $I_{0.85}$, we have classified the energy levels of the GQDs spectrum in three groups: edges, mixed and bulk states. In order to identify the wavefunctions which efficiently couple to a low-energy excitation, we select some states of each type and study their coupling with the other types of energy levels through some examples.

**Edge states** We start by looking at how the edge states that lie at very low energy couple to the other types (see Table 1.2). Figure 1.25 shows a zoom of Figure 1.24 for low values of the initial energy $E_i$. We first note that in this energy range, all the possible transitions are almost ineffective. Indeed, if an edge state of energy $E_i = 1.49\ meV$ is as the initial states,the maximum coupling to another edge state, a mixed and the first bulk state, with respective final energies of $E_f = 3.12\ meV$, $E_f = 83.8\ meV$ and $E_f = 107.2\ meV$, is limited to $f_{edge \to edge} \sim 7.7.10^{-2} \ll 1$. This result confirms that the edge states of energy pinned at the Dirac point or those with a very low energy do not couple to light.

| $Energy\ (meV)$ | 1.49 | 3.12 | 83.8 | 107.2 |
|---|---|---|---|---|
| $I_{0.85}$ | $8.76.10^{-2}$ | 0.14 | 0.7 | 0.85 |
| $Type$ | $Edge$ | $Edge$ | $Mixed$ | $Bulk$ |

Table 1.2: *Energy, probability amplitude over 85% of the radius $I_{0.85}$ and category of few states of a $R = 25$ nm GQD.*

**Mixed and bulk states** We now focus on the mixed states presented in Table 1.3.

| $Energy\ (meV)$ | 35.26 | 49.93 | 54.73 | 63.67 | 83.8 | 84.12 | 88.07 | 107.3 |
|---|---|---|---|---|---|---|---|---|
| $I_{0.85}$ | 0.49 | 0.52 | 0.57 | 0.66 | 0.7 | 0.67 | 0.74 | 0.85 |
| $Type$ | $Mixed$ | $Mixed$ | $Mixed$ | $Mixed$ | $Mixed$ | $Mixed$ | $Mixed$ | $Bulk$ |

Table 1.3: *Energy, probability amplitude over 85% of the radius $I_{0.85}$ and category of few states of a $R = 25$ nm GQD.*

We see on Figure 1.26 that they couple together very efficiently ($f_{i,f} \sim 0.7$). As developed

[6] As the GQDs have a discrete energy spectrum, we may not refer to the "band" term. A more correct qualification for the observed interband/intraband transitions thus should be inter-levels/inter-sub-levels respectively. Nevertheless, we will use the first terminology to lighten up the speech.

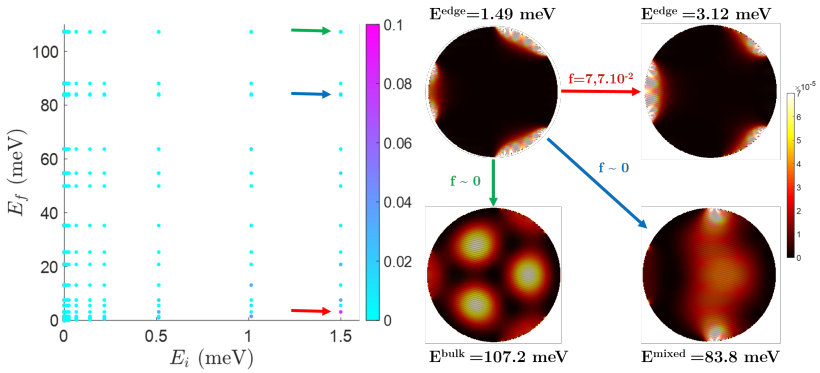


Figure 1.25: *Probability densities (according to the right colour bar) for the wavefunctions of four states of a $R = 25$ nm GQD, selected from Table 1.2. The dimensionless parameter $f_{i,f}$ for the transitions indicated by arrows relying the probability distributions are given near the corresponding arrow. The three transitions are also represented by arrows of same colour in the left $(E_i, E_f)$ panel.*

in section 1.3.2, these states are by far the most numerous and thus will dominate the absorption probability spectra of large GQDs.

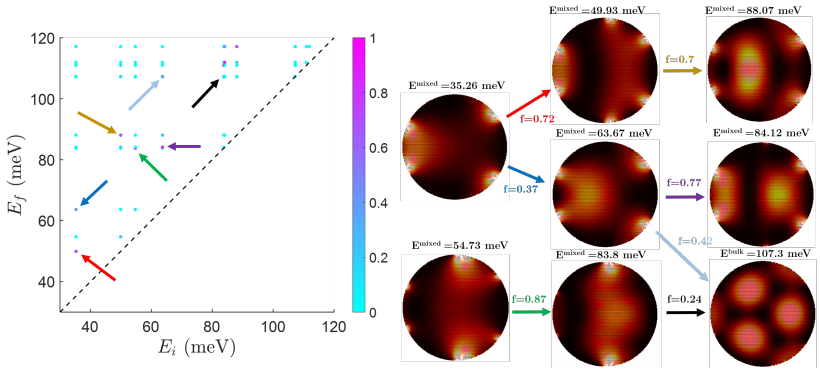


Figure 1.26: *Probability densities (according to the right colour bar of the previous figure) for the wavefunctions of various states of a $R = 25$ nm GQD, selected from Table 1.3. The dimensionless parameter $f_{i,f}$ for the transitions indicated by arrows relying the probability distributions are given near the corresponding arrow. The different transitions are also represented by arrows of same colour on the left $(E_i, E_f)$ panel.*

### 1.4.4 Influence of size, temperature and doping

We have seen in the previous section that photons of few tens of meV couple very efficiently to the low-energy mixed states and efficiently the bulk states via intraband transitions. Obviously, in a real system, these transitions are achievable if the initial state is occupied and the final state empty. Regarding the inhomogeneous density of energy pairs $(E_i, E_f)$ with an efficient $f_{i,f}$, the absorption probability of a GQD is expected to drastically depend on the Fermi level.

In order to compute the absorption probability spectrum $\alpha(\hbar\omega)$, we replace the Dirac distributions of Equation (1.24) by Lorentzian functions $\mathcal{L}_\Gamma\left(E_f - E_i \ ; \ \hbar\omega\right)$ of half-widt-at-half

maximum $\Gamma$ :

$$\mathcal{L}_\Gamma\left(E_f - E_i\ ;\hbar\omega\right) = \frac{\Gamma/\pi}{\Gamma^2 + \left(E_f - E_i \pm \hbar\omega\right)^2} \tag{1.29}$$

The phenomenological parameter $\Gamma$ is fixed at 5 meV, that is smaller or even much smaller than the typical width in Figure 1.21 (section 1.4.2). We thus investigate the complete determination of the absorption probability spectra $\alpha(\hbar\omega)$ of large GQDs while varying their size, temperature and doping level.

### Zero-temperature without doping

For a zero-temperature system, with a Fermi level $E_F = 0$, all the states with a negative energy are filled and all the states with a positive energy are empty. Consequently, only interband transitions such as $E_i < 0 \rightarrow E_f > 0$ are allowed. To figure out the main features of the absorption over a large range of energy, we represent on Figure 1.27 the absorption probability spetcra $\alpha(\hbar\omega)$ for GQDs of radii $R = 17$, 21 and 25 $nm$. Over the all range of

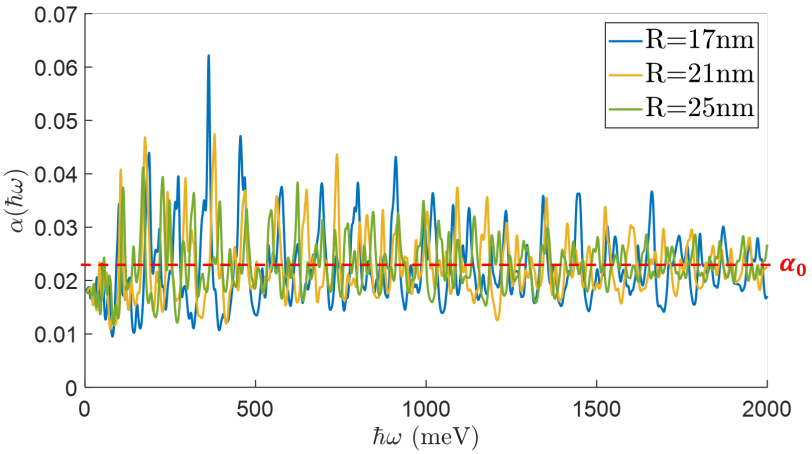


Figure 1.27: *Absorption probability spectra for undoped GQDs of different radius, at $T = 0$ K.*

energy, we see that $\alpha(\hbar\omega)$ fluctuates around a constant value $\alpha_0$, whatever the GQD size. We interpret this value as the linear optical response of a monolayer graphene sheet, characterised by an interband absorption of $\alpha_0 = \frac{e^2}{4\pi\epsilon_0\hbar c} = 2.3\%$. Therefore, the tight-binding model shows that the interband absorption of large GQDs is relatively similar to the interband absorption of monolayer graphene.

### Doping influence at zero-temperature

To illustrate the doping influence at zero-temperature, we represent on Figure 1.28 the absorption probability $\alpha(\hbar\omega)$ for $R = 25$ $nm$ for different Fermi energies. At low doping, $E_F \leq 20$ $meV$, the absorption does not show any clear energy signature and is on the order of $\alpha_0$. Although a low Fermi level allows the very efficient low-energy transitions mentioned in the previous section, the number of these transitions remains small compared to all the other inefficient transitions in this energy range, resulting to a flat absorption. However, when $E_F = 50$ $meV$, the number of energy pairs $(E_i, E_f)$ with an efficient $f_{i,f}$ starts to be high enough to increase by a factor 2 the absorption at low energy.
For $E_F \geq 100$ $meV$, the absorption exhibits a sharp peak around 30 $meV$ due to the activation of all the efficient intraband transitions. An important result of this work is that the absorption reaches more than 20% and 40 % for $E_F = 200$ $meV$ and 300 $meV$ respectively.

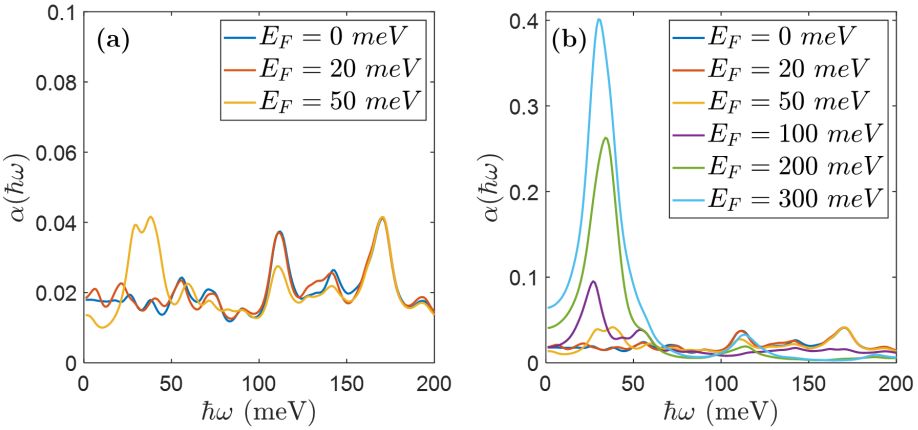


Figure 1.28: *Absorption probability spectra for a doped GQD of radius $R = 25$ nm, at $T = 0$ K. (a) Low doping and (b) low to high doping evolution.*

Such large absorption is extremely promising for the development of optoelectronic and photonic devices operating in the THz spectral range. The main absorption peak is followed by a decrease of the absorption below $\alpha_0$ at higher energy, as seen in Figure 1.29, indicating less efficient intraband absorptions (denoted by the additional dashed line in Figure 1.24). $\alpha(\hbar\omega)$ finally tends as expected to $\alpha_0$ due to interband transitions when $\hbar\omega \geq 2E_F$.

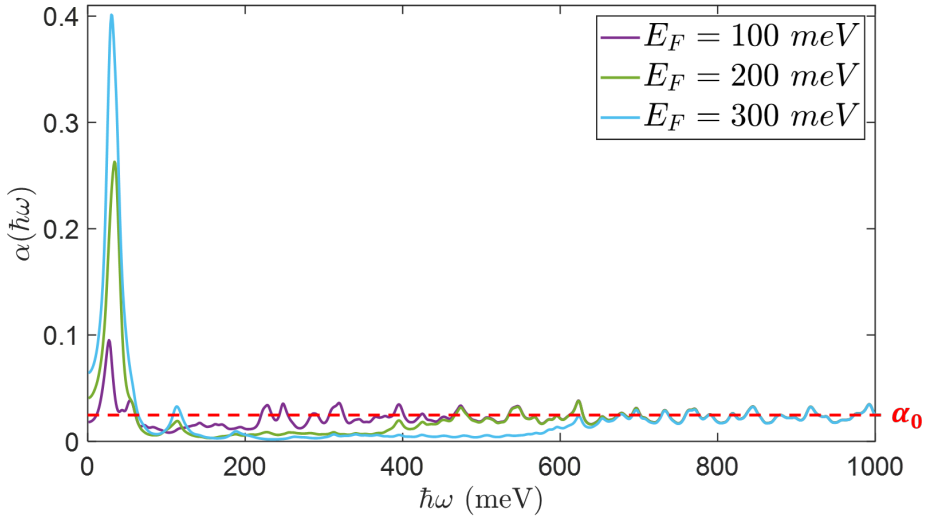


Figure 1.29: *Absorption probability spectra for a GQD of radius $R = 25$ nm, at $T = 0$ K, for three doping values, as presented in Figure 1.28 but extended up to higher photon energies..*

### Temperature influence for different doping values

We represent on Figure 1.30 the absorption at low doping values, for $T = 4.7\ K$ and $T = 300\ K$. These two temperatures corresponds to the temperatures at which the experimental characterization presented in the next chapter have been conducted.
When the temperature is increased, due to the Fermi distribution profile of the carrier occupation, the energy levels occupancy decreases below $E_F$ and increases above $E_F$, on a typical energy range of $\sim k_B T$. We restrict our analysis to low energy photons $\hbar\omega \leq 200\ meV$ since, at higher energy, $\alpha(\hbar\omega)$ is almost insensitive to temperature: the absorption arises from

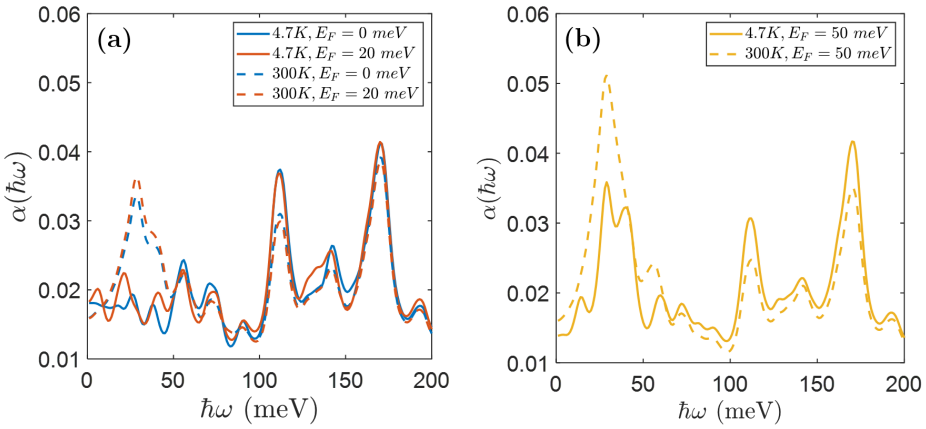


Figure 1.30: *Low-energy photon absorption probability spectra for doped GQDs of radius $R = 25$ nm, at low and high temperatures, for different doping contents.*

interband transitions when $\hbar\omega \geq 2E_F$ and $k_B T_{300K} \approx 26\ meV \ll 2E_F$.

For $0 \leq E_F \leq 20\ meV$, an increase of the temperature leads to the activation of efficient intraband transitions around 30 $meV$ and thus an increase of the absorption. Subsequently, the absorption due to higher energy intraband transitions around 110 $meV$ is reduced by Pauli exclusion principle. For $E_F = 50\ meV$, the absorption around 30 $meV$ is enhanced by almost a factor 2 when the temperature is increased as the number of allowed efficient intraband transitions becomes more significant.

The enhancement of the absorption when the temperature is increased starts to become less important in high doping regime. As seen on Figure 1.31, up to $E_F = 100\ meV$, the increase is small ($\alpha_{300K}/\alpha_{4.7K} \simeq 1.01$) and the temperature mainly broadens the absorption profile. When $E_F \geq 200\ meV$, the absorption is slightly lowered and its bandwidth remains unchanged.

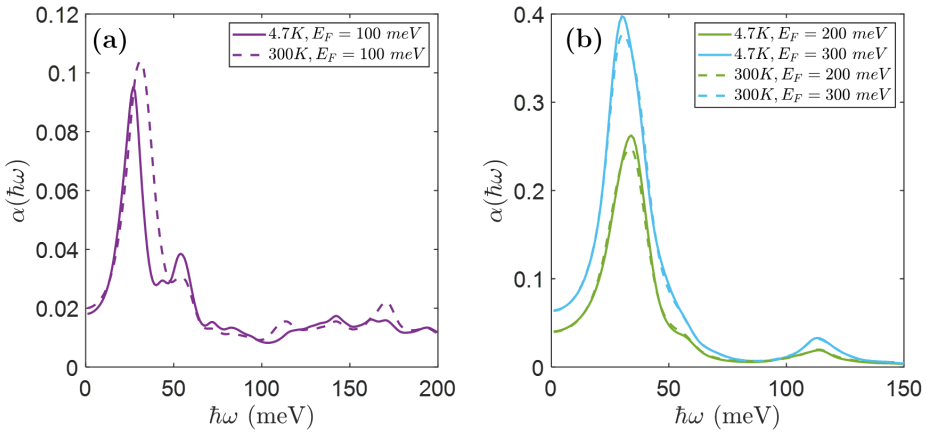


Figure 1.31: *Low-energy photon absorption probability spectra for doped GQDs of radius $R = 25$ nm, at low and high temperatures, for different doping contents.*

### Influence of the GQD size

We now investigate the influence of the GQD size on the absorption profile, at $T = 4.7\ K$ and $300\ K$. We focus on two cases: $E_F = 20\ meV$ for the low doping regime, which corresponds to our experimental conditions (see next chapter) and $E_F = 200\ meV$ as an example of the high doping regime.

When $E_F = 20\ meV$ (Figure 1.32), at low temperature, there is no clear influence of the GQD size on the low energy absorption ($\hbar\omega \leq 80\ meV$). Surprisingly, the small absorption peak around $110\ meV$ is shifted to higher energies when $R$ is increased whatever the temperature, in contrast with the $1/R$ general tendency of the absorption profile (Figure 1.22). At $T = 300\ K$, we recover the $1/R$ tendency for the low energy intraband transition: as the GQD size increases, the absorption becomes narrower and shifts to lower energies.

The influence of the GQD size on the absorption is, however, clearly perceptible in the

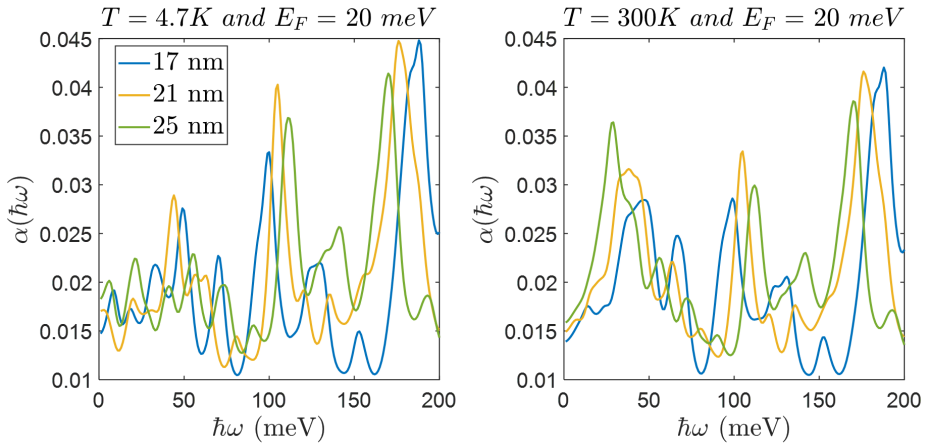


Figure 1.32: *Low-energy photon absorption probability spectra for lightly doped GQDs of different radii at low (left) and high (right) temperatures.*

high doping regime (Figure 1.33). At $T = 300\ K$, the sharp resonances at low energy and the smooth ones at higher energy both shift to lower energies when $R$ increases. In the low temperature case, we also observe a similar shift in energy.

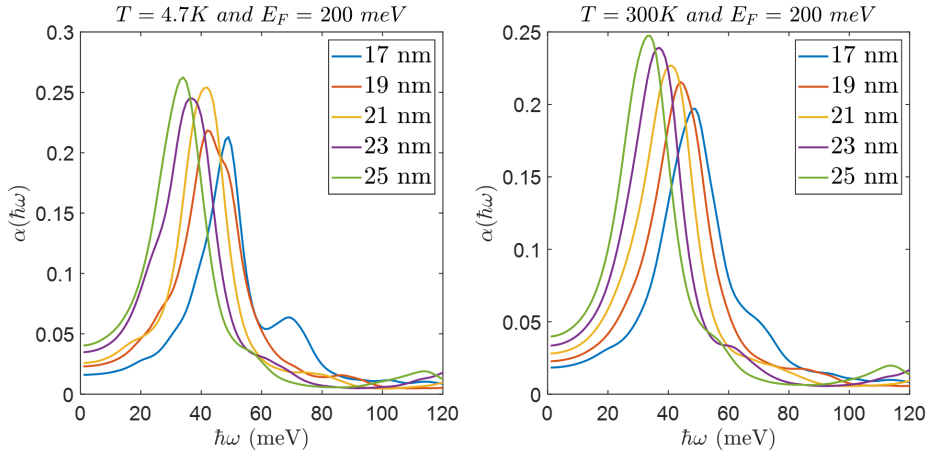


Figure 1.33: *Low-energy photon absorption probability spectra for an important doping of GQDs of different radii at low (left) and high (right) temperatures.*

### 1.4.5 Conclusion

We demonstrate the possibility of engineering the energy spectrum of a GQD, and their optical properties, by simply defining their size and doping. Furtheremore, we found that this tunability remains robust no matter the edge structure of the GQD.

Our analysis of the electronic state distribution of large GQDs shows the existence of three different types of states. The first type refers to edge states that are strongly localised on the edge of the GQDs. The second type corresponds to wavefunctions mostly localised on the bulk and that are thus defined as bulk states. The third type corresponds to mixed-states as they extend from the edges to the center of the GQD.

Based on this knowledge, we have demonstrated that photons of few tens of meV couple very efficiently to the low-energy mixed states and efficiently the bulk states via intraband transitions, which lead to a large absorption resonance at THz frequencies. An important result of this work is that the absorption reaches more than 20% and 40 % for $E_F = 200\ meV$ and 300 $meV$ respectively. Such large absorption is extremely promising for the development of optoelectronic and photonic devices operating in the THz spectral range.

As perspectives, the model can be developed to calculate the hot carriers dynamics (by including carrier-carrier interaction, carrier-optical phonon scattering and carrier-acoustic phonon) to determine if Auger recombinations can be suppressed. These attractive outlooks would reveal the possibility to achieve optical gain at THz frequencies.

# Chapter 2

# THz spectroscopy of multilayer epitaxial graphene and graphene quantum dots

In the previous chapter, we have shown that reducing the spatial extension of a graphene monolayer down to circular quantum dots of few tens of nanometers in diameter leads to the full discretization of its electronic states. We have calculated the absorption probability $\alpha(\omega)$ of a monolayer GQD and demonstrate that it can efficiently couple with photons of meV energy and thus yield to pronounced absorption in the THz spectral range. This chapter is devoted to the fabrication arrays of GQDs and the experimental investigation of their absorption properties at THz frequencies using THz time-domain spectroscopy system. As the GQDs are processed from multilayer epitaxial graphene grown on Silicon Carbide (SiC) substrate, we start experiments by probing the THz intraband and interband response of multilayer epitaxial graphene.

This chapter starts with a brief review of previous works on the graphene conductivity in the THz spectral range. This is followed by the a general description of THz-TDS experiment. Next, I present in-depth investigation of the intraband and intraband conductivity of multilayer epitaxial graphene performed using THz-TDS system. Finally, I present the investigation of the THz properties of GQDs. I first start this part with a description of how we have progressed on the fabrication procedure. Secondly I show the experimental optical response of the GQDs at THz frequencies. Then, I compare these original results to theoretical predictions. Finally, I present preliminary results on the carriers dynamics in these graphene based materials using optical pump-THz probe experiment.

## THz spectroscopy of graphene and related materials

THz spectroscopy has become an exciting technique for probing and characterizing a variety of low-energy physical phenomena from atomic transitions to the vibrations of biological molecules. THz spectroscopy is based on the interaction between the electromagnetic field and the electric or magnetic dipoles contained in matter. These interactions with matter affect the propagation of THz waves, which leave a spectral signature, permitting to identify the matter as well as understanding its properties. This make THz spectroscopy systems very attractive for a wide range of disciplines including physics, chemistry, engineering, astronomy, biology, and medicine. In the field of materials science, THz spectroscopy is ideally suited to measure mobile charge carriers since they reflect and absorb THz radiation. THz

spectroscopy has been used to measure conductivity, topological insulators, and superconductors, as well as phase transitions in these materials. Furthermore, 2D materials like bismuth selenide ($Bi_2Se_3$) and graphene have been studied.

THz spectroscopy gives access to both interband transitions and intraband transitions in graphene due to its zero bandgap, in stark contrast to conventional semiconductor materials. However, as discussed in the Introduction, the interband conductivity at THz frequencies is not zero only in quasi-intrinsic graphene layers (i.e. for $E_F$<2 meV) due to Pauli blocking effect. As the fabrication of quasi-intrinsic graphene layer remains extremely challenging, most of THz-TDS experiments have been focused on doped graphene, revealing that THz photons are excellent probes of intraband dynamics.

Initially, the free carrier absorption in graphene (or intra-band response) has been measured using broadband Fourier-transform IR spectroscopy (FTIR) [42, 43, 44]. Even though the FTIR spectroscopy is a powerful tool, which provides a broad spectral range, it lacks the phase sensitivity as typically only power transmission or reflection spectra are recorded. In contrast, THz-TDS experiment, which measures the time-resolved electric fields of THz radiation propagating through a medium and compared to a reference, enables phase-resolved measurements of the complex optical conductivity of the material of interest without requiring the use of Kramers-Kronig relation. This THz-TDS technique has been widely use to probe the complex intraband conductivity spectra (free carrier absorption) of graphene samples [45]. Moreover, this THz-TDS technique has been applied to spatially map the THz intraband conductivity of a large area CVD sample [46]. The inhomogeneity in THz intraband conductivity provides information on variations in doping level and the influence of microscale defects [47, 48]. Thus, THz-TDS has potential as a fast, non-contact and non-destructive effective tool to evaluate the homogeneity and uniformity of fabricated graphene layers. Further studies of intraband graphene conductivity have combined gate voltage or an organic dopant on CVD-grown graphene to modulate the carrier density [49] and THz-TDS experiment.

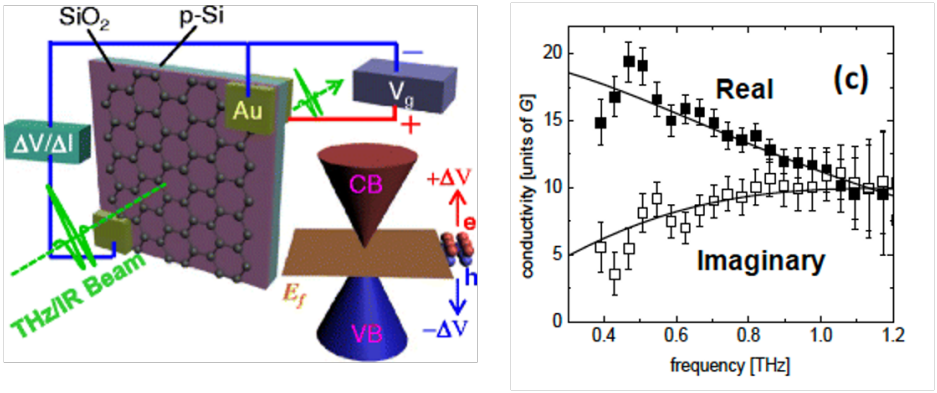


Figure 2.1: *Left: Sketch of agated large-area graphene device fabricated, together with the incident and transmitted THz beams. Reproduced from Reference [50]. Right: Extracted linear THz conductivity of the graphene sample, normalized by* $G_0 = e^2/4$ *, with solid lines representing the fit result using Drude model. As fit parameters we obtain a momentum scattering time* $\tau$*=140 fs, and a Fermi level of* $E_F$*= 0.07 eV. Reproduced from Reference [51].*

All these previous works have established that the optical intraband conductivity of doped graphene in the THz frequency range follows the Drude model together with its square root dependence on the carrier concentration [52]. A typical THz conductivity spectrum of a

doped CVD-grown graphene is presented in Figure 2.1. By analysing the spectral shape of the THz conductance with appropriate models, one can determines the Fermi energy and scattering times of the graphene layer [50]. For instance, measurements on high-quality large-area CVD graphene has revealed electron momentum scattering time of 140 fs, which corresponds to mean free paths of 140 nm. THz-TDS measurements have been also applied to probe THz conductivity of multilayer epitaxial graphene grown on SiC. More recently, the applicability of this THz-TDS technique to spatially map the carrier density and mobility has been extended to epitaxial graphene grown on SiC [53, 54]. However, the investigation of the THz conductivity of exfoliated graphene layers are uncommon [55]. The raison is that the largest dimension of exfoliated graphene is limited to typically 100 $\mu m$ x100 $\mu m$ is weak compared to radiation wavelength in the THz range (typically ∼300 $\mu$m), preventing for the possibility to extract relevant information from measurements. Regarding graphene nanostructures, only very few works have been reported on the study of the THz conductivity and all these works have only probed the transport of free carriers within the nanostructures. For instance, the intraband conductivity of graphene nanoribbons with optical band gaps in the visible spectral range has been studied by THz TDS experiments, showing THz conductivity spectra well described by the Drude-Smith model [56].

In this thesis work, we only focus on the linear response of the THz graphene conductivity. But, it is interesting to mention recent works that have demonstrated that, despite the low photon energy of THz waves (∼4 meV), a THz pulse can carry an immense field strength thus allowing highly nonlinear phenomena in single-layer graphene, such as generation of THz harmonics up to the seventh order at room temperature [51] [57].

From this brief state of the art, we can underline that in spite of intensive works on intraband conductivity in graphene in the THz spectral range, the study of the interband conductivity in graphene remains elusive at THz frequencies. Moreover, we can point out that there is no experimental report on the intraband and interband conductivity of graphene quantum dots in the THz spectral range.

## 2.1 THz time-domain spectroscopy

### 2.1.1 Principle of THz-TDS system

In this section, we describe the general principle of the THz-TDS system used in this work to probe the THz properties of multilayer epitaxial graphene and GQDs. THz-TDS systems are based on a ultrafast optical laser that delivers a pulse train of femtosecond (fs) pulses. A schematic view of the experimental set-up is presented in Figure 2.2. The ultrafast optical laser is a femtosecond Ti:sapphire oscillator, which delivers horizontally polarized femtosecond pulses at a center wavelength in the infrared tange ($\lambda_0 \sim 800\ nm$), with a typical spectral bandwidth $\delta\lambda$ around 100 nm and a repetition rate of 80 MHz. The average power is about 850 mW. A pulse compressor is placed right after the laser to reduce the optical pulse duration down to 15 fs (i.e. near the Fourier limit ∼ 10 fs). Such short pulses are crucial for a broadband THz generation and detection. The infrared beam is then separated in two beams by a beam splitter: 80% of the power for the "TDS pump line" (1) and 20% for the "TDS probe line" (2), respectively dedicated to the THz emission and detection.

The infrared beam on the path (1) illuminates an electrically biased photoconductive antenna that produces a THz pulse. The emitted THz pulses are focused by paraboloidal mirrors onto the sample and then onto an electro-optic crystal used as THz detector. On

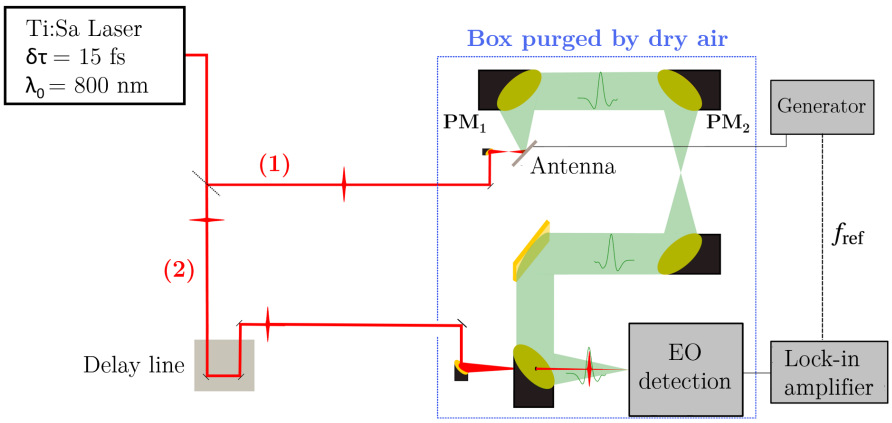


Figure 2.2: *Sketch of the experimental THz-TDS setup. The infrared beam is depicted in red and the THz beam in green. The area where the THz pulse is generated and propagates is placed in a box purged by dry air in order to reduce THz absorption induced by water molecules in the air.*

the "TDS probe line" (2), the infrared beam travels on a motorized optical delay line (that modifies the path length) and then is focused onto the electro-optic crystal. By moving the delay line and then acting on the temporal delay between the infrared pulse and the THz pulse that are mixed in the electro-optic crystal, we are able to synchronously sample the transient THz electric field and reconstruct its temporal profile. This scheme imposes stability requirements on the output of the laser to ensure that every laser pulse generates the same THz pulse. In addition, the THz beam path is enclosed in a box purged by dry air to reduce the humidity down to 0.1%, thus strongly reducing the THz absorption by the water molecules of the air.

The signal read-out from the THz detector is performed via a lock-an amplifier. A lock-in amplifier is a system that selectively amplifies a signal at a given reference frequency $f$ and then applies an adjustable low-pass filter to the result. Thereby it isolates the signal at the frequency of interest from all other frequency components. To this end, we apply a square wave bias voltage to the photoconductive antenna to switch the THz generation on and off at the desired reference frequency. By that means, one can detect very small signals within a noisy background.

### THz generation

Several techniques are used for THz generation such as nonlinear crystal, air-plasma source, ultrafast spin currents in ferromagnetic/nonmagnetic metal nanostructures and photoconductive antenna. They all have their advantages and disadvantages. The first three families of emitters require the use of an optical chopper to modulate the THz generation for the lock-in detection, which is limited to typically 10 kHz. However, to limit the $1/f$ frequency noise of the laser, higher modulation frequency is desired. In this work, we use a photoconductive antenna for the THz generation as it can be modulated at high frequency (few ten of kHz) for lock-in detection providing larger signal-to-noise ratio for the THz TDS system. Common THz photoconductive antenna consists in a dipole-like metallic electrodes deposited on a Gallium Arsenide substrate as illustrated in Figure 2.3 [58].

The antenna is polarized by a DC voltage of few volts, which creates an electrostatic field between the two electrodes. By illuminating the GaAs material with (sub-)picosecond

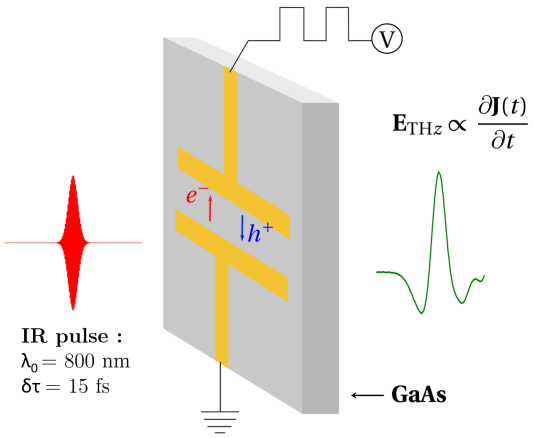


Figure 2.3: *Scheme of a photoconductive dipole antenna on a GaAs substrate excited by a femtosecond infrared pulse (red). The infrared beam generates carriers that are accelerated by the electric field induced by bias voltage applied to antenna electrodes, leading to the emission of a radiation at THz frequencies (green).*

infrared pulse of energy $E \sim 1.55\ eV$ higher than the bandgap energy of GaAs (1.424 $eV$ at room temperature), electron-hole pairs are photocreated between the electrodes. The photoexcited charges are accelerated by the electrostatic field in opposite direction, which gives rise to a transient current $J(t)$. Since the transient photocurrent oscillates in a picosecond scale, it leads to the emission of radiation at THz frequencies in the far field, which is proportional to the time derivative of the photocurrent :

$$E(r,t) = \frac{L}{4\pi\epsilon_0 c^2 r}\frac{\partial J(t)}{\partial t}$$

with $L$ the distance between the electrodes and $r$ the distance from the antenna. The rising time of the transient current is determined by the infrared pulse duration and its decay time is governed by the photoexcited carrier lifetime in GaAs. The temporal scale of the generated transient current directly determines the spectral range of the radiated electric field $E(r,t)$.

It has been shown that the overall THz radiation emitted by the dipole photoconductive antenna includes contribution from the photocurrent within the gap but also from the antenna structure. However, due to its small dimensions, dipolar photoconductive antennas behave like ponctual sources, meaning the THz radiation at all frequencies is diffracted and a Si lens needs to be added on the back of the photoconductive antenna to fully collect the emitted THz electric field. To overcome this need, large dipolar antennas that allow an higher and more directive THz emission have been developed, with a size ranging from 100 $\mu m^2$ to 1 $mm^2$. Nevertheless, the voltage to be applied between the electrodes of such a large structure reaches about few kV. To overcome this issue, in this work, we use a homemade interdigitated photoconductive antenna (see Figure 2.4) that combines the assets of the two aforementioned concepts: closed enough electrodes to apply bias within the range of few volts and a large active area of emission to generate high amplitude and more directive THz electric field [59]. It is composed by 150 nm thick Au electrodes deposited on a GaAs substrate. Anodes and cathodes periodically alternate with a 2 $\mu m$ spacing between two consecutive electrodes, and the total surface area is $500\mu m \times 500\mu m$. The periodicity between anodes and cathodes induces periodic opposite phase emitted electric field, leading to destructive interferences. To tackle this problem, half of the spacing between the digits is covered by a 150 nm thick Au mask, separated from the electrodes by an insulating layer of

$SiO_2$.

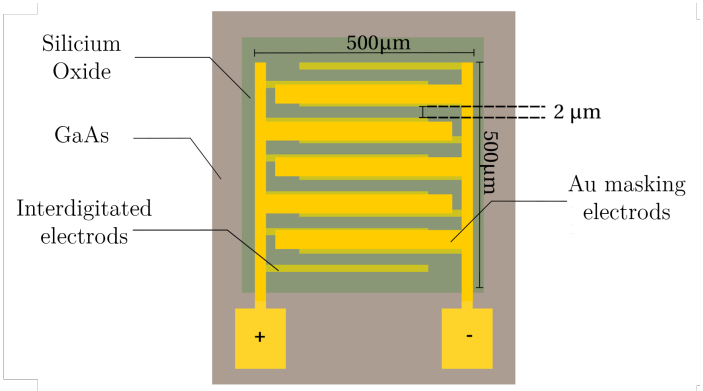


Figure 2.4: *Scheme of the interdigitated photoconductive antenna on low-temperature-grown (LT) GaAs used in our THz-TDS setup. It is composed by interdigitated gold electrodes, covered by an insulating layer of silicium oxide and gold masking electrodes to avoid destructive interferences.*

We fabricated the photoconductive antennas on low-temperature-grown (LT) GaAs since LT-GaAs has a very high breakdown field 500 kV/cm and a subpicosecond carrier lifetime along with reasonably good mobility. It is regarded as one of the best materials as the active layer for photoconductive devices driven by 800 nm wavelength optical pulses. The LT GaAs layer, of 2 $\mu$m thick, was grown by MBE epitaxy on a semi-insulating GaAs substrate. Consequently, when the photoconductive antenna is illuminated with an 15 fs infrared pulse, the emitted electric field is a (sub)picosecond pulse with a broadband spectrum ranging from 0.3 to 20 THz.

**THz detection**

THz detector in usual TDS systems are either photoconductive antennas or electro-optic crystals. In our system, we use an electro-optic crystal and exploit the second order non-linear effect that occurs in the crystal when both THz waves and optical probe pulses are present, the Pockels effect. Simply, this effect is a birefringence induced by the THz electric field pulse. When an infrared pulse - which acts as a sampling probe - propagates in the crystal, its phase is modified by the THz induced birefringence. As the 15 fs infrared pulse is much shorter than the picosecond THz pulse, when the infrared pulse overlaps the THz pulse in the crystal at a certain time $\tau$, the phase shift is proportional to the THz electric field zt this time $E_{THz}(\tau)$. By moving the delay line, we can time shift the overlap of the two pulses and then sample the whole THz pulse profile, as shown in Figure 2.5.

After passing through the electro-optic crystal, the infrared pulse phase shift is measured by ellipsometry with a quarter-wave plate, a Wollaston prism and balanced photodiodes, as presented in Figure 2.6. The quarter-wave plate adds a phase shift of $\pi/2$ to the vertical component of the polarization with respect to the horizontal one. The Wollaston prism then projects the orthogonal components of the polarization in two different directions in space, and each beam is focused on the balanced photodiodes. The intensity difference $\Delta I$ between the photodiodes is thus proportional to the phase shift induced by the THz field, and consequently to the THz electric field value $E_{THz}(t)$. The measured photocurrent difference $\Delta I$ is linked to the THz electric field as [60]

$$\Delta I(\tau) = \int_{-\infty}^{+\infty} d\omega E_{THz}(\omega) f(\omega) exp(-i\omega\tau) \tag{2.1}$$

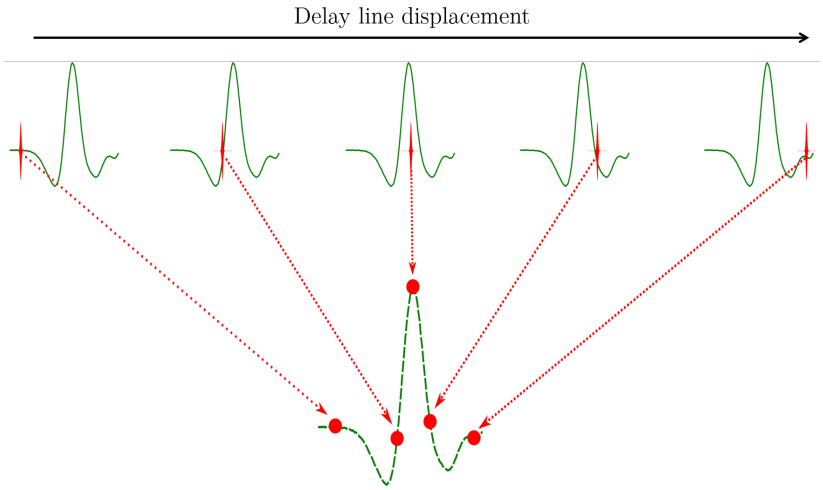


Figure 2.5: *Schematic of the principle of electro-optical sampling of a THz pulse profile. The infrared pulse shifts in time thanks to the delay line displacement to probe different points of the THz temporal profile.*

where, $\tau$ is the relative delay between the optical and the THz pulses, $f(\omega)$ expresses in the frequency domain the response function of the electro-optic crystal in frequency space, which involves the electro-optical coefficient and the phase agreement between the components of the infrared pulse at frequency $\omega_0$ and the components of the THz field at frequency $\omega$ and $E_{THz}(\omega)$ is the THz electric field in frequency space.

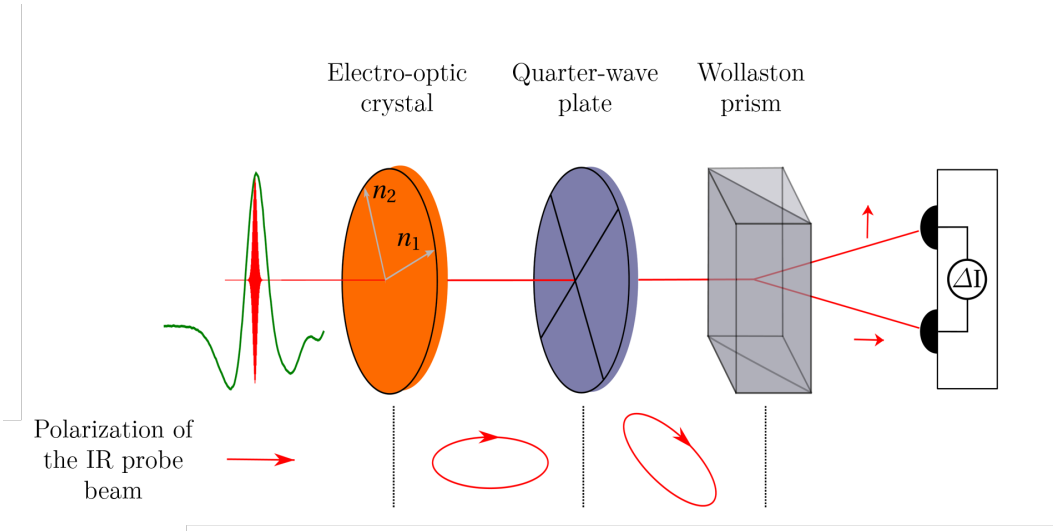


Figure 2.6: *Scheme of electro-optical detection. Red arrows represent the infrared probe polarization in the plane perpendicular to the direction of propagation. The infrared beam is phase-shifted by the THz induced birefringence in the electro-optical crystal. The quarter-wave plate adds a phase shift of $\pi/2$ to the vertical component of the polarization with respect to the horizontal one. The Wollaston prism projects the orthogonal components of the polarization on two photodiodes and the intensity difference $\Delta I$ is measured.*

In this thesis, we use two different electro-optic crystals: Zinc Telluride (ZnTe) and Gallium Phosphide (GaP) crystals. The choice of the crystal is driven by the spectral range we want to investigate. For these two electro-optic crystals, the function $f(\omega)$ can be considered as constant and the photocurrent difference $\Delta I$ is expressed as :

$$\Delta I(\tau) = I_p \frac{\omega_0 n^3 r_{41} L}{2c} E_{THz}(\tau) \tag{2.2}$$

where $I_p$ is the intensity of the near infrared beam, $n$ is the optical index of the crystal in the near infrared ($\lambda = 800$ nm), $r_{41}$ is the electro-optical coefficient [61, 62] and $L$ is the thickness of the crystal.

The performances of the THz-TDS system that uses a 2 mm thick ZnTe for the electro-optic detection are presented in Figure 2.7. The time-resolved amplitude of the electric field is shown in Figure 2.7 (a). The temporal resolution set by the delay line step between two consecutive acquired points is 8 fs[1], and the lock-in amplifier integration time constant for each point is set to 100 ms. The calculated amplitude of the Fourier transform of the temporal signal is represented in Figure 2.7 (b). We define the detection bandwidth of the TDS system as the spectral range where the amplitude is higher than the noise level. Consequently, the bandwidth for a 2 mm thick ZnTe crystal ranges from 0.1 THz to 4 THz, with a signal-to-noise ratio of $\sim 30$.

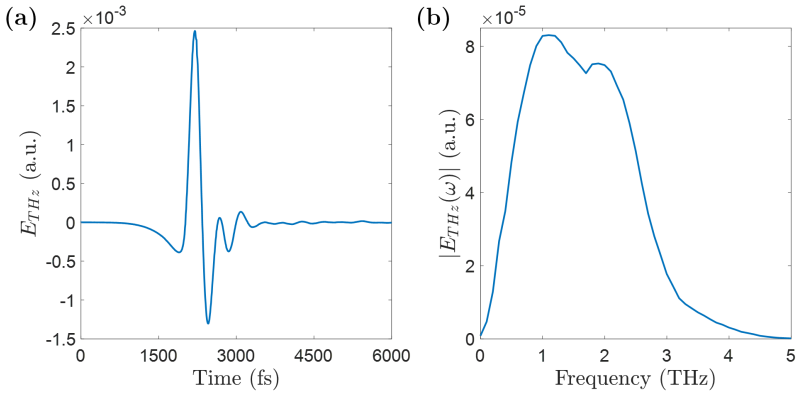


Figure 2.7: *Time-resolved electric field amplitude (a) and its corresponding spectrum (b) using 2 mm-thick ZnTe electro-optic crystal.*

Figure 2.8 shows the results obtained for a 100 $\mu m$ thick GaP crystal. In this case, the bandwidth ranges from 0.3 THz to 7 THz, with a signal-to-noise ratio of $\sim 25$.
The absolute and normalized amplitude spectrum of these two crystals are compared respectively in Figure 2.9. We see that the GaP crystal is well adapted for a broadband acquisition, especially if we are interested in the frequencies higher than 4 THz. However, if we want to focus on the low frequency part of the spectrum, ZnTe crystal is better suited as it shows a higher absolute signal than GaP in this frequency range.

### 2.1.2 Diffraction limited focusing of the THz electric field

In order to probe the GQD using our THz TDS system, an important point that have to be considered is the focusing of the THz beam. Indeed, considering the long wavelength of THz radiation (300 $\mu m$ at 1 THz), it is unrealistic to optically probe a single GQD with a diameter of few tens of nanometers, even if the THz beam is focused down to the diffraction limit. In order to address this issue, we decided instead to fabricate and probe a $S_{tot} \sim 1\ mm^2$ array of GQDs, as depicted in Figure 2.18. This is the largest array we are able to fabricate

[1]This temporal step is aimed to well resolve the temporal profile, and allows a high enough cutoff frequency according to Shannon criteria.

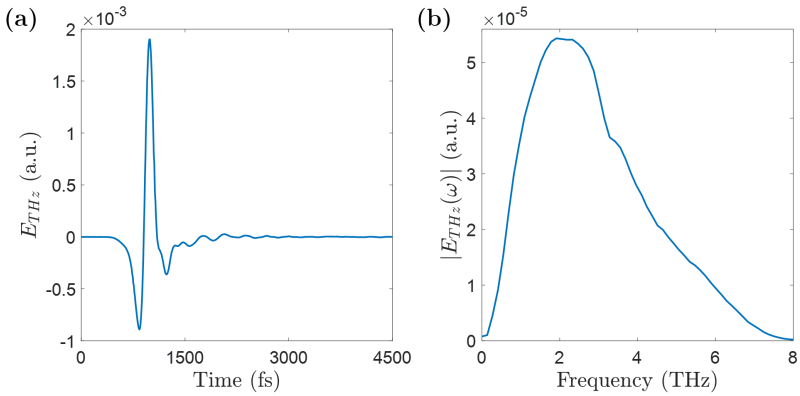


Figure 2.8: *Time-resolved electric field amplitude (a) and its corresponding spectrum (b) using 100 µm-thick GaP electro-optic crystal.*

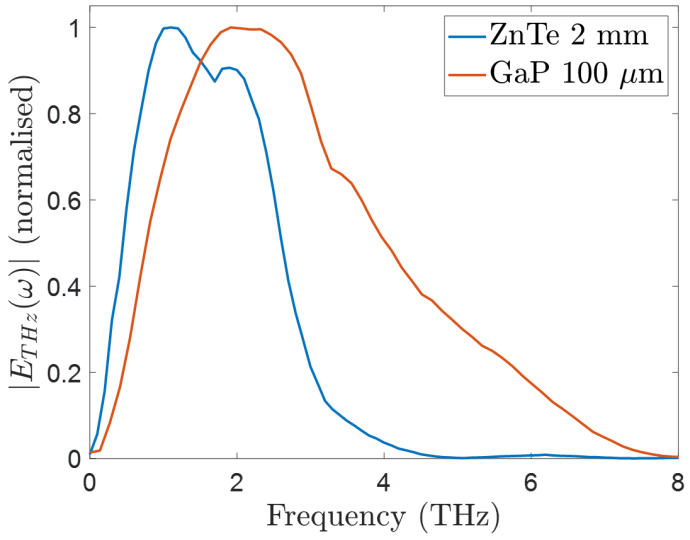


Figure 2.9: *Comparison between normalised amplitude spectrum obtained using two different electro-optic crystals for THz detection.*

due to the extended time of the e-beam technological step to reach $S_{tot} \sim 1\ mm^2$. However, for such typical dimensions of $< 1\ mm^2$, it is still crucial to strongly focus the THz beam at the sample position. Thus, focusing the THz beam down to the diffraction limit would be ideal. But, it is not trivial for a broadband THz pulses, essentially because photoconductive antennas are commonly excited by femtosecond optical pulses with plane-wavefront as either a low-divergent optical excitation beam is used or the THz emitter is placed close to the beam waist of a divergent optical excitation beam. The wavefront of the THz radiation at the surface of the photoconductive antenna is imposed by the plane wavefront of the optical pump beam. Therefore, the THz radiation behaves as a paraxial Gaussian beam with a beam waist located at the surface of the emitter and with a radius $w_{THz}$ that is constant for all frequencies. Moreover, the emitted THz electric field strongly diverges following the frequency-dependent relation $\theta = \sqrt{2}\frac{(\lambda_{THz}}{(\pi w_{THz}))}$. Consequently, the focusing parabolic mirror produces at its focal point (where the sample of interest is placed) a virtual image of the THz emitter. Since typical dimension of THz emitter is large compared to THz wavelength, the spatial resolution of the broadband TDS system is poor. More quantitatively, at a frequency of 10 THz for instance, the focused spot area ∼64 times higher than the diffraction limit area. Moreover, such weak focusing of the THz beam on the electro-optic crystal limits the Pockels effect and thus the dynamic of the THz-TDS system.

Achieving diffraction-limited focusing of the THz beam requires to achieve a THz emission with frequency-independent divergence and wavefront over more than 5 octaves. An original approach have been developed recently by my research group (M. Baillergeau [63]). By optically exciting the photoconductive antenna with a spherical wavefront, a broadband THz radiation is emitted with a divergence and a wavefront independent of the frequency over the full spectral range. To implement this approach, the THz photoconductive antenna is placed away from the Rayleigh range of the optical beam, as schematically represented on Figure 2.10 (a), in order to fully illuminate the 500 $\mu m^2$ emitter area with an spherical wavefront excitation. In this original scheme, the emitted THz radiation resembles a paraxial Gaussian beam with a divergence of the THz electric field equals to the divergence of the optical beam, for all frequencies. Thus, the THz radiation behaves as a Gaussian beam with a beam waist virtually located before the position of the large-area photoonductive antenna. The emitted THz field with frequency independent divergence is then collected by a second parabolic mirror $PM_1$ that collects the whole emitted radiation. Finally, as shown in Figure 2.10 (b), a third parabolic mirror $PM_2$ identical to $PM_1$ and that is fully illuminated for all frequencies, focuses the THz beam. Thus, with this configuration, at the sample location the THz beam is focused in the diffraction limit. Note that this original concept is valid for frequencies that are higher than $\lambda_{THz} < 2\pi w_{THz} \sim 3THz$. For lower frequencies, THz radiation diffracts in all directions leading to a strong divergence, as expected by Bethe's theory of diffraction by small holes.

In our experimental set-up, we use a f-2 for focusing. In the diffraction limit, the THz beam waist $w_0$ (in the air) at the focal point of the parabolic mirror $PM_2$ can be approximated by $w_0 \sim \frac{1.22}{2}\lambda N$ with $N$ the $PM_2$ f-number. The beam spot diameter at the focal point and the Rayleigh range for all frequencies are computed on Figure 2.11.

One may consider to reduce the waist by replacing $PM_2$ mirror by a f-1 or f-0.8 that are standard parabolic mirrors and commercially available. However, for low temperature transmission measurements, the sample is put in a cryostat with (low THz absorption) back and front windows. Increasing the numerical aperture of the $PM_2$ mirror would lead to significant geometrical constraints as it needs larger windows and it limits the space between $PM_2$ and $PM_3$ to insert the cryostat.

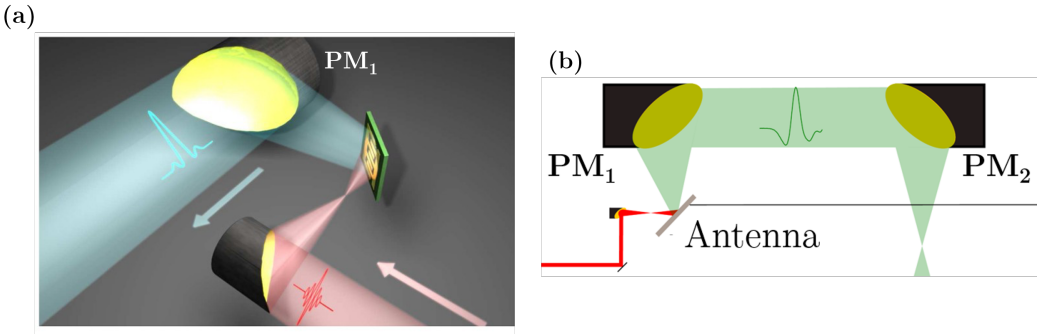


Figure 2.10: *(a) Sketch of the photoconductive antenna excited by a spherical wavefront. It is placed away from the Rayleigh range of the optical beam (red). The divergence of the THz beam (blue) and the optical beam are equals. (b) The THz beam is focused on a sample by a parabolic mirror $PM_2$ identical to $PM_1$.*

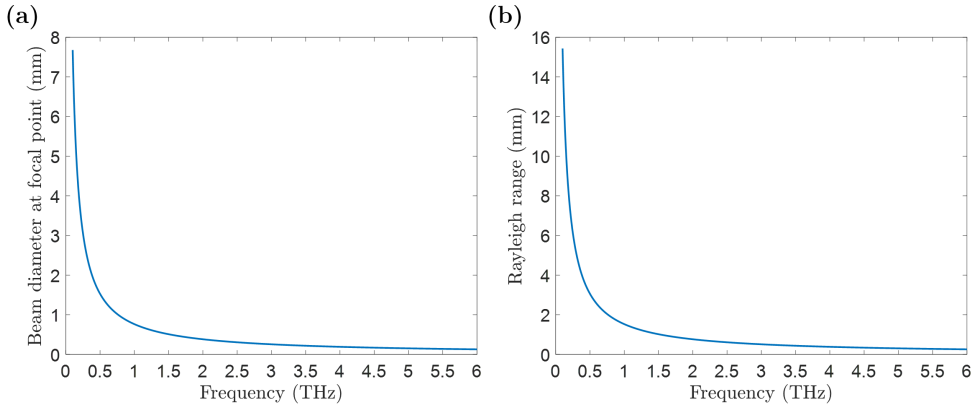


Figure 2.11: *Beam spot diameter at the focal point (a) and Rayleigh range (b) as function of the frequency, computed with respect to the experimental set-up configuration.*

### 2.1.3 Transmission measurement of a sample by THz-TDS

In order to determine the complex refractive index of a graphene based material deposited on top of a thick substrate, two measurements are needed using THz-TDS system. A first acquisition of the THz electric field passing through the sample on its substrate $E_{sample}(t)$, and another one only through the substrate $E_{substrate}(t)$, which will be the reference. From these two acquisitions, the transmittance $t(\omega)$ of the graphene based material is extracted. Indeed, the transmittance is expressed by the ratio between the Fourier transform amplitudes of the aforementioned temporal acquisitions:

$$t(\omega) = \frac{E_{sample}(\omega)}{E_{substrate}(\omega)}$$

In the following section, we briefly describe the mathematical approach of deriving the complex conductivity of a graphene based material from the recorded amplitude transmittance. The graphene based material could be either graphene layers or arrays of GQD.

#### Tinkham formula

We first consider that the system we probe by an incident THz beam $E_{inc}(\omega)$ is composed by a film of thickness $d$ on a substrate of thickness $L$.
Figure 2.12 depicts the propagation of a linearly polarised THz pulse through a substrate (1) only (which will be the reference signal $E_{ref}(\omega)$), and the same THz pulse propagating through a film (2) on a substrate (1), of respective complex refractive index $n_j(\omega) = n_j + i.n_j(\omega)$ (with $j = 1, 2$), which will be the sample signal $E_{sample}(\omega)$. Both elements are surrounded by air (0) of refractive index $n_0 = 1$ and $E_{inc}(\omega)$ denotes the incident beam. In the following equations, we will write all the frequency-dependent quantities $a(\omega) \equiv \hat{a}$ for clarity.

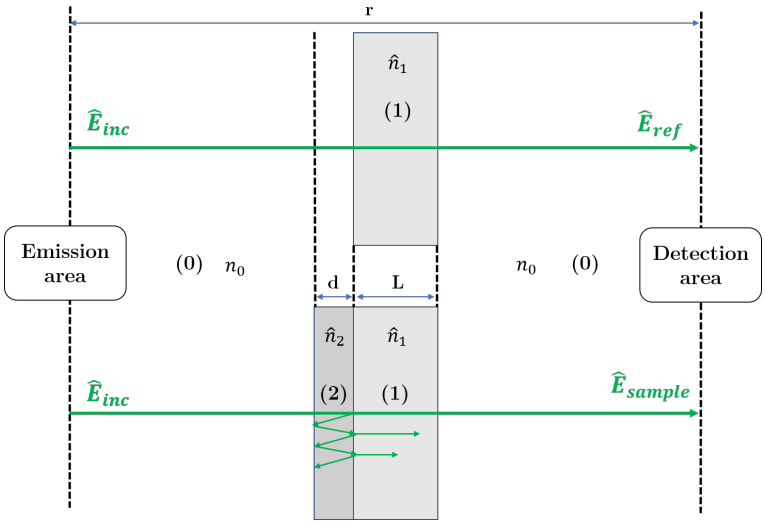


Figure 2.12: *Sketch of reference and sample signal propagation through a substrate and a film on a substrate, respectively. r denotes the geometrical distance between the emission and detection areas.*

According to notations used in Figure 2.12, the detected reference signal writes as:

$$\widehat{E}_{ref} = \widehat{E}_{inc} e^{i\omega(r-L)/c}\, \widehat{t}_{01}\, e^{i\widehat{n}_1\omega L/c}\, \widehat{t}_{10}\, FP_{010} \tag{2.3}$$

where $FP_{010}$ denote the Fabry-Perot term resulting from multiple reflections at the interface, given by:

$$FP_{010} = \left(1 + \widehat{r}_{01}\widehat{r}_{10} e^{2i\widehat{n}_1\omega d/c}\right)^{-1} \tag{2.4}$$

and $\widehat{t}_{01}$ and $\widehat{r}_{01}$ the usual Fresnel transmission and reflexion coefficients, given in the case of normal incidence on a plane boundary between two materials $i$ and $j$ by:

$$\widehat{t}_{ij} = \frac{2\widehat{n}_i}{\widehat{n}_j + \widehat{n}_i} \quad \text{and} \quad \widehat{r}_{ij} = \frac{\widehat{n}_j - \widehat{n}_i}{\widehat{n}_j + \widehat{n}_i} \tag{2.5}$$

The Fabry-Perrot term will play a role if the subsequent echoes are recorded in the temporal acquisition window of $E_{ref}(t)$. In the further study, the substrate (1) is thick enough that we can cut the appearance of the first echo by restricting the acquisition window. Consequently, we will consider that (2.4) equals to one. Additionally, the graphene-based materials presented in this study are grown on an insulating substrate, i.e. we can consider that $\widehat{n}_1 \approx n_1$, which simplify (2.7) to:

$$\widehat{E}_{ref} = \widehat{E}_{inc} e^{i\omega(r-L)/c}\ t_{01}\ e^{i\widehat{n}_1\omega L/c}\ t_{10} \tag{2.6}$$

The detected sample signal through the film (2) on a substrate (1) is:

$$\widehat{E}_{sample} = \widehat{E}_{inc} e^{i\omega(r-d-L)/c}\ \widehat{t}_{02}\ FP_{021}\ e^{i\widehat{n}_2\omega d/c}\ \widehat{t}_{21}\ e^{in_1\omega L/c}\ t_{10} \tag{2.7}$$

By replacing the Fresnel coefficients in the expression of $\widehat{E}_{ref}$ and $\widehat{E}_{sample}$ using (2.5) and the Fabry-Perrot term in $\widehat{E}_{sample}$ using expression (2.4), the transmittance writes:

$$\widehat{t} = \frac{\widehat{E}_{sample}}{\widehat{E}_{ref}} = \frac{\widehat{n}_2(1+n_1)e^{-i\omega d/c}}{\widehat{n}_2(1+n_1)\cos(\widehat{n}_2\omega d/c) - i(\widehat{n}_2^2+n_1)\sin(\widehat{n}_2\omega d/c)} \tag{2.8}$$

We now apply the thin film approximation, that is the graphene-based material thickness $d$ on the substrate surface is much smaller than the incident THz wavelength $d \ll \lambda_{THz}$:

$$\widehat{t} \simeq \frac{(1+n_1)}{1+n_1 - i(\widehat{n}_2^2+n_1)\omega d/c} \tag{2.9}$$

We can furthermore simplify the above expression as the thin layer is much more conductive than the substrate ($\widehat{n}_2^2 \gg n_1$ and rewrite (2.9) in terms of the complex conductivity of the graphene-based material using $\widehat{n}_2^2\omega/c = iZ_0\widehat{\sigma}$:

$$\widehat{t} = \frac{(1+n_1)}{1+n_1+Z_0\widehat{\sigma}d} \tag{2.10}$$

with $Z_0 = 1/(\epsilon_0 c)$ the free-space impedance.
Going to the limit of an infinitely thin film ($d \to 0$), defining a two-dimensional conductivity $\widehat{\sigma}_{2D} = \lim_{d\to 0}\widehat{\sigma}d$. We can rewrite the amplitude transmittance:

$$\widehat{t} = \frac{(1+n_1)}{1+n_1+Z_0\widehat{\sigma}_{2D}} \tag{2.11}$$

For our ensemble of weakly absorbing GQDs, one may retain only the real part of the conductivity $\widehat{\sigma}_{2D} \simeq \pi\widehat{\alpha}/Z_0$ expressed as function of the aborption probability $\widehat{\alpha}$ and get finally:

$$\widehat{t} = \frac{(1+n_1)}{1+n_1+\pi\widehat{\alpha}} \tag{2.12}$$

**Frequency resolution**

The frequency resolution of the extracted complex conductivity is limited by the frequency resolution of the transmittance measurements. The frequency resolution of the measurement is fixed by the temporal acquisition window. However, the time window extension is limited by the appearance in the signal of echoes from the main THz pulse due to internal reflections within the photoconductive antenna and the sample substrate. Including echoes in the temporal acquisition would lead to aliasing in the spectrum and thus in the calculated transmittance. Some techniques have been developed to get rid of this limitation [64] but it requires longer acquisitions and a basic knowledge of the physical properties, such as the complex index of refraction, of the probed material. As it is precisely these quantities we want to investigate, we set a maximal time windowing for the acquisition at the appearance of the first echo. The delay between the main THz pulse and the first echo from the photoconductive antenna is set by the 500 $\mu m$ thickness of of the GaAs substrate of the photoconductive antenna. To push away the echo from the photoconductive antenna, I have carefully sticked under it another 500 $\mu m$ thick semi-insulating GaAs substrate, using Poly(methyl methacrylate) (PMMA) glue, leading to a total thickness of 1 $mm$ and thus doubling the delay between the main THz pulse and the first echo, with an extremely small residual echo at the interface (see Figure 2.13 (a)). This configuration enables high frequency resolution acquisitions of 0.04 THz (see Figure 2.13 (b)).

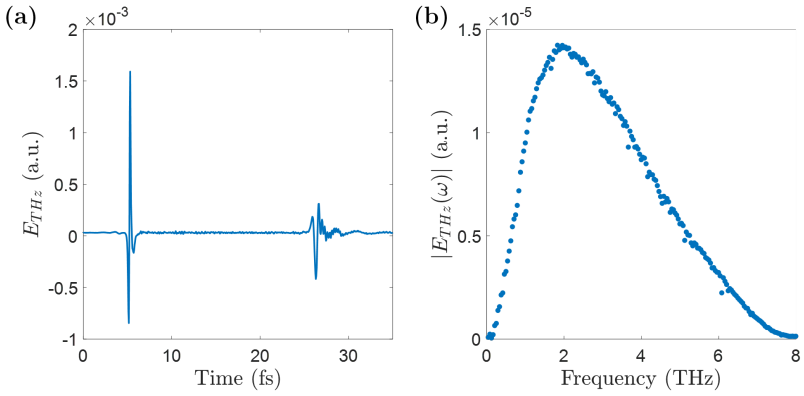


Figure 2.13: *(a) Time-resolved electric field amplitude for 1 mm-thick photoconductive antenna. (b) THz spectrum obtained from time-resolved measurement with a 1 mm-thick antenna.*

The investigated graphene-based materials are grown on a Silicon Carbide (SiC) substrate of thickness approximately 300 $\mu m$. To increase the delay between the main THz pulse and the first echo from the SiC substrate, I made several attempts to stick another SiC substrate, but unfortunately, SiC has less affinity to PMMA than GaAs substrate and the attempts were unsuccessful. Consequently, its the echo within the SiC substrate that sets the temporal acquisition window to approximately 10 ps, and thus the frequency resolution of our measurements is limited to 0.124 THz.

## 2.2 THz TDS characterisation of multilayer epitaxial graphene

We first investigate the THz conductivity of multilayer epitaxial graphene grown on C-terminated surface of 4H-SiC substrate, using THz time domain spectroscopy. There are several motivations to this study. First, the array of GQDs will be processed from this epitaxial stacking of graphene layers. Understanding the THz properties of the graphene layers before processing the GQDs is therefore essential. We choose multilayer epitaxial graphene,

grown by the group of C. Berger and W. A. de Heer, and produced by thermal desorption of Si from the C-terminated face of single-crystal 4H-SiC(000-1) since it yields a high quality multilayer graphene at the wafer scale on flat and non-interacting substrate [65], [10]. Multilayer epitaxial graphene is known to contain few highly-doped layers near the substrate interface and, on top, typically a few tens of independent layers with non-Bernal rotated graphene planes. Indeed, it has been shown that, owing to the layer rotational stacking, multilayer epitaxial graphene is composed by $N_l$ independent layers of graphene that possess the electronic properties of a single graphene layer [66], [67]. The chemical potentials of the heavily-doped layers $\mu$, obtained from magneto-spectroscopy measurements, are 360, 275, 130 and 80 meV above the Dirac point and the chemical potential of the quasi-neutral layers is below $\mu_{max}$=7 meV above their Dirac point [68], [69]. The second motivation to this work is to elucidate how close the Fermi level is to the Dirac point in the quasi-neutral layers. Finally, this study aims at demonstrating the possibility to achieve interband conductivity at THz frequencies in these quasi-neutral layers.

For this purpose, we measure the transmitted THz waveforms through the multilayer graphene sample and through a bare SiC substrate from 5 K to 300 K as illustrated in Figure 2.14a. Using Fourier transformation, the amplitude transmittance spectra $t$ in the frequency domain from 0.4 THz to 4 THz are obtained. Figure 2.14b shows the transmittance as a function of the temperature for different frequencies. We clearly observe that the overall transmittance and thus the total conductivity of the multilayer graphene strongly varies with temperature for all frequencies.

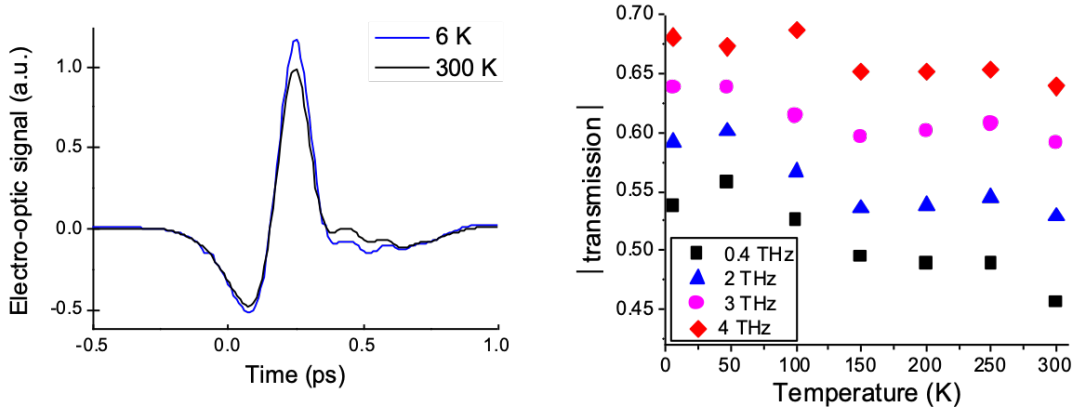


Figure 2.14: *a) Transmitted THz electric field through the graphene sample at 5 K (blue) and 300 K (black). Insert: corresponding amplitude spectrum of the THz electric field at T=300 K obtained by fast Fourier transform. b) Transmittance as a function of the temperature for different frequencies.*

These changes are due to the temperature-dependent conductivity of the quasi-neutral layers only. Indeed, the conductivity of the highly-doped layers, for which $\hbar\omega \ll \mu$, is governed by intraband transition processes that are well described by a Drude model [70]. Using this Drude model, the intraband transition processes in the highly-doped layers $k_BT < \mu < 1$ are predicted to be independent of the temperature from 5 K to 300 K, as shown in Figure 2.15a. Thus, the temperature dependence of the transmittance observed in Figure 2.14b results from the intraband and the interband conductivities of the quasi-neutral layers. Figure 2.15b (upper panel) focuses on the amplitude transmittance spectrum $|t|$ of the multilayer graphene at 5 K. The transmittance is nearly constant up to 1 THz and then increases

monotonously. However, in graphene at low temperature, intraband (Drude) conductivity shows monotonic frequency dependence whereas interband conductivity provides a sharp response around $2\mu$. Thus, a negative slope extending over more than 1 THz due to thermal smearing of the $2\mu$ feature is expected as illustrated in Figure 2.15b(bottom panel), which reports the calculated transmittance at 5 K of a multilayer graphene sample consisting of the four doped layers and $N_l$=53 quasi-neutral layers of chemical potential $E_F$=7 meV using our model described below. It is surprising that such a slope change is not observed in the measured transmission spectra as the build-up of the interband conductivity of the quasi-neutral layers is expected at $\hbar\omega < 2\mu_{max}$=14 meV i.e. $f<$ 3.5 THz.

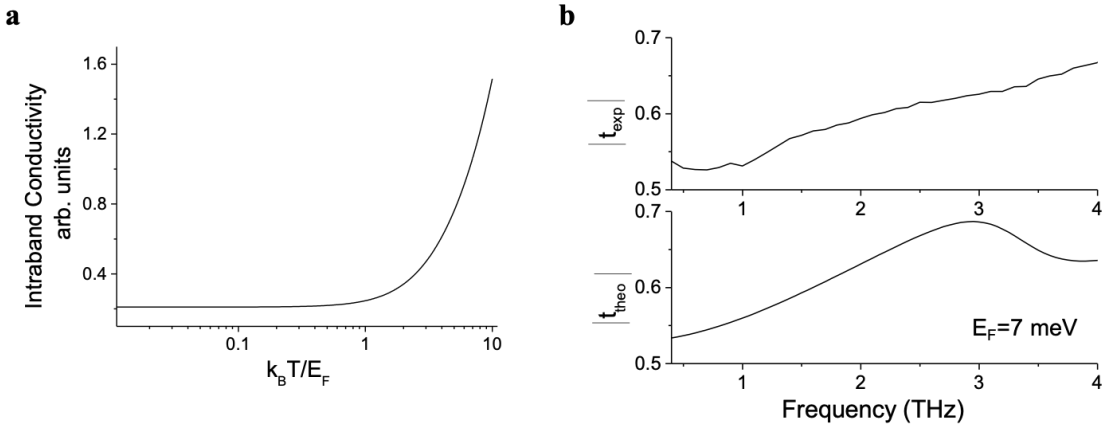


Figure 2.15: *a) Calculation of the intraband conductivity in graphene as a function of $k_BT/E_F$ [16]. b) Amplitude transmittance spectrum $|t|$ of the graphene multilayers at 5 K measured (top) and predicted (bottom) for $\mu$=7meV.*

This behavior could not be explained by a broadening of the chemical potential in the quasi-neutral layers leading to a smooth interband response as the narrow width for the magneto-transmission line (involving Landau levels $L_{1(0)}$ and $L_{0(1)}$ respectively in the valence and conduction bands) measured over a large area in multilayer epitaxial graphene samples by magneto-spectroscopy demonstrates the weak chemical potential fluctuations in the quasi-neutral layers. In contrast, we can attribute this behavior to a chemical potential of the quasi-neutral layers lower than the investigated spectral range, i.e. $\mu \leq 1$ meV. This assumption is supported by the change of the experimental transmission spectra as soon as the temperature is increased from its lowest value ($k_BT = 1$ meV at T=11 K) considering that interband and intraband processes in graphene vary with temperature only for $\mu \leq k_BT$.

For a more thorough understanding of the interplay between interband and intraband processes in the quasi-neutral graphene layers, we perform a full calculation of the temperature-dependent THz conductivity in the highly-doped and the quasi-neutral graphene layers. As described previously, the transmitted electric field through the graphene sample normalized to the transmitted electric field through the substrate is related to the total conductivity of the graphene layers by the Thinkam formula:

$$t(\omega) = \frac{1 + n_{SiC}}{1 + n_{SiC} + Z_0\sigma(\omega)} \tag{2.13}$$

where $n_{SiC}$ is the refractive index of the SiC substrate and $\sigma(\omega)$ is the complex total conductivity of the graphene layers. The total conductivity includes the contribution of the four highly-doped layers $\sigma_{doped}(\omega)$ and of the N quasi-neutral layers $\sigma_{QN}(\omega)$ and is given

by $\sigma(\omega) = \sigma_{doped}(\omega) + N_l\sigma_{QN}(\omega)$. $\sigma_{doped}(\omega)$ relies on intraband processes only, as discussed earlier, and is calculated using a scattering time of 70 fs in agreement with a previous report [71]. The intraband and interband processes in the quasi-neutral layers compete at THz frequencies and thus: $\sigma_{QN}(\omega) = \sigma_{QN\_intra}(\omega) + N_l\sigma_{QN\_inter}(\omega)$. For the intraband conductivity, the thermal broadening of the electron distribution must be taken into account since its magnitude is of the same order as the chemical potential. Thus, we describe the frequency-dependent intraband conductivity of the thermalized electron gas in the quasi-neutral graphene layer using:

$$\sigma_{QN\_intra}(\omega) = -\frac{e^2}{v_F^2}\int_{-\infty}^{+\infty} D(E)\frac{\tau(E)}{1 - i\omega\tau(E)}\frac{\partial f_{FD}(\mu, T, E)}{\partial E}\,\mathrm{d}E \tag{2.14}$$

where $D(E) = \frac{2}{\pi\hbar^2 v_F^2}|E|$ is the energy-dependent density of states in graphene, $\tau(E)$ is the electron momentum scattering time, $v_F$ is the Fermi velocity and $f_{FD}$ the Fermi Dirac distribution. $\mu(T)$ is the chemical potential that is a decreasing function of the temperature, calculated considering the conservation of the total particle number in the system. The interband conductivity of one quasi-neutral graphene layer is given by:

$$\sigma_{QN\_inter}(\omega) = \frac{\pi e^2}{4h}\left[\tanh\left(\frac{\hbar\omega + 2\mu(T)}{4k_BT}\right) + \tanh\left(\frac{\hbar\omega - 2\mu(T)}{4k_BT}\right)\right] \tag{2.15}$$

Previous studies on multilayer epitaxial graphene have shown that the scattering time in the quasi-neutral layers is inversely proportional to the carrier energy and is dominated by short-range scattering on residual intrinsic defects over a very broad energy range from 10 meV to 1.5 eV [72], [73]. Long-range scattering on Coulomb impurities in the quasi-neutral layers can be neglected since the layers inside the stack are naturally protected and screened from the environment; the thermal decomposition growth process directly from the SiC substrate prevents contamination by extrinsic impurities. We do not consider in the model scattering mechanisms due to absorption of optical phonons since the thermal energy in this study remains considerably lower than the optical phonon energy in graphene (200 meV). Finally, contributions due to interactions with acoustic phonons as well as carrier-carrier scattering are usually considered to be relatively small for low energy carriers [74].

Figure 2.16a shows the transmission spectra measured at 5 K, 50 K, 100 K, 200 K and 300 K from 0.4 to 4 THz. It is observed that, from 5 K to 50 K, the transmission (absorption) slightly increases (decreases) over the entire spectral range and above 50 K the absorption of the graphene layers increases as the temperature is increased. Below 1 THz, the transmission spectra are virtually flat except at a temperature of 300 K. Above 1 THz, the spectra show a monotonic behavior with the frequency. We also observe that the spectra at 4K, 50 K and 100 K overlap around 3.7 THz. In Figure 2.16b, the transmission spectra calculated using our model for $\mu$=0 meV are reported and in Fig. 2.16c the deviation from the calculated to experimental data expressed by $\Delta t = |t_{exp}| - |t_{theo}|$ is shown. The dashed lines in Figure 2.16b and the black symbols in Fig. 2.16c are the calculated data considering carrier scattering on short-range potentials with a momentum scattering time given by $\tau_{SR} = \alpha/|E|$, where $\alpha$ is a constant-temperature independent fit parameter ($\alpha$=1 fs/eV and $N_l$=53 layers have been used in the calculations). The model generally reproduces the measured data from 1.5 THz to 4 THz, indicating the main role played by scattering on short-range potentials in agreement with previous reports. However, a strong discrepancy between the predicted and measured transmission is observed at low frequency (below 1.5 THz). Thus, our results reveal that an additional scattering mechanism is involved at energies close to the Dirac point. As is known, vacancies in graphene give rise to bound states at the Dirac point, the so-called midgap states [75]. Scattering by such defects may also be involved in the low-frequency

intraband conductivity of the quasi-neutral layers. To incorporate their contribution in the model, we include the scattering time given by $\tau_{MD} = \beta|E|(ln\gamma E)^2$ with $\gamma$ related to the radius of vacancies and $\beta$ is a constant-temperature independent fit parameter [76]. The total momentum scattering rate is thus given by $\Gamma = (\alpha/|E| + \beta|E|(ln\gamma E)^2)^{-1}$. The solid lines in Figure 2.16b show the transmission spectra calculated for $\alpha$=1 fs/eV, $\beta$=20 ps/eV and $\gamma$=0.1. One can see that our model based on scattering on both short-range potentials and on midgap states agree well with the experimental data for $E_F$=0 meV. In particular it reproduces the decrease of the transmission with increasing temperature, the monotonic frequency dependence above 1 THz, the plateau at lower frequencies and also the overlap of the spectra at 4K, 50 K and 100 K around 3.7 THz. We estimate that our accuracy on the Fermi level is 1 meV (i.e. $2E_F$= 2meV) owing to the low cut-off frequency of the THz time domain spectroscopy experiment. These results strengthen our assumption on the position of the Fermi level in the quasi-neutral layers since midgap-states can pin the Fermi level at the Dirac point [77] (see Figure 2.16d). Our study provide a unique insight in scattering mechanisms involved at energies close to the Dirac point. They result from the interplay between scattering on short-range potentials and on channels via midgap states related to the presence of vacancy defects.

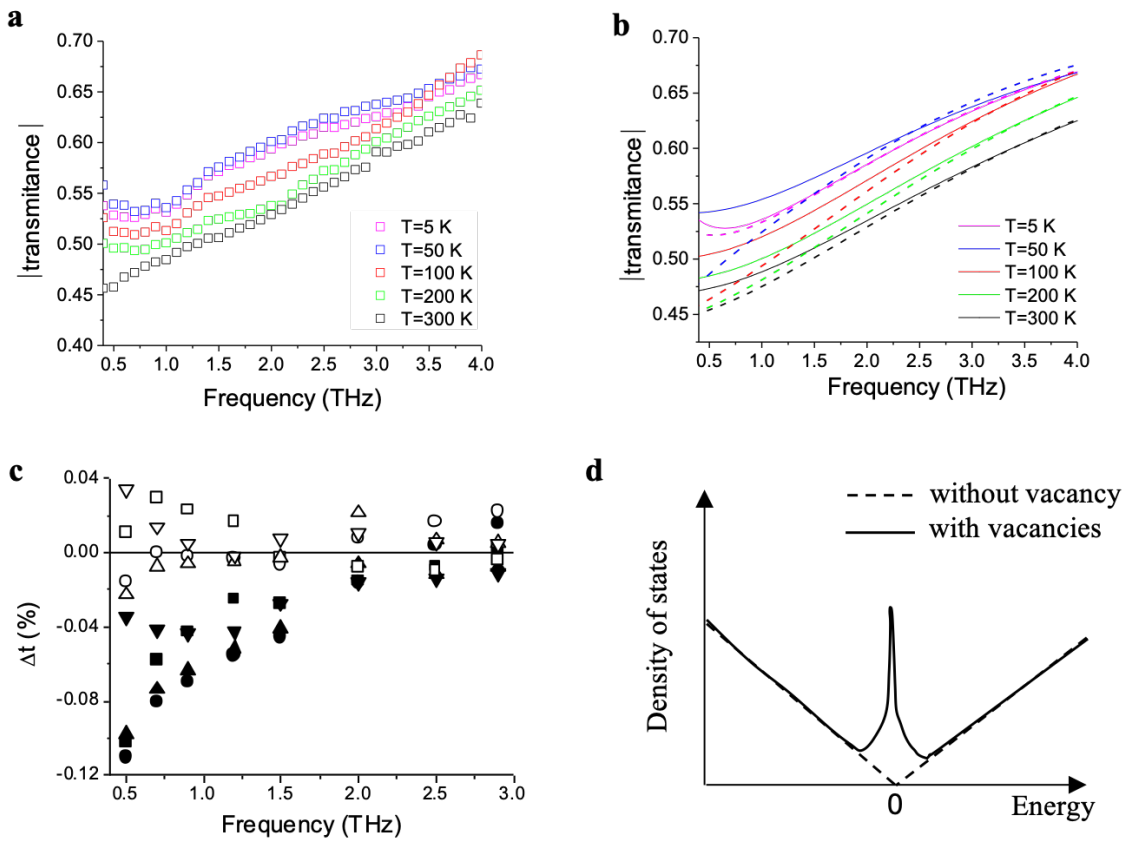


Figure 2.16: *a) Experimental transmission spectra of MEG at 5K, 50 K, 100 K, 200 K and 300 K. The error bars are the standard deviation in the measurements. b) Corresponding calculated transmission spectra of graphene layers considering scattering on short-range potentials only (dashed line) and considering both scattering on short-range potentials and on mid-gap states (solid line). c) Deviation in % from calculated to experimental data* $\Delta t = |t_{exp}| - |t_{theo}|$ *as a function of frequency. Black symbols results from calculations assuming scattering on short-range potentials only and open symbols on both scattering processes. d) Schematic of the density of states of graphene without and with vacancies.*

A further interesting aspect of our study in temperature is the identification of the distinct conductivities in the highly-doped layers and in the quasi-neutral layers. Figure 2.17a shows the predicted intraband conductivity of the quasi-neutral layers for $E_F$=0 meV and of the highly-doped layers at 5 K and 300 K. The intraband conductivity of the highly-doped layers is constant from 5 K to 300 K as expected and dominates the total intraband conductivity of multilayer epitaxial graphene at low temperature. Conversely at 300 K, the contribution of intraband conductivity from quasi-neutral layers is strongly increased from 5 K to 300 K owing to the thermal distribution of electron. The interband conductivity of the quasi-neutral layers, shown in Figure 2.17b, follows the standard evolution of thermal electronic distribution. Our analysis demonstrates interband transitions in multilayer expitaxial graphene at THz frequencies. This opens the route to the development of graphene-based devices for THz photonic applications such as THz lasers and THz saturable absorbers.

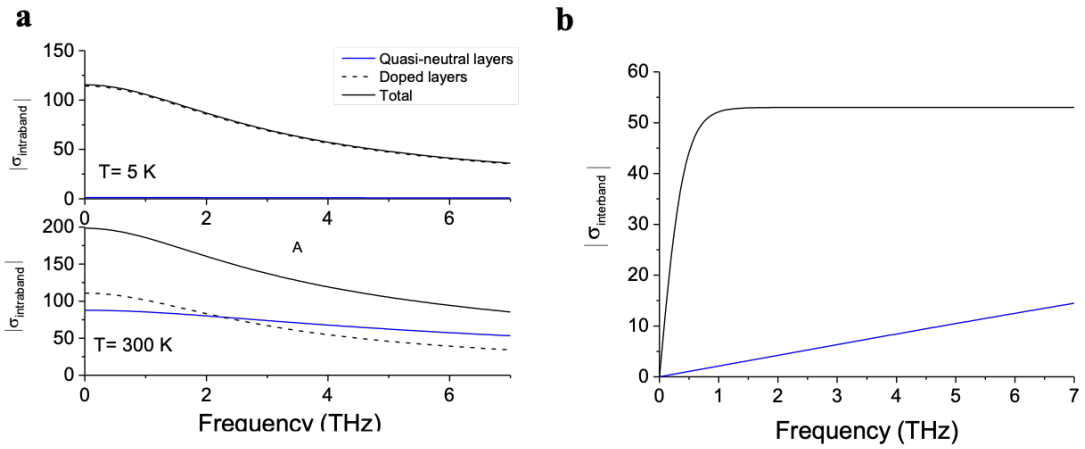


Figure 2.17: *a) The predicted intraband conductivity of the quasi-neutral layers for $E_F$=0, of the highly-doped layers and the total intraband conductivity at 5K and 300 K. b) The interband conductivity of the quasi-neutral layers at 5K (blue line) and 300 K (black line).*

**Section conclusion**

From this study of the THz conductivity of multilayer epitaxial graphene, we show that the properties of the quasi-neutral layers are well described by a Fermi level pinned at the Dirac point by mid-gap states [77]. We highlight that the dominant scattering mechanisms are a result of intrinsic defects that induce scatterings on short-range potentials and mid-gap states. These findings show the existence of interband processes at THz frequencies in multilayer epitaxial graphene. Furthermore, this work highlights the potential of THz-TDS technique for investigating the THz properties of graphene based materials without the need of contact that is very promising for probing the THz response of arrays of GQDs.

## 2.3 Probing THz absorption of GQD using THz-TDS

In this section, we evaluate the possibility to probe the absorption of GQDs in the THz spectral range using our THz-TDS experiment. We have shown in the previous chapter that reducing the spatial extension of a graphene sheet down to few tens of nanometer-sized circular GQD structures lead to the full discretization of its electronic states. From the determination of the absorption probability $\alpha(\omega)$ of a monolayer GQD, we have demonstrated that such GQDs can couple efficiently to photons of meV energy and thus lead to pronounced

absorption in the THz spectral range. In the theoretical determination of the absorption probability $\alpha(\omega)$ of a GQD, we have considered an optical power $W_{inc}(\omega)$ fully incident onto a quantum dot of area $S = \pi R^2$, with $R$ the radius of the quantum dot. In practice, this is not feasible due to the large THz beam size (even at the diffraction limit) compared to the dimension of a single GQD. To overcome this issue, we decide to fabricate and probe a $S_{tot} \sim 1\ mm^2$ array of GQDs, as depicted in Figure 2.18.

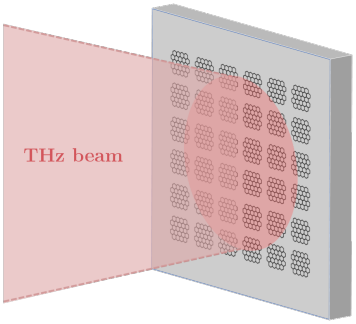


Figure 2.18: *Sketch of a GQDs array illuminated by a THz radiation. The GQDs array is designed to cover the entire THz beam.*

This assembly of GQDs is fabricated by nanostructuring the multilayer epitaxial graphene studied in the previous section, using electron beam lithography. Owing to the large number of graphene layers, the total absorption probability of such an array of multilayer epitaxial graphene quantum dots can thus be expressed as:

$$\alpha_{tot}(\omega) \approx \eta N_l \alpha(\omega) \tag{2.16}$$

with $\eta = S_{GQDs}/S_{tot}$ the ratio of remaining graphene area $S_{GQDs}$ nanostructed in GQDs over the total array surface $S_{tot}$.

At first, it is worth considering about the expected amplitude of the GQDs array transmittance. The experimental amplitude transmittance $t$ can be directly related to $\alpha_{tot}$ using the Tinkham formula. In the previous chapter, we have shown that the energy level distribution of a GQD, as well as which wavefunctions can couple efficiently to THz light, are fixed by its typical dimensions. Temperature and doping level are experimental parameters that enable to tune the absorption probability spectrum. Remarkably, a large "pristine" GQD ($E_F$=0 meV at T=0 K) possesses a graphene-like absorption spectrum, i.e. an optical response characterised by an interband absorption of $\alpha_0 = e^2/4\pi\epsilon_0\hbar c = 2.3\%$, independently from its dimensions (see previous Chapter). In this way, as a fist approximation, we roughly estimate the expected amplitude transmittance assuming $\alpha_0$ to be the absorption probability of all GQDs. Thus, the amplitude transmittance is expressed as:

$$t(\eta, N_l) = \frac{1 + n_{SiC}}{1 + n_{SiC} + \eta N_l \pi \alpha_0} \tag{2.17}$$

where $n_{SiC} \sim 3.25$ is the refractive index of the SiC substrate. Figure 2.19 shows the expected transmittance $t(\omega)$ as function $N_l$ for different values of $\eta$.

Considering that the sensitivity of our THz-TDS system is $\sim 2\%$ (dark dashed line), our prediction shows that whatever the GQD density $\eta$, the absorption of a GQDs array composed by a graphene monolayer would be too weak to be detectable. Moreover, if the filling factor is too small $\eta \leq 0.1$, even with a high number of graphene layers, the transmittance hardly reaches $\sim 2\%$. It is thus necessary to maximise both parameters $(\eta, N_l)$. This coarse

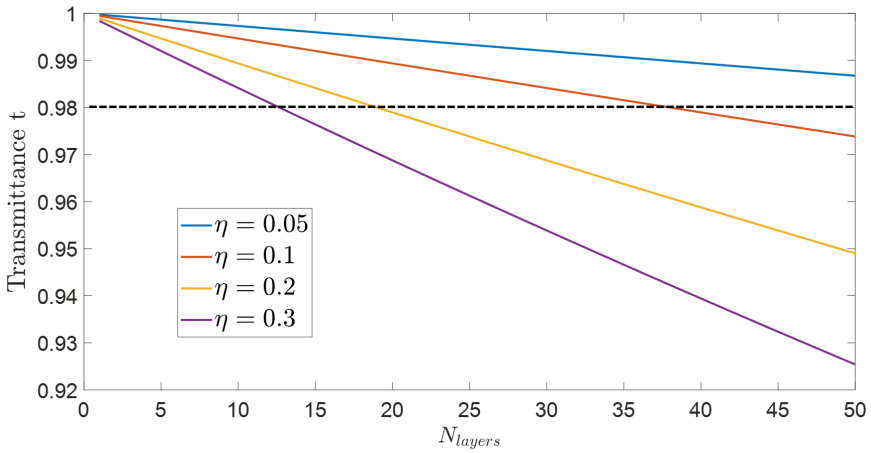


Figure 2.19: *Estimation of the GQDs array transmittance t as function the number of graphene layers $N_l$, for different values of the filling factor $\eta$.*

evaluation highlights that some technological and instrumental challenges need to be overcome to get a measurable transmittance for an array of GQDs.

The first critical step toward our goal is the nanofabrication of GQDs arrays. To fabricate a 1 $mm^2$ array with GQDs of diameter $\sim$ 70 $nm$, the distance between neighbouring GQDs has to be minimized down to few tens of nm in order to maximize the GQDs density $\eta$. A simple geometrical estimation shows that $\eta$ can hardly be increased beyond 30%, in order to avoid dots merging during the fabrication process. In addition, the total number of dots that need to be patterned on the multilayer graphene sample is estimated to be about $\sim 10^7$. Consequently, patterning $\sim 10^7$ nm-sized quantum dots over a surface of 1 $mm^2$ requires to elaborate significant technological developments.

The second challenge consists in probing the optical properties of GQDs arrays using broadband THz-TDS system. Indeed, as these samples associate small dimensions and weak absorption of the incident THz light, our initial THz-TDS system requires some critical improvements. In particular, it is crucial to strongly focus the THz beam at the sample position and improve the signal-to-noise ratio and stability of the THz-TDS set-up.

## 2.4 Fabrication of graphene quantum dot array

In this section, we describe the fabrication procedure of arrays of GQDs: we develop on a top-down approach, which mainly consists in nanopatterning the multilayer epitaxial graphene using electron-beam lithography (EBL) followed by reactive ion etching (RIE). As this new fabrication procedure of large GQDs was not mastered, it has needed several improvements that have result in three generations of fabricated samples: A, B and C. A generation is defined by the method used to nanofabricate a batch of GQDs. Based on the quality of the produced samples, together with their THz-TDS characterisation, the process was improved, leading to the next generation. I participated to the fabrication of the GQD samples, which has been driven by Elisa Riccardi, post-doc in my research group.

### 2.4.1 First generation: batch A

We start using 100 nm thick positive Poly(methyl methacrylate) (PMMA) resist, spin coated on different multilayer epitaxial graphene samples. Using EBL, we pattern an assembly of 40 to 60 nm-diameter GQDs, separated by $\sim 100\ nm$ (center-to-center distance) on an area of $\sim 1\ mm^2$ (see Table 2.1).

| Sample name | A1 | A2 | A3 |
|---|---|---|---|
| Number of graphene layers | 8 | 30 | 50 |
| GQDs diameter (nm) | $40-60$ | 50 | 40 |

Table 2.1: *Number of graphene layers of the MEG used to nanofabricate the GQDs arrays of batch A, with the corresponding GQDs dimensions after processing.*

The usual procedure to pattern a nanometer-sized structure by EBL is to draw a discretized sketch of the pattern, with a resolution defined by the resist and by the electron beam parameters (exposure time, electron dose). Given the high number of dots we plan to pattern ($\sim 10^7$), we make use of a different approach to reduce the EBL steps and thus the procedure duration. Each GQD is patterned using the "dot mode" of the electron-beam writing system: the electron beam is focused on a few tens of nm area, thus defining a circular GQD at once. The main advantage of using PMMA is that we can adjust the GQD diameter only by controlling the electron dose sent on the resist. The total procedure duration can thus be reduced to $\sim 20$ hours. After the development, we perform a 30 nm thick Aluminium (Al) deposit ,which acts as a protecting mask during the etching step. The remaining PMMA resist is removed, and a Fluoroform/Dioxygene ($CHF_3/O_2$)-based plasma etching is performed, leaving only the GQD array pattern. A lift-off using caustic potash (KOH solution) enables to remove the Al mask. Figure 2.20 shows Samples A1, A2 and A3 after the lift-off step.

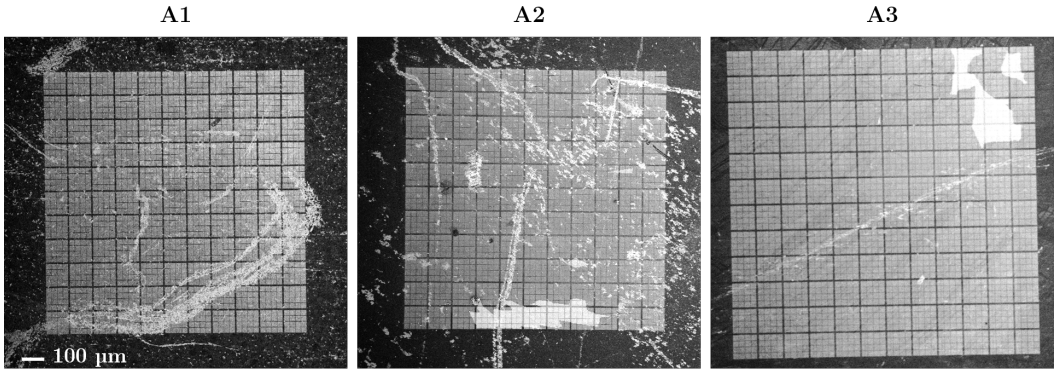


Figure 2.20: *Scanning electron microscopy (SEM) images of samples A1, A2 and A3 after nanoprocessing, at the same scale shown in A1 image. GQDs are patterned over* $25 \times 25\ \mu m$ *squared areas arranged in a* $4 \times 4$ *matrix, set as a unit cell. The GQD array is defined by a* $\sim 10 \times 10$ *matrix of this unit cell, resulting in a total area of about* $\sim 1\ mm^2$.

At large scale, the GQD arrays seem to present a relatively homogeneous pattern, with some aluminium residuals for samples A2 and A3. However, a closer observation shows significant defects in the structure. For sample A1 (Figure 2.21), we see $\mu$m scale dislocations and the GQDs shape is not well controlled.

For samples A2 and A3 (figure 2.22), the GQDs size distribution appear to be less dispersed, but the samples still exhibit some dislocations. Furthermore, we observe large metallic clusters, which we attribute to be residual aluminium aggregates. These Al clusters cannot be

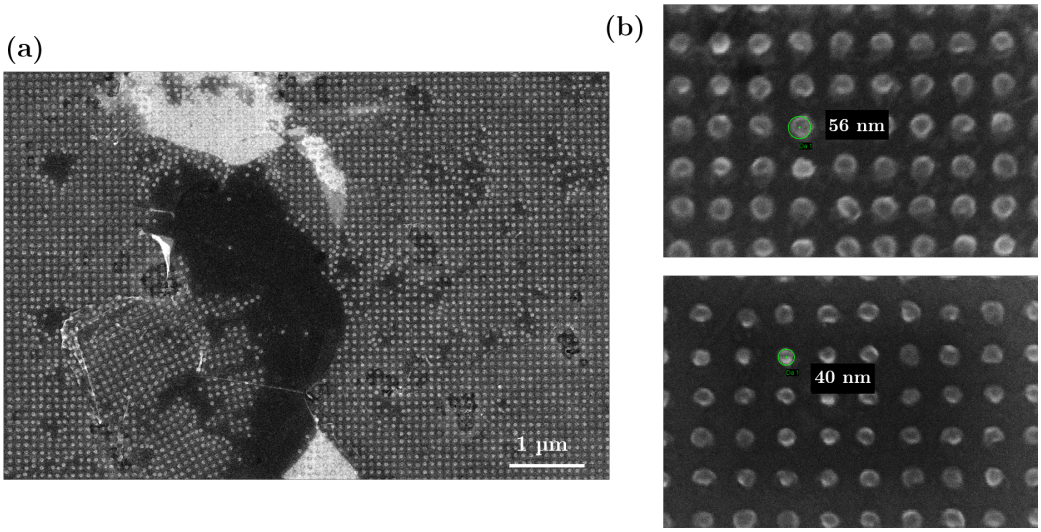


Figure 2.21: *SEM images of Sample A1. On a large scale (a), µm dislocations of the GQDs structure are visible. (b) Selected nm-scaled areas away from dislocations, showing a GQDs pronounced size and shape dispersion. The diameter of a GQD indicated by a green circle is given near the corresponding circle.*

completely removed by the lift-off step, even after several iterations. The THz-TDS measurements performed on the batch A (not shown in this work) were inconsistent with the expected orders of magnitude for the amplitude transmittance, due to the high-absorption of metallic impurities in the THz range.

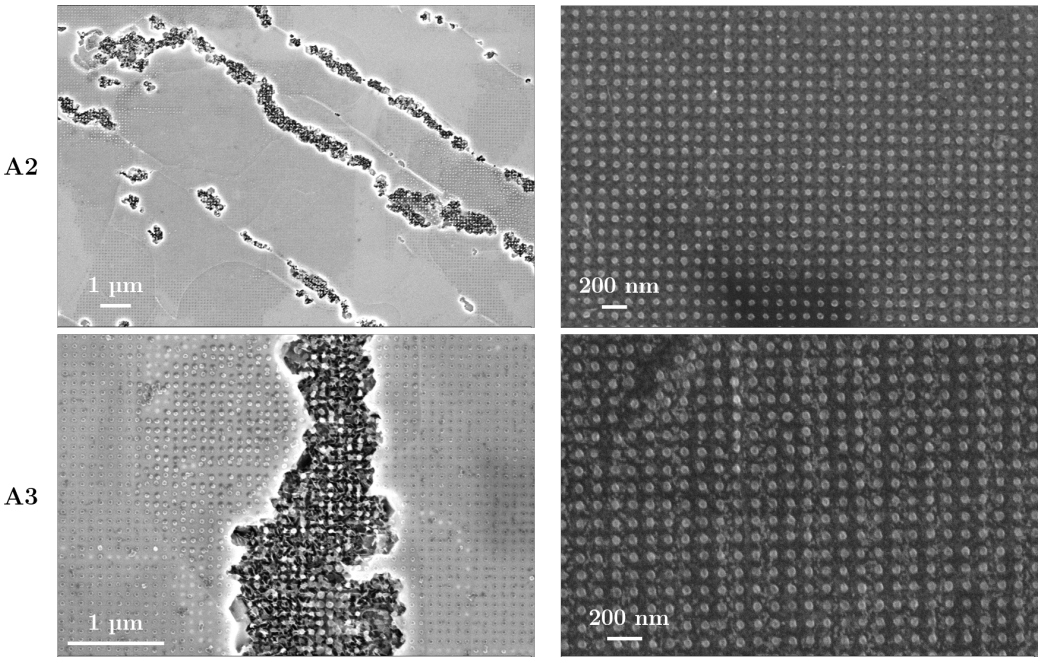


Figure 2.22: *SEM images of Sample A2 and A3 on large (left) and lower scale (right), on different areas. On the left images, we see aluminium aggregates over few µm on both samples. At lower scale, the GQDs size distribution appears to be less dispersed for Sample A2 (upper-right image) compared to A1, with few dots locally displaced. For sample A3, some residuals lie between dots, and several dots are locally displaced (bottom-right image).*

### 2.4.2 Second generation: batch B

As the Aluminium lift-off of such dense nanostructures always resulted in residual metallic impurities, we decide to avoid the use of a metallic protecting mask. We thus turn to a negative resist for the EBL patterning, which acts as a protecting layer during the etching step. For the fabrication of batch B (see Table 2.2), we spin-coated 100 nm of Hydrogen silsesquioxane (HSQ) negative resist on the multilayer epitaxial graphene, followed by a quick annealing. After EBL patterning and resist development, a RIE is performed, removing directly the unprotected heterostructure area.

However, the HSQ resist does not allow the same electron dose-tunability while patterning the GQD array using "dot mode". As the largest diameter that can be drown on the resist at once is about 30 nm, we change the fabrication protocol: each dot is patterned as the superposition of three close electron shots on the resist, as depicted in Figure 2.23. We set the GQDs diameter to be about 70 nm, the distance between the dots to be 110 nm to reach a filling ratio $\eta$ around 30 %. Consequently, the total EBL procedure require $\sim$ 60 hours.

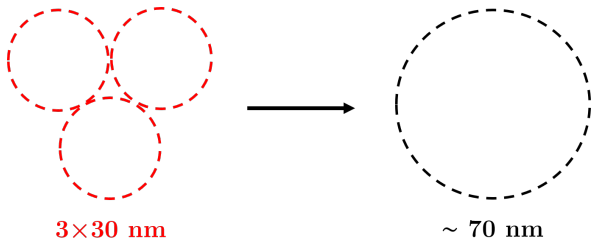


Figure 2.23: *Sketch of the method used to pattern large GQDs on HSQ resist. A single electron shot (red circle) allows to pattern at once a dot of diameter limited to 30 nm. The combination of three close electron shots however allows to cross-link the resist over a large quasi-circular area of $\sim$ 70 nm.*

| Sample name | B1 | B2 |
|---|---|---|
| Number of graphene layers | 20 | 20 |
| GQDs diameter (nm) | $60-70$ | 55 |

Table 2.2: *Number of graphene layers of the MEG used to nanofabricate the GQDs arrays of batch B, with the corresponding GQDs dimensions after processing.*

We observe on Figure 2.24 that this procedure results in a significant reduction of the presence of contaminants on the surface.

A closer look on the GQD arrays shows that the dot shape is much more circular compared the batch A and the diameter dispersion is improved. However, a non-negligible surface of the array still presents some deformations of the pattern: accidental removing of the resist or quantum dots merging as we can see on Figure 2.25. These inhomogeneities are observed on all fabricated samples of the batch B. Furthermore, the THz-TDS measurements on this GQD arrays batch do not show any detectable THz absorption, in contrast with our expectations. We interpret this observation as the consequence of a lowered filling ratio $\eta < 30$ %, due to a probably too high surface without dot patterning, as seen in Figure 2.25. Consequently, the technological procedure needs to be improved to enhance the adhesion of the resist on the full graphene sample area.

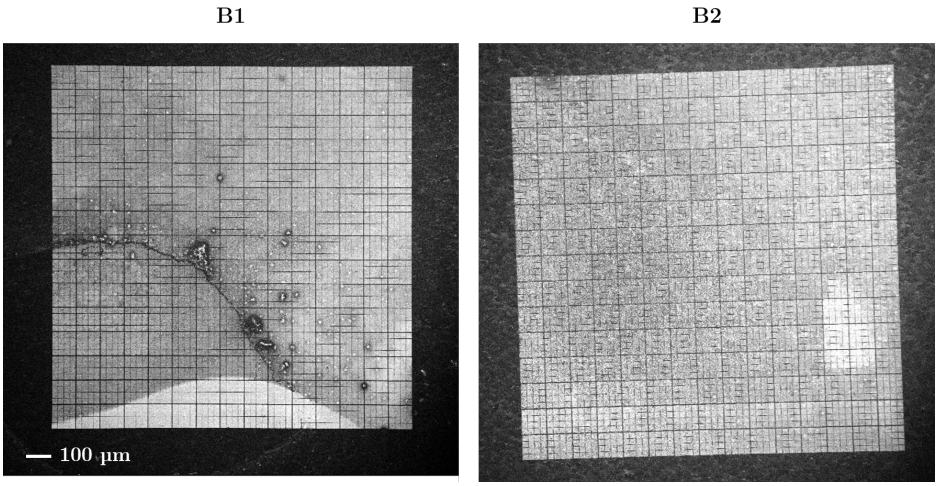


Figure 2.24: *SEM images of samples B1 and B2 after nanoprocessing, at the same scale indicated in B1 image. Despite some visible surface scratching in B1 (before processing), both samples B1 and B2 show no presence of residual contaminants on the surface.*

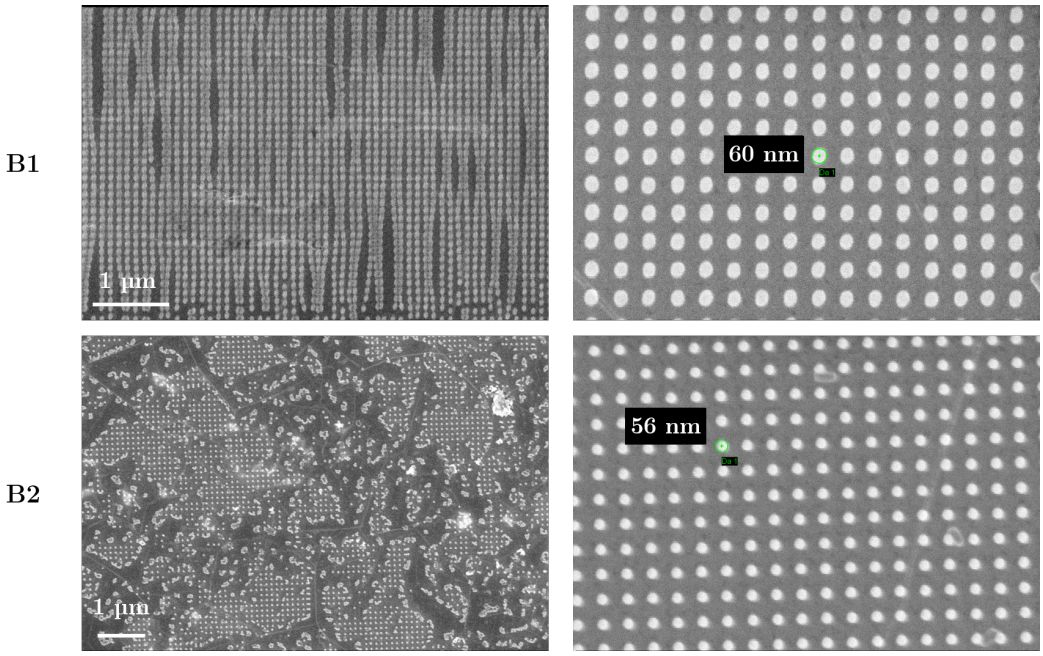


Figure 2.25: *SEM images of Sample B1 and B2 on large (left) and lower scale (right), on different areas. Left images emphasise the areas showing defects: dots merging for B1 and dislocations for B2. Right images shows that away from the defect areas, the HSQ resit allows to pattern homogeneous and quasi-circular GQDs, with a controlled diameter between 56 and 60 nm. The diameter of a GQD indicated by a green circle is given near the corresponding circle.*

### 2.4.3 Third generation: batch C

For the fabrication of batch C, with the aim of enhancing the adhesion of the resist on the graphene area, we spin-coat 30 nm of an adhesion promoter (Surpass 3000) and follow the same protocol as for batch B. Additionally, in order to increase the total absorption of the sample, we choose to focus on initial MEG samples which contain a high number of graphene layers, as presented in Table 2.3.

| Sample name | C1 | C2 |
|---|---|---|
| Number of graphene layers | 50 | 30 |
| GQDs diameter (nm) | 75 | $70 - 80$ |

Table 2.3: *Number of graphene layers of the MEG used to nanofabricate the GQDs arrays of batch C, with the corresponding GQDs dimensions after processing.*

Samples C1 and C2 exhibit an homogeneous aspect over the all the structured area ($\sim 1$ mm$^2$), as we can see on Figure 2.26.

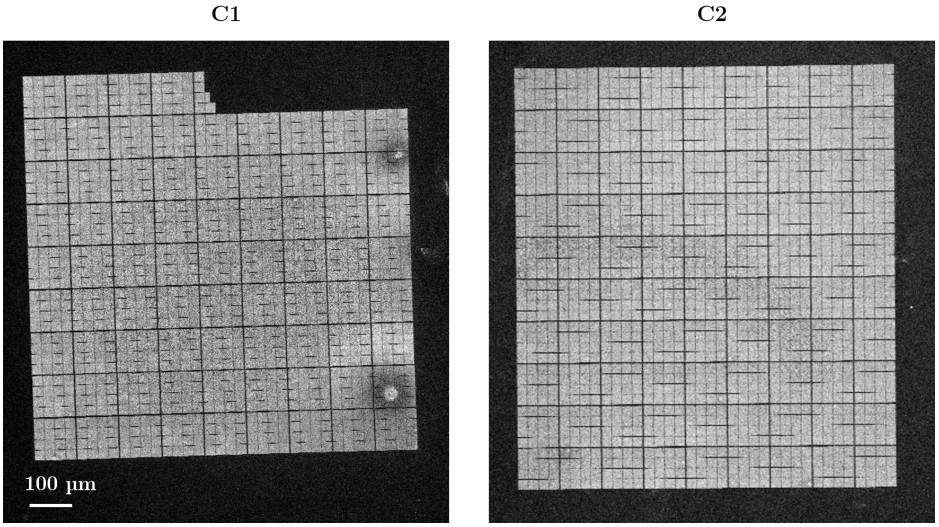


Figure 2.26: *SEM images of samples C1 and C2 after nanoprocessing, at the same scale indicated in C1 image. Both samples show no presence of residual contaminants on the surface and an homogeneous profile.*

The GQDs are also remarkably well defined over several $\mu$m$^2$, as shown in Figure 2.27 (left), and no sign of resist removal or dot merging is observed. At a lower scale Figure 2.27 (right), we see that sample C1 is composed by uniform GQDs of diameter 73 nm. In the case of sample C2, the GQDs are quasi-spherical and their diameter is found to be between 70 and 80 nm.

## 2.5 THz response of graphene quantum dots array

In this section we report the experimental results of the GQD arrays transmittance measurements using our THz-TDS system. We probe the THz properties of samples C1 and C2 made of GQDs on a SiC substrate (GQD/SiC), at low and room temperature ($T = 5$ K and 300 K, respectively). Two measurements are needed to compute the GQD transmittance using THz-TDS experiment: a first acquisition of the THz electric field passing through GQD/SiC and another one only through a SiC substrate, as reference.

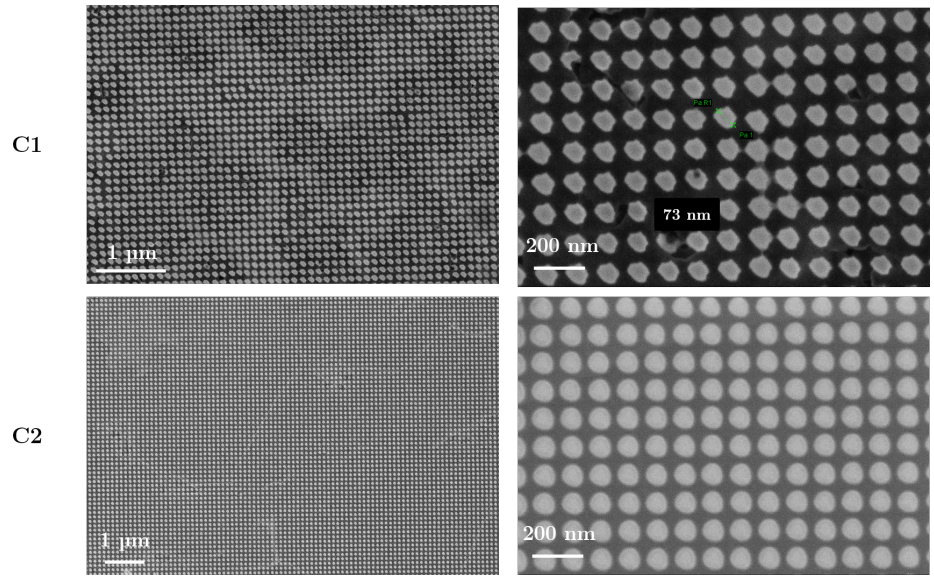


Figure 2.27: *SEM images of Sample C1 and C2 on large (left) and lower scale (right), on different areas. At large and low scale, no defect is observed in the structure, and the GQDs are uniform in size and well defined for both samples.*

### 2.5.1 Sample C1: thick multilayer GQD array

At first, we observe that the etched area of the substrate of C1 sample, where all the graphene layers have been entirely removed during the fabrication process, has a quite different aspect than a bare SiC substrate, where no graphene have been grown on. Figure 2.28 shows optical images of the sample, before and after processing, at different scales. We note the presence of black residual "holes" of about $\sim$ 2 $\mu$m diameter on the entire substrate, which cannot be removed by chemical etching[2]. In addition, Raman spectroscopy indicates that these residual "holes" contain carbon aggregates. From this observation, it follows that a rigorous reference for the transmittance measurement should be on the SiC after processing, i.e. on the same SiC substrate, away from the GQD array.

Unfortunately, the GQDs are nanostructured in the center of the SiC substrate to avoid thickness inhomogeneity of the e-beam resist on the edges after the spin coating step. Consequently, the easy-to-implement method, which consists in sticking the sample on a copper plate with two holes - one for the GQD array and one for the reference - is not acceptable as the two holes are too close, leading to a leak of the THz radiation on the unlighted hole. Consequently, we establish the protocol measurements of the THz transmittance as follow :

- At first, the transmittance $t_1$ of the GQDs array sticked on a holder with a 1.5 $mm$ diameter hole (see Figure 2.29 (a)) is measured with respect to the free space signal.

- The cryostat is opened and the sample is sticked again on the copper holder to measure the transmittance $t_2$ of the reference area (see Figure 2.29 (b)) with respect to the free space signal.

- Finally, we extract the complete transmittance of sample C1 as: $t_{C1} = \frac{t_1}{t_2}$

#### Transmittance spectra of sample C1

Figure 2.30 reports the measured amplitude transmittance of the GQD array C1 as function of the frequency at T=5 K and T=300 K. We first note that the order of magnitude of $t_{C1}(\omega)$

[2]After the nanolithography and etching step, another etching was performed to remove the holes, but it had no effect.

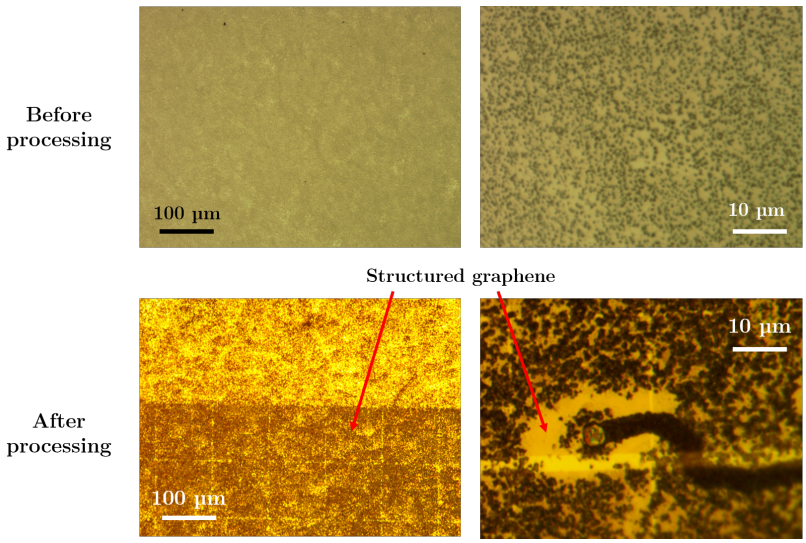


Figure 2.28: *Comparison between optical images of sample C1 before and after nanoprocessing, at large and reduced scale. The GQDs array obtained after nanostructuration is clearly visible by optical contrast (red arrows). On a lower scale, we note the presence of black "holes" in the structured graphene area, that are also present in the initial MEG sample.*

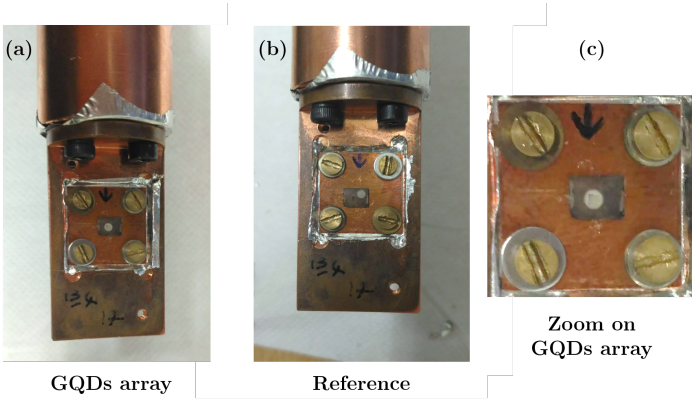


Figure 2.29: *Pictures of the sample sticked on holder with a 1.5 mm hole : (a) for the GQDs array transmittance mesurement $t_1$ and (b) for the measurement of transmittance $t_2$ of the reference area, away from the GQDs array. (c) Zoom on the GQDs array from picture (a): the graphene nanostructure is visible to the naked eye.*

is consistent with our initial estimation for sample C1 using 2.17, which gives $t(\eta = 0.3, N_l = 50) \sim 0.92$. At room temperature, we observe a broad dip centered at ~6.3 THz, which results in a monotonically decrease of the transmittance down to 0.92% as the frequency increases below 6 THz. This large dip corresponds to an absorption peak (resonance). The bandwidth of our THz TDS system limits the acquisition to $f$ <6.9 THz. We also observe an additional weak resonance around 3.8 THz. When the temperature is lowered to 5 K, the large dip is still observed; it is lightly less sharp and centered at a slightly lower frequency, 5.6 THz. We see two additional resonances around 1.5 THz and 3.5 THz. The latter is more pronounced than at 300 K. These two additional resonances possess similar bandwidth of typically 1 THz (i.e. 4.1 meV).

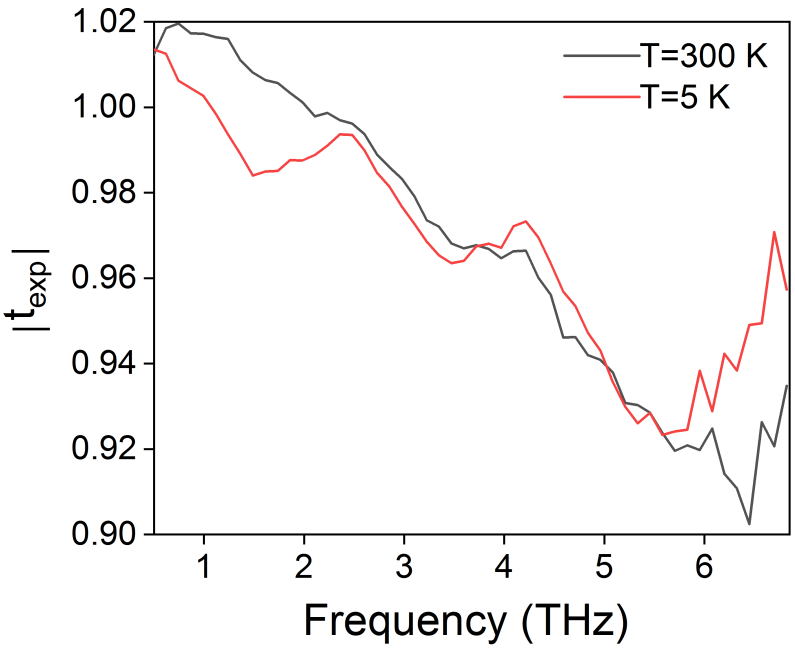


Figure 2.30: *Experimental transmission spectra of sample C1 at 300 K and 5 K.*

We clearly see that these tendencies strongly differ from the THz response of the multilayer epitaxial graphene (before nanoprocessing) studied in details in section 2.2(see Figure for comparison). Indeed, the evolution of the transmittance as the frequency is increased has opposite tendency: increasing for multilayer graphene due to Drude conductivity and decreasing for GQDs due to optical transition between electronic states. Moreover, the evolution as a function of temperature also differs, as for multilayer epitaxial graphene, decreasing temperature results only in a constant increases of the transmittance amplitude whereas for GQDs, the transmittance shows frequency shift of the resonance, changes in their amplitude and also the rise of an additional resonance. This is an important result of this thesis that reports, for the first time to our knowledge, the experimental transmittance of GQDs in the THz spectral range.
We note in Figure 2.30 that the transmittance is higher than 1 at low frequency, most probably due to an alignment difference of the THz beam between the sample and the reference measurement.

The main limitation of the experimental protocol used for this characterization of sample C1 is the requirement of two set of measurements, acquired during 2 consecutive but

different days. To overcome this issue of two distinct cool down operations for sample and reference measurements, some critical optimization of the epitaxial growth as well as of the experimental set-up are needed.

**Optimization of the experiment**

To allow consecutive measurements of the GQD array and of a proper SiC reference, the sample holder has to be redesigned. Due to the residual "hole" observed after nanoprocessing, the SiC reference and GQD signal must be performed on the same substrate of typical dimensions 3 $mm \times 4.5$ $mm$. Thus, the sample holder must support the entire substrate and enables two independent measurements as it cannot be cleaved neither before nor after nanostructuration in order to prevent from any damage on the surface. The sample holder consists in a copper plate with two holes aligned on the nanostructured graphene area and on a reference zone (without graphene). Due to the relatively weak absorption of the GQD array, the shapes and positions of the holes have to be strictly identical at a micrometer scale. Secondly, regarding the THz beam size at the focal point (see Section 2.1.2), holes cannot be neither too close to each other if ones want to avoid leakage of the THz radiation onto the neighbour hole, nor too far away considering the limited size of the substrate. I used a micro-mill machine to design 1.5 mm-diameter holes, with a center to center spacing of 2.1 mm. When a substrate is sticked on the sample holder, the extinction of the electric field between the holes is found to be $> 93\%$, indicating that there is almost no THz radiation leakage. Additionally, to prevent a beam clipping due to the divergence of the THz field around the focal point, we use a 300 $\mu m$ thick copper plate. This thickness still ensures a good thermal exchange between the copper and the sample when the system is cooled down. Regarding the small size of the holes compared to the THz beam size, alignment is also a critical parameter. That is why I have implemented a home-made fully automatised 3-axis stand to drive the sample and reference position.

### 2.5.2 Sample C2: intermediate thick multilayer GQD array

In this section, we investigate a new GQD array, sample C2, whose growth has been optimized to reduce the residual "holes" observed on sample C1. These residual "holes" are due to silicon gas escaping the substrate during the graphene growth step. Indeed, to produce a 50-layers graphene sample, the growing step has to be done several times, introducing more and more residual "holes" at each round. To overcome this issue, C. Berger and W. de Heer have fabricated a new series of multilayer epitaxial graphene with an intermediate number of graphene layers. They successfully fabricated a multilayer epitaxial graphene sample of $N_l \sim 30$ graphene layers with a significantly weak residual "hole" density. The residual "holes" have a depth of only 20-40 nm and a width of $<1$ $\mu$m. We thus expect after nanoprocessing to get GQD arrays of higher quality and clean SiC reference on the same substrate. We first examine the surface texture of sample C2 after nanostructuration.

The GQDs array pattern is remarkably clear on the optical images of sample C2 (see Figure 2.31), and the SiC substrate away from the GQD area shows no presence of residual "holes" at optical scale, in contrast with sample C1. Our observations are in agreement with prior AFM characterisations performed on the 30-layer MEG sample before nanostructuration.

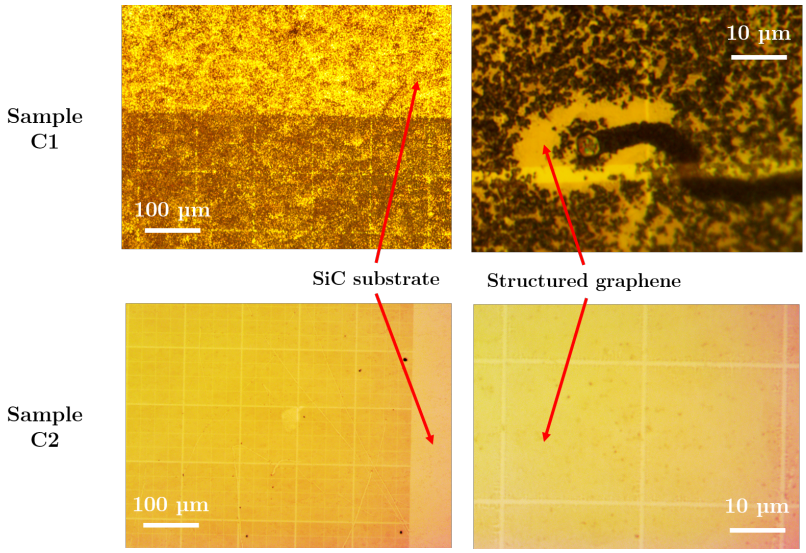


Figure 2.31: *Comparison between optical images of samples C1 and C2 after nanostructuration, at large and reduced scale. No "holes" are observed on sample C2 and the GQDs array pattern is clearly visible.*

### Experimental protocol

Sample C2 is sticked on a copper plate with two 1.5 $mm$-diameter holes as illustrated in Figure 2.32. The 1 $mm^2$ GQD array is carefully centered on the left hole.

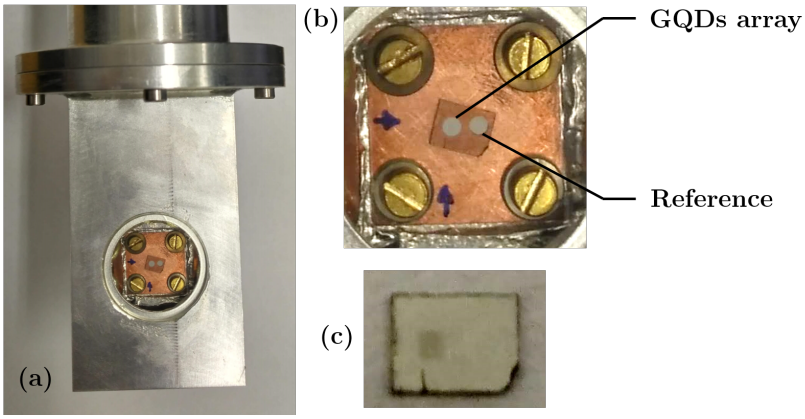


Figure 2.32: *(a)-(b) Pictures of sample C2 sticked on a two 1.5 mm-diameter holes holder, placed within the cryostat. (c) Picture of Sample C2 outside the cryostat. The GQDs array is clearly visible to the naked eye.*

### Transmittance spectra of sample C2

Figure 2.33 shows the measured transmittance of GQD array (Sample C2) as a function of the frequency, at $T = 5\ K$ and $T = 300\ K$. We observe a flat response between 0.5 and 3 THz for both temperatures corresponding to ∼1% absorption and a broad dip centered around ∼6 THz for both temperature. This large resonance, also observed in sample C1, represents a unique feature of the optical response of the GQDs at THz frequencies. We also observe at T=5K an additional very weak and broad resonance around 4 THz. The order of magnitude of $t_{C2}$ is, as expected, slightly lower than for sample C1, and also consistent

with our initial estimation, which gives $t(\eta = 0.3, N_l = 30) \sim 0.95$. These results represent the first experimental observation of the optical response of GQD in the THz spectral range. This is a first step towards the development of THz devices based on GQDs opening very interesting perspectives for THz technology.

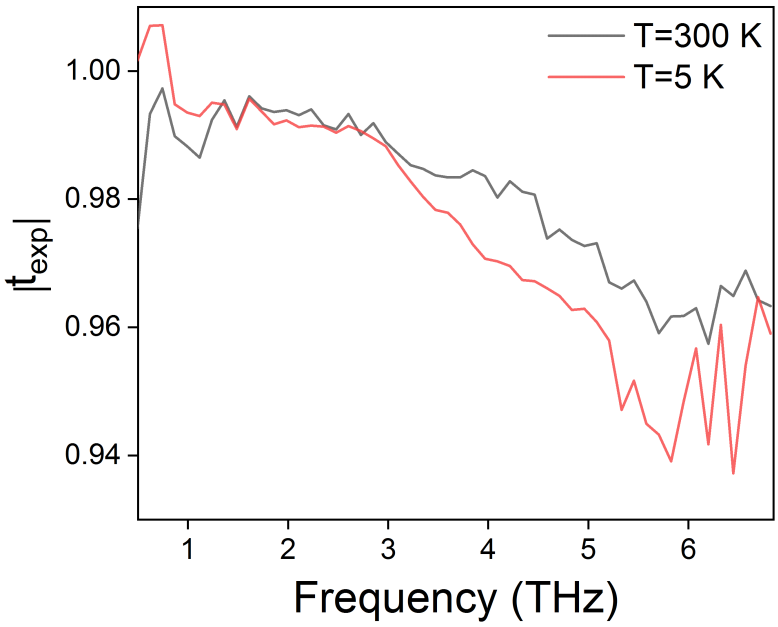


Figure 2.33: *Experimental transmission spectra of sample C2 at 300 K and 5 K.*

### Validation of the protocol

To demonstrate the validity of our previous measurements, we measure the transmittance of sample C2 using as a reference a distinct bare SiC substrate, from the same batch used for the epitaxial growth of the multilayer graphene. As we are no longer constrained by the limited size of the substrate, the GQD array C2 and the reference are sticked on 2.8 $mm$-diameter holes, with a center-to-center spacing of 4.3 $mm$. Room temperature acquisitions are performed, following the same experimental protocol as mentioned above. Figure 2.34 compares the experimental transmittance $t_{1.5}$ measured with a reference on the same SiC substrate and a 1.5 $mm$-diameter hole and $t_{bare\ SiC}$ measured with a reference on a bare SiC substrate and a 2.8 $mm$-diameter hole.

We note that the two measurements are remarkably well superimposed, thus highlighting two important conclusions: at first, we eliminate any edge-hole induced effect[3]. Additionally, as the 2.8 mm holes are well separated, we can also exclude a possible bias induced by a leakage of the THz beam on the neighbouring hole. Secondly, it validates our approach to tackle the reference issue: using a multilayer epitaxial graphene with an intermediate number of graphene layers allows to reduce the surface modifications on the SiC substrate, which stays similar to a bare SiC substrate.

[3]The small deviation observed in Figure 2.34 below 1.5 THz is attributed to a slight shift of 350$\mu$m between the GQDs array and the center of the hole.

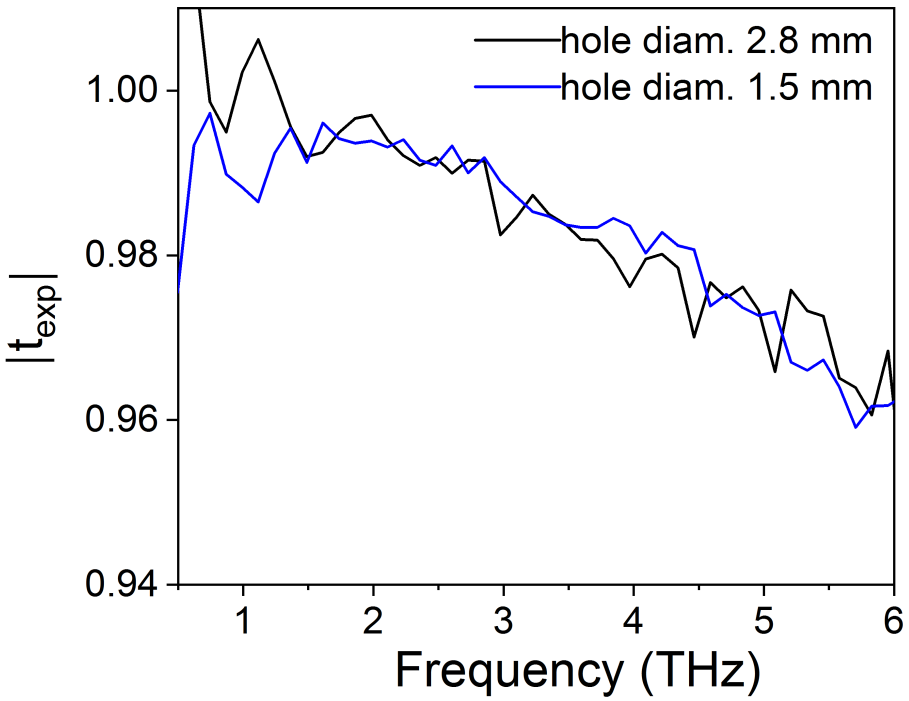


Figure 2.34: *Room temperature comparison of sample C2 transmittances, with different SiC substrates as reference. The spikes on the transmittance probably arise from a change in the humidity rate, which was about 0.3 % and 0.7% for* $t_{1.5}$ *and* $t_{2.8}$ *respectively.*

## 2.6 Comparison with tight-binding modelisation

In this section, we analyse the original experimental results on the THz response of GQDs through the tight-binding modelling presented in chapter 1. Our experimental study mainly reveals: 1/ the presence of a large resonance around 6 THz at 300 K and at a slightly lower frequency, around 5.8 THz, at 5 K and 2/additional weak resonances at low frequencies that are sharper and more numerous at low temperature. Due to computing issue, the largest GQDs that can be considered in the calculation have a diameter of D=2R=50 nm. However, the diameter of the GQDs of C1 and C2 samples falls in the range from 60 nm to 90 nm and 53 nm to 80 nm respectively, due to inhomogeneous dispersion. Consequently, we expect to observe experimentally an absorption resonance (i.e. a dip in the transmittance) at lower energy than that predicted. As developed in Chapter 1, the absorption probability $\alpha_{ML}$ of a monolayer GQD at frequency $\nu$ is defined by three parameters: the temperature $T$, the fermi level $E_F$ of the graphene layer, and the energy level broadening $\Gamma$.

$$\alpha_{ML}(\nu) = f\left(\nu, T, E_F, \Gamma\right) \tag{2.18}$$

As discussed in section 2.2, the graphene layers can be considered independent electronically (owing to the rotational stacking [67, 66]). Thus, we express the total absorption as the sum of all graphene layers, taking into account their respective Fermi level and the filling factor $\eta$ of remaining graphene after nanostructuration:

$$\alpha_{tot}(\nu) = \eta \sum_{N,E_F} \alpha_{ML}\left(\nu, T, E_F, \Gamma\right) \tag{2.19}$$

assuming that the temperature and the energy level broadening are constant for all graphene layers. Finally, using the Tinkham formula, we express the GQD array transmittance $t(\nu)$ as function of the frequency $\nu$ :

$$t(\nu) = \frac{1 + n_{SiC}}{1 + n_{SiC} + \pi\alpha_{tot}(\nu)} \tag{2.20}$$

### 2.6.1 Sample C1 modelling

As discussed in section 2.2, the multilayer epitaxial graphene used for the fabrication of the C1 sample, is composed by four heavily doped layers near the SiC substrate with Fermi levels of 360, 275, 130 and 80 meV above the Dirac point, and $N_{QD} = 49$ of quasi-neutral layers away from the substrate surface, with a Fermi level pins at the Dirac point by midgap states, $E_F \sim 0\ meV$. We start by considering a ratio $\eta = 0.318$ of remaining graphene, based on SEM images of sample C1 (see section 2.4.3).

$$\alpha_{tot} = \eta N_{QD}\alpha(E_F = 0) + \eta \sum_{i=1}^{4} \alpha_i(E_F \gg 1) \tag{2.21}$$

The phenomenological parameter $\Gamma$ is fixed to $1\ THz = 4.1\ meV$. This value corresponds to the half-width at half maximum of the absorption lobes observed in the experimental transmittance of C1 at $T = 5\ K$. We assume that it is appropriate as it is smaller or even much smaller than the typical width of absorption lobes observed in the averaged computed spectrum for $R = 25\ nm$ (see Chapter 1, section 1.4.2).

Figure 2.35 reports the theoretical transmittance $t_{theo}$ calculated for GQD of diameter $D = 50\ nm$ and the experimental transmittance $t_{exp}$ of C1 sample that contains GQDs with a dispersive diameter ranging from 60-90 nm. We observe that the theoretical transmittance $t_{theo}$ well reproduces the experimental data $t_{exp}$ at 300 K, namely a broad dip

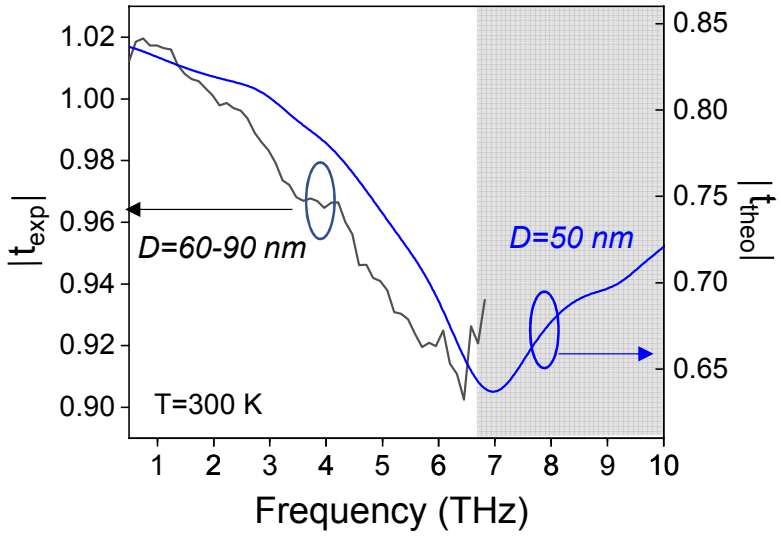


Figure 2.35: *Comparison between experimental $t_{exp}$ (black curve, left y-axis) and computed $t_{theo}$ (blue curve, right y-axis) transmittance of Sample C1, at $T = 300$ K. For $t_{theo}$, $\Gamma$ is fixed to 1 $THz = 4.1$ $meV$.*

around 6 THz, corresponding to a large absorption resonance. As expected, the dip of the experimental curve occurs at a lower frequency than that of the theoretical curve, due to the lower diameter of the GQDs used for calculation. It is however important to mention that the amplitude of the theoretical and experimental curves differs quite significantly (y-axis do not have same scale). Several reasons can be responsible for these differences in the amplitudes. First, the remaining graphene after nanostructuration could be much less than expected due to some dislocations and thus $\eta < 0.318$. Indeed, as shown in section 2.5.1 for C1 sample, the epitaxial growth of thick multilayer epitaxial graphene induced residual "holes" on the SiC surface. It is more likely that in these areas, due to the non-homogeneity of the surface, no GQD remains after the nanolithography. A significant reduction of $\eta$ down to 0.05-0.1 is thus an acceptable assumption.

At T=5K, the comparison between experiment and theory is also very consistent as reported in Figure 2.36. The broad dip is well reproduced by modelling (at higher frequency). Moreover, we observe weak resonances at low frequencies, that are more pronounced and more numerous than at T=300K. We can point out another very interesting feature that is the shift to lower frequency of the large resonance peak observed in experimental data when the temperature is decreasing is also observed in theoretical results: the peak frequency decreases from 7 THz to 6.7 THz when the temperature is reduced from T=300K to T=5K.

However, a main disagreement lies on the amplitude of the resonances between theory and experiment; the theoretical curves clearly overestimate the transmittance amplitude. Also, at frequencies below 3 THz, modelling predicts a relatively flat response in contrast to our experimental observations.

### Influence of the level broadening

To interpret the additional weak absorption resonance observed in the transmittance spectra that are more pronounced and more numerous at low temperature, we study the influence of the level broadening $\Gamma$. We report in Figure 2.37, the calculated transmittance at 5K

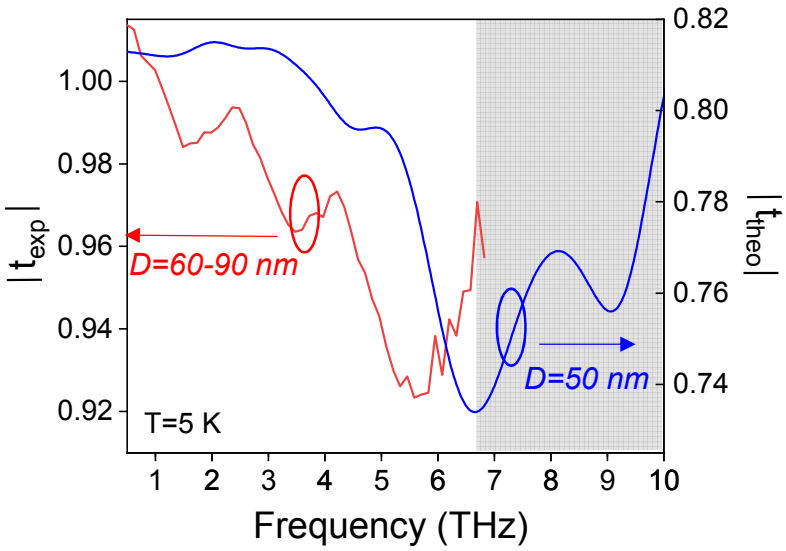


Figure 2.36: *Comparison between experimental $t_{exp}$ (red curve, left y-axis) and computed $t_{theo}$ (blue curve, right y-axis) transmittance of Sample C1, at $T = 5$ K. For $t_{theo}$, $\Gamma$ is fixed to $1\ THz = 4.1\ meV$.*

and 300K for different values of level broadening. We clearly observe that the value of $\Gamma$ strongly affects the amplitude, the shape and the number of observable resonances in the transmittance spectra in addition to the main dip. Moreover, less and weaker resonances are observed at T=300 K than at T=5K, in agreement with our experimental results. A more complete analysis of these weak resonances is under going to get insight on $\Gamma$ in our GQDs. An inhomogeneous broadening is expected due to the dispersion of the GQD geometry and the high number of dots in the GQD array ($\sim 10^7$). The knowledge of the homogeneous broadening could provide very interesting information as the relaxation time of carriers $\tau$ is linked to the level broadening[4] $\Gamma$ by Heisenberg's uncertainty principle: $\tau \sim \hbar/2\Gamma$. To get some information on the relaxation, we plan to perform optical pump-THz probe experiments.

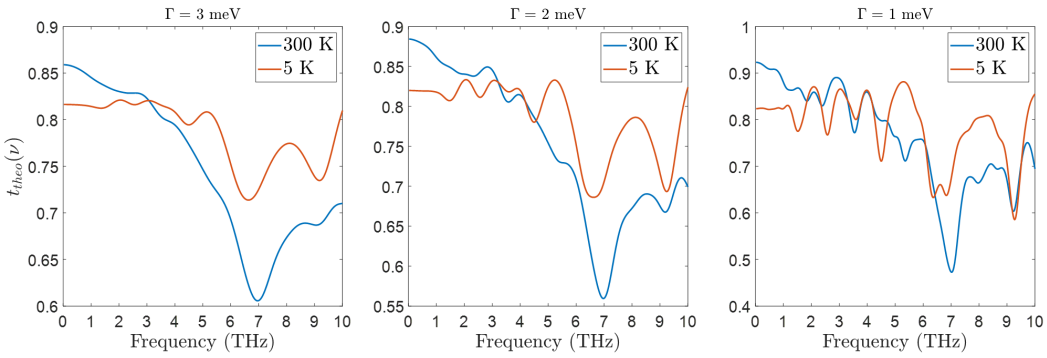


Figure 2.37: *Computed sample C1 transmittance at $T = 300$ and 5 K, for different values of the level broadening $\Gamma$, with $\eta = 0.318$ and $N_{QD} = 49$.*

[4]As we defined $\Gamma$ to be the half width at half maximum of the Lorentzian functions in the absorption probability expression of Chapter 1, we include a factor 2 in the lifetime estimation.

### 2.6.2 Sample C2 modelling

The initial 30-layer MEG, used to fabricate Sample C2, was produced following similar epitaxial growth steps to those for the 50-layer MEG used to fabricate Sample C1. It is thus also composed by four heavily doped layers near the SiC substrate (with Fermi levels of 360, 275, 130 and 80 meV respectively) and $N_l = 26$ layers away from the substrate. Prior to its nanostructuration, magnetospectroscopy measurements have been performed by M. Krizman and L.A. De Vaulchier to get the Fermi level energy of these $N$ layers. Their analysis has revealed a Fermi level energy $E_F$=20 meV (see Appendix for a detailed description).

#### Sample C2 modelling

Figure 2.38 reports the experimental transmittance spectra $t_{exp}$ at room temperature and the calculated transmittance spectra $t_{theo}$ assuming, as previously, a ratio $\eta = 0.318$ and $\Gamma = 1$ THz $= 4.1$ meV. We confirm that the computed transmittance well describes the main features of the experimental data, in particular the large dip around 6 THz. As already explained, the frequency shift between the theoretical and experimental peaks is due to the lower diameter of the GQDs considered in calculation. However, the amplitude of the predicted main resonance is still significantly larger than that observed by the experiment.

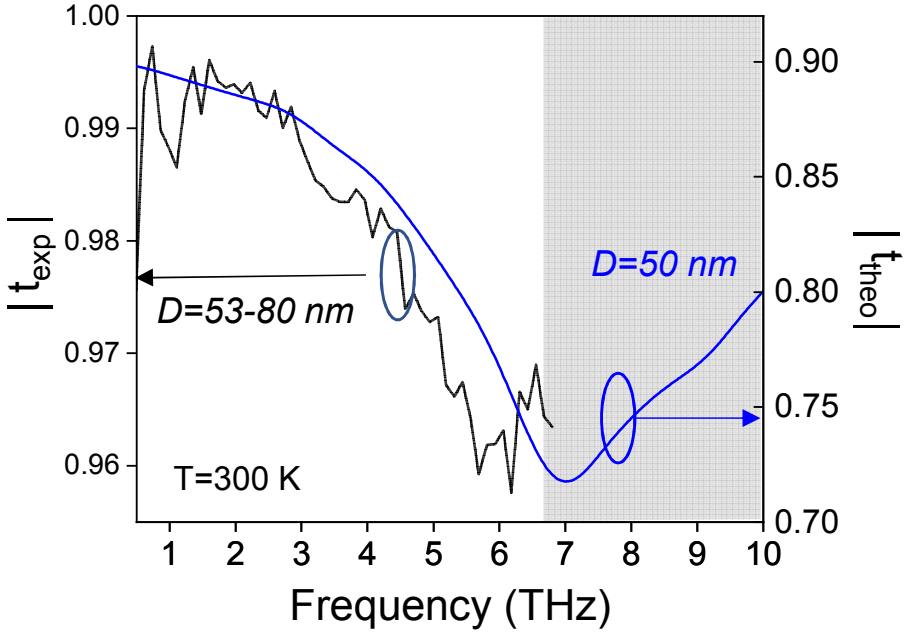


Figure 2.38: *Comparison between experimental $t_{exp}$ (black curve, left y-axis) and computed $t_{theo}$ (blue curve, right y-axis) transmittance of Sample C2, at $T = 300$ K. For $t_{theo}$, $\Gamma$ is fixed to 1 $THz = 4.1$ meV.*

Similarly, modelling and experimental results well agrees at T=5 K. Interestingly, whereas no frequency shift of the main resonance is observed between T=5 K and T=300 K, in contrast with Sample C1, modelling also predicts the absence of the frequency shift. Also, additional weak resonances, that are not observed at room temperature, appear in the theoretical and modelling spectra.

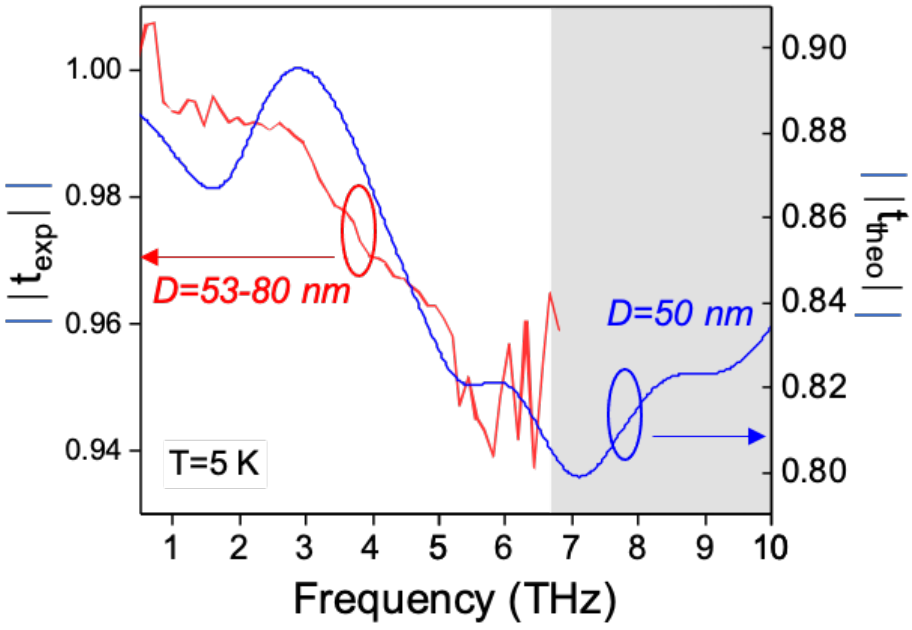


Figure 2.39: *Comparison between experimental $t_{exp}$ (red curve, left y-axis) and computed $t_{theo}$ (blue curve, right y-axis) transmittance of Sample C2, at $T = 5$ K. For $t_{theo}$, $\Gamma$ is fixed to $1\ THz = 4.1\ meV$.*

**Study on the influence of temperature on t($\omega$)**

Using our complete modelling, we study the respective contribution of the doped and quasi-neutral layers in the total transmittance spectra to get a better understanding of the evolution of the transmittance spectra with temperature for both samples. If we consider GQDs only composed by four heavily doped layers (with $E_F \geq 80$ meV), we see on Figure 2.40 (a) that the main absorption lobe is nearly independent of the temperature change. We attribute this behavior to the fact that the transmittance profile arises from efficient intraband transitions, that are allowed because of the high Fermi level values and thus is consequently poorly affected by temperature.

We now consider GQDs composed by only the quasi neutral layer, i.e. $N_l = 50$ layer with $E_F = 0$ meV for sample C1 and $N_l = 26$ with $E_F = 20$ meV for sample C2. We observe on Figure 2.40 (b) and 2.41 (b) that, owing to the broadening of the carrier distribution at room temperature, on the order of $k_B T_{300K} \sim 26$ meV, some carriers get enough energy to participate to the efficient intraband transitions at higher energy. These intraband transitions involves mixed and bulk states. In contrast, at low temperature, as discuss in Chapter 1, the carrier population occupy electronic states at low energy. The corresponding intraband transitions involves only mixed states and that are less numerous and more spread out.

For the full stacking of sample C1, the contribution of the 50 quasi-neutral layers is important relatively to the doped layers and thus the change in the transmittance of these quasi-neutral layers with temperature is also observable in the total transmittance of the full structure. In return, for sample C2, the contribution of the lightly doped layer is weak and therefore there is no frequency peak shift in the total transmittance in agreement with our experimental results.

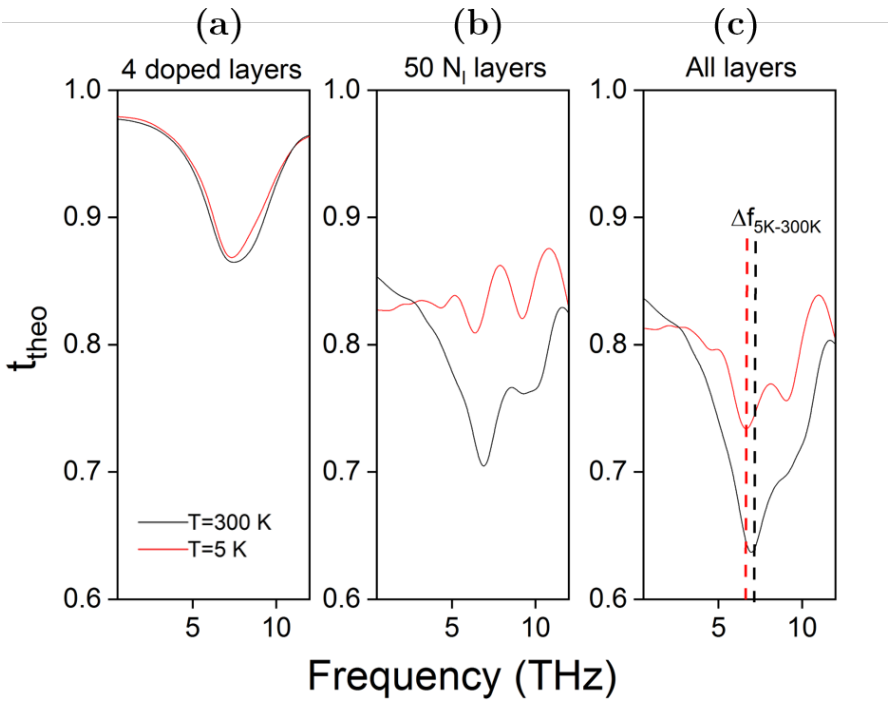


Figure 2.40: *Computed transmittance $t_{theo}$ at T=5K (red curves) and T=300K (black curve) for different compositions of the GQD: (a) only 4 doped layers, (b) only 50 layers with $E_F = 0$ meV and (c) full stacking: sample C1.*

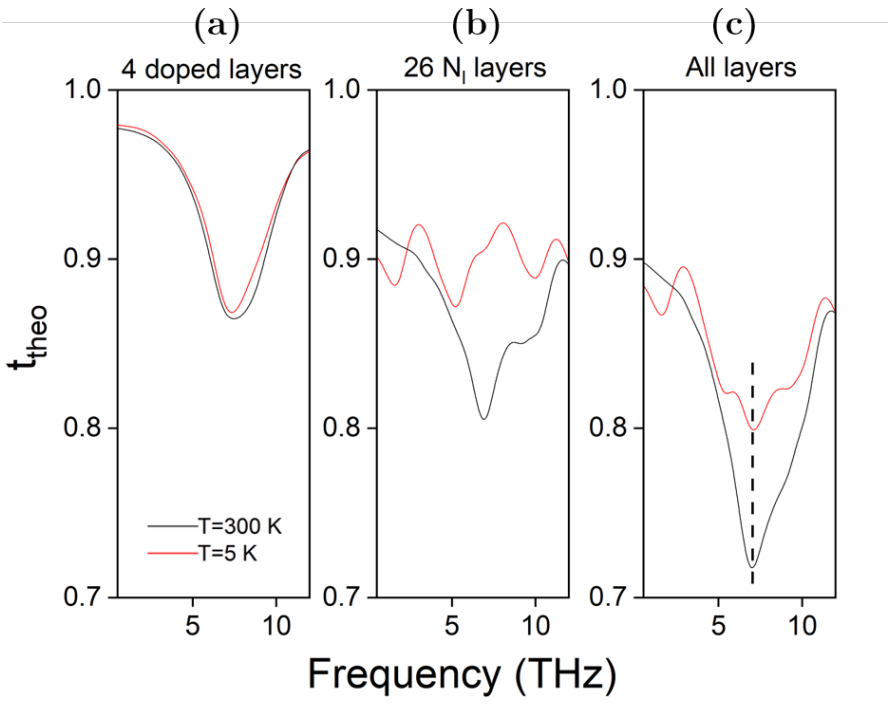


Figure 2.41: *Computed transmittance $t_{theo}$ at T=5K (red curves) and T=300K (black curve) for different compositions of the GQD: (a) only 4 doped layers, (b) only 26 layers with $E_F = 20$ meV and (c) full stacking: sample C2.*

## 2.7 Optical-pump THz-probe experiments

Understanding and ultimately controlling the relaxation and recombination dynamics of non-equilibrium carriers in graphene and related materials is of interest for fundamental studies of elementary process and of paramount importance for the development of optoelectronic devices. The relaxation and recombination dynamics of non-equilibrium carriers in graphene has been widely investigated [13],[72],[78],[79] (see illustration in Figure 2.42). Mostly, femtosecond visible or near infrared pulses are used to generate hot non-equilibrium carriers of large density at high energies. After photoexcitation, the electron/hole populations are both redistributed (by energy-conserving intraband carrier-carrier scattering) and relaxed (by intraband electron-optical phonon scattering) within ∼50 fs. It results in two independent lower energy broad electron and hole distributions, for which efficient interband Auger recombination processes leads to a single Fermi-Dirac distribution for conduction and valence populations within 100-200 fs. A subsequent cooling process occurs mediated by interband optical phonon emissions within 1-2 ps and by less efficient intraband acoustical phonon scattering. Few studies have used optical pump with energies lower than optical phonon energy and reported significant slowing of the carrier relaxation [80]. However, owing to the excitation of a large density of hot carriers, optical phonon emission remained the predominant relaxation channel [78], [81].

In spite of these intensive works performed in graphene, there is no investigation of the hot carrier relaxation dynamics in graphene nanostructures and in particular in graphene quantum dots. However, several processes are expected to be altered by the reduction of in-plane dimensions of the graphene layer. The main one is the Auger recombination process. Indeed, as Auger recombination is a scattering process in which the recombination of an electron–hole pair pushes another electron to higher energy, one would expect that the full discretization of electronic states should significantly limit available final states for the scattered electron. Auger coupling have been studied in small GQD by I. Ozfidan *et al.*. Their prediction showed the existence of two electron-hole pair states stable against Auger recombination [82]. In addition, it has been shown in analogous systems that Auger coupling is decreased with increasing quantum dot size [83]. Moreover, the electron-phonon interaction is supposed to be modify by the phonon modes resulting from the confinement.

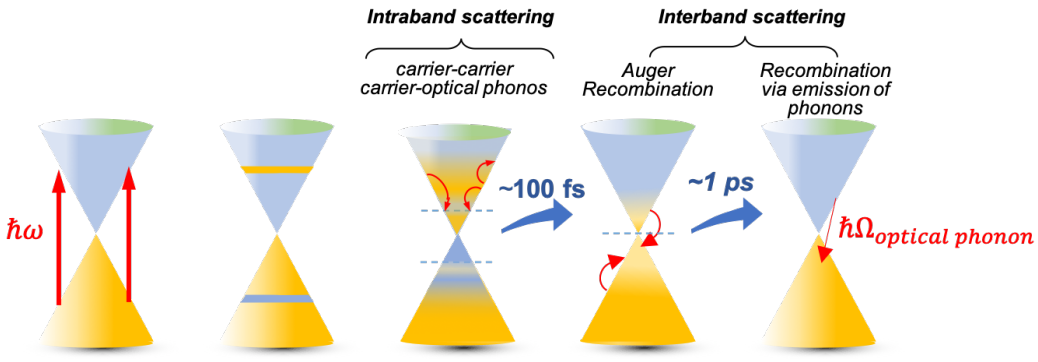


Figure 2.42: *Scheme of the relaxation and recombination dynamics of non-equilibrium carriers in graphene probed by pump-probe experiments. Carrier multiplication effects are not considered here.*

In order to probe the carrier dynamics in GQD arrays, I have extended the initial TDS setup by implementing an optical-pump line to perform optical-pump THz-probe experiments. In pump-probe spectroscopy systems, an optical pump pulse is used to generate non-equilibrium carriers in the graphene, which modify the intraband and interband con-

ductivity; a weaker probe pulse is subsequently used to map the cooling of these hot carriers with sub-ps resolution by comparing the transmission of the probe beam with and without the excitation pulse.

### 2.7.1 Description of the setup

A schematic view of the optical-pump line part is shown in Figure 2.43. After the first beam splitter, on the optical path towards the antenna, another beam splitter separates the infrared beam into two different directions: (1) towards the antenna and (3) for the optical-pump line. In order to get enough power for the pump line without degrading the signal-to-noise ratio of the THz emitted by the antenna, the beam splitter ratio is set to 70% in reflection and 30% in transmission. The infrared beam on the path (3) is mechanically modulated by a chopper for detection. A first lens focuses the infrared on the chopper in order to reduce the beam size and thus enabling a higher frequency modulation. A second lens, mounted on a removable stage, collects the beam, which finally travels on a delay line that will set the time delay between the infrared and the THz pulse on the sample.

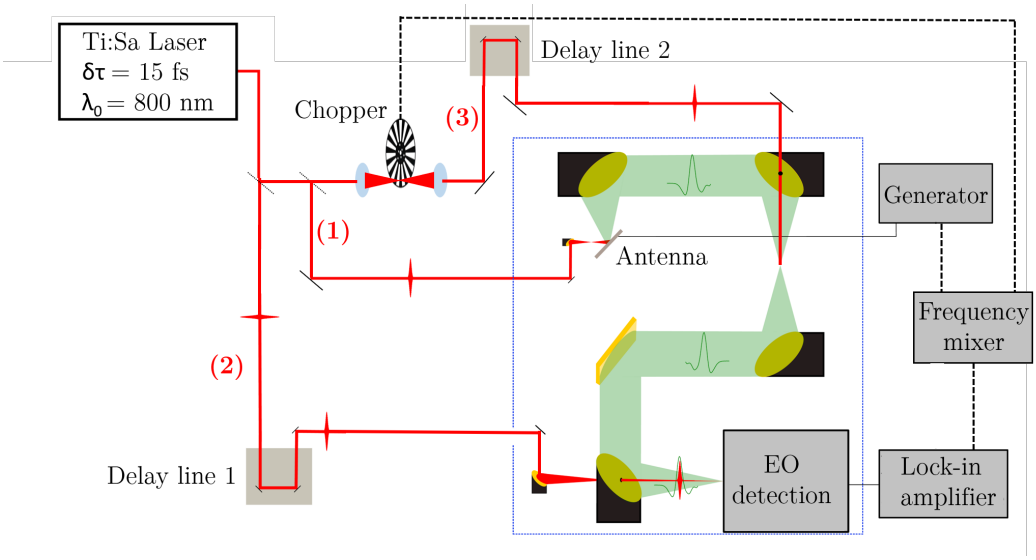


Figure 2.43: *Sketch of the optical-pump line added on the THz-TDS setup presented in section 2.1*

.

By acting on the position of the second lens, one is able to focus the infrared beam on the sample to maximize the incident power, or instead increase the spot diameter on the sample and thus reduce the power flux to prevent any damage for sensitive samples.

### 2.7.2 Double-modulation detection

As photoexcited carriers induce change in the transmittance of the THz electric field, we probe the dynamics of photoexcited carriers in the GQD by measuring the THz electric field through the GQD arrays after photoexcitation by the infrared pump, $E_{THz}^{ON}$ and without the photoexcitation, $E_{THz}^{OFF}$ . Regarding the low absorption of the GQD arrays, we expect the amplitude of the differential transmittance to be low as well. Hence, it is critical to develop a detection that provides a high enough signal-to-noise ratio.

The signal $S(t)$ we want to detect results from the interaction between the THz electric field produced by the photoconductive antenna electrically modulated at a frequency $f_1 = 42\ kHz$, and an infrared pulse mechanically modulated by a chopper at a frequency $f_2$

(adjustable from 1 to 10 kHz). These two techniques provide square modulated signals but, for simplicity, we will consider sinusoidal modulations.
We first describe the single frequency homodyne detection of the THz signal $V_I \sin(\omega_1 t + \phi_1)$. The lock-in amplifier creates an internal reference signal $V_r \sin(\omega_r t + \phi_r)$, and the the target signal detected by the lock-in amplifier with single modulation writes:

$$\begin{aligned} S_{SM} &= V_I \sin(\omega_1 t + \phi_1) V_r \sin(\omega_r t + \phi_r) \\ &= V_r V_I \left( \frac{1}{2} \cos\left[(\omega_1 + \omega_r)t + \phi_1 + \phi_r\right] - \frac{1}{2} \cos\left[(\omega_1 - \omega_r)t + \phi_1 - \phi_r\right] \right) \end{aligned}$$

When we knob the frequency $\omega_r$ and reference phase $\phi_r$ to $\omega_1$ and $\phi_1$ respectively, which is in real experimental conditions done via an external transistor-transistor logic (TTL) signal sent by the antenna modulator, we are able to measure the DC component $\frac{1}{2} V_r V_I$ that is the THz signal.
The double modulation follows the same method, and we use a homemade frequency mixer to sum up the frequency of THz generation $f_1$ trigger signal and the frequency $f_2$ of the chopper trigger signal. In this case, the target signal writes:

$$\begin{aligned} S_{DM} = \frac{1}{4} V_r V_I \Big( & \cos\left[\omega_r t + (\omega_1 + \omega_2)t + \phi_r + \phi_1 + \phi_2\right] \\ & + \cos\left[\omega_r t - (\omega_1 + \omega_2)t + \phi_r - \phi_1 - \phi_2\right] \\ & - \cos\left[\omega_r t + (\omega_1 - \omega_2)t + \phi_r + \phi_1 - \phi_2\right] \\ & - \cos\left[\omega_r t - (\omega_1 - \omega_2)t + \phi_r - \phi_1 + \phi_2\right] \Big) \end{aligned}$$

When we detect the input signal at $\omega_1 + \omega_2$ via a TTL signal send by the frequency mixer on the lock-in amplifier, we thus acquire the DC component $\frac{1}{4} V_r V_I$ which corresponds to the change a change in the transmittance of the THz electric field, induced by the infrared pump. The infrared beam diameter is adjusted by the position of the lens to 1.5 $mm$ on the sample. The spatial overlap between the infrared and THz beam is optimised by maximizing the differential transmittance signal on a reference sample (300 $\mu m$-thick GaAs substrate). Figure 2.44 shows the experimental transmitted electric field dymanics of the reference sample after optimisation. The temporal step is 8 $fs$ and the lock-in time constant is 300 $ms$. For a GaAs substrate, the signal-to-noise ratio reaches $\sim 65$ and the rise time is of $\sim 400 - 450$ $fs$. The temporal resolution of our pump-probe measurement is limited by the duration of the optical pulses to ∼100 fs.

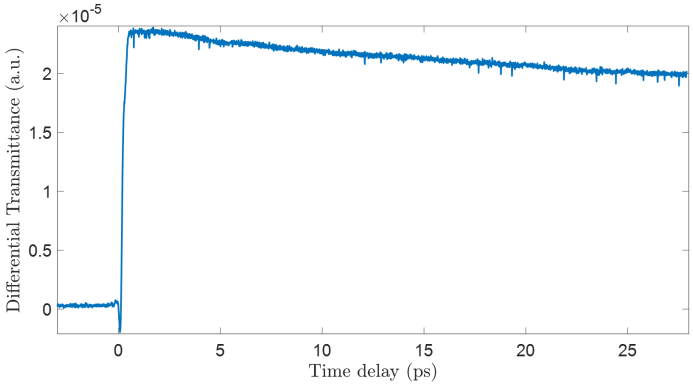


Figure 2.44: *Differential transmittance amplitude measured on a GaAs substrate, used as a reference to optimize the spatial overlap between the infrared and THz beams.*

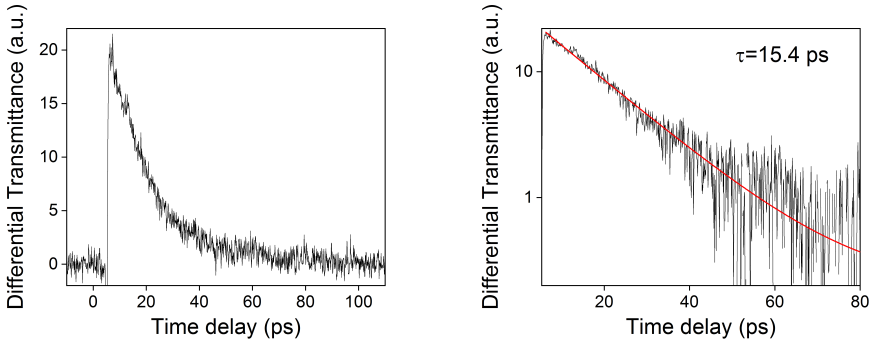


Figure 2.45: *Differential transmittance amplitude measured on multilayer epitaxial graphene, before processing. The experimental data is fitted with a mono-exponential decay (red line) and gives a time constant of 15.4 ps.*

### 2.7.3 Multilayer epitaxial graphene

As a first investigation, we probe the dynamics of the non-equilibrium carriers in the multilayer epitaxial graphene before their nanoprocessing. The differential transmittance amplitude of the THz probe pulse as a function of the pump-probe delay time, measured at $T = 5\ K$ is reported in Figure 2.45.

The temporal resolution of our experimental set-up prevents to observe the ultrafast intraband relaxation of the hot carriers resulting form electron-electron scatterings as they occur with 50fs-100fs time scale. To extract relaxation times the experimental data is fitted by a mono-exponential decay (red line in Figure 2.45 right). The resulting time constant is 15.4 ps. The observation of such timescale of tens of picoseconds is consistent with previous results obtained in experimental studies performed on similar multilayer epitaxial graphene [72]. Their complete analysis has demonstrated that the dynamics of hot carriers in these multilayer epitaxial graphene with large number of quasi neutral layers are dominated by the combined effect of efficient carrier–carrier scattering, which maintains a thermalized carrier distribution, and carrier–optical–phonon scattering, which removes energy from the carrier liquid. By selectively switching on and off the different scattering processes in their model, they show that the acoustic phonon modes have negligible contribution to the observed THz carrier dynamics on the timescale of tens of picoseconds.

### 2.7.4 Hot carriers dynamics in graphene quantum dot arrays

We made several tentative to probe the dynamics of non-equilibrium carriers with the GQD arrays. We measured very small signals that we are currently optimizing to extract properly the dynamics. In future, based on the improved knowledge we get from both the theoretical and experimental investigation of these new objects, we plan to probe multilayer doped graphene samples that should provide larger THz response and enables to detect significant differential transmission.

### 2.7.5 Conclusion

In this chapter, we have presented the experimental investigation of the optical properties of GQDs array made of multilayer epitaxial graphene in the THz range. Our results show that the THz response of GQDs with diameters of few tens of nm is characterised by a large absorption resonance around 6 THz at low and room temperature. Additional weak absorption resonances at lower frequency are also observed at low temperature. These results are

supported by the theoretical analysis developed in Chapter 1 that highlights the contribution of doped and quasi-neutral layers of the GQDs.
This is an important result as we report experimentally, for the first time to our knowledge the transmittance spectra of large GQDs at THz frequencies. Their response strongly differ from the THz absorption of multilayer epitaxial graphene.

Our measurements and analysis show that transitions at THz frequencies can be induced in GQDs at low and room temperature and that their properties can be tuned by the doping and size of the GQDs. Therefore, GQD with diameter of few tens of nanometers are very appealing for the development of THz devices such as compact THz lasers and low noise THz detectors.

# Chapter 3

# Dark transport and photo-transport in a single graphene quantum dot

In the previous chapter, we have probed the optical properties of arrays of GQDs using THz-TDS system and demonstrated a broad absorption feature around 6 THz. Due to the significant size dispersion of the GQDs that compose the arrays, their THz response includes inhomogeneous broadening effects. In order to overcome this inhomogeneous effect and to get additional insight in the electronic and optical properties of GQD of few tens of nanometers in diameter, we study in this chapter the dark quantum transport in a single GQD and the photo-transport under incoherent THz illumination. This chapter includes parts of our full article [84].

In this chapter, after a brief review of experimental studies on GQDs of a few tens of nanometers in diameter, I present the fabrication process of the single GQD inserted within single electron transistors coupled to a bow-tie THz antenna. I then report dark transport measurements in the GQD-based transistors that show Coulomb blockade regime and excited states of the GQD. Finally, we provide the photoresponse of the GQD in the Coulomb blockade regime under incoherent THz illumination. This study has been performed in close collaboration with Takis Kontos and Sebastien Balibar (Mesoscopic Physic's group at LPENS).

## 3.1 Experimental studies on large GQDs

Until now, GQDs of a few tens of nanometers in diameters, i.e. large GQD, have been realized by top-down lithography and etching of graphene layers. Most of the experimental works on large GQDs was dedicated to the study of quantum transport phenomena. The first work investigating transport in GQD was reported in 2004, with the measurement of Coulomb-blockade oscillations in thin graphite flakes with highly resistive contacts as tunneling barriers [85]. Then, in 2008, tunable Coulomb blockade have been demonstrated in a GQD made by etching a single exfoliated graphene flake and using graphene side gates [86]. These pioneer works have initiated several subsequent experimental investigation of quantum transport in GQD. Major achievements include the observation of more regular Coulomb blockade diamonds than in graphene nanoribbons [87], the observation of excited states, co-tunnelling lines due to quantum confinement, a fluctuating Coulomb peak spacing [88] and the implementation of charge detection [89], [90](see Figure 3.1). In most works, the

sample scheme is a graphene island connected to graphene leads with small constrictions. The influence of the constrictions on transport through GQDs was discussed in various experiments and is often assume that GQD with the constrictions behaves as a single electron transitor due to co-tunnelling effects in the 'constriction dots' [91]. An important work in the general context of this thesis was perfomed by C. Volk et al. that have measured transient currents through electronic excited states and demonstrated long charge carrier relaxation times in GQD of 60–100 ns [92]. Besides, related works have been carried out in graphene double quantum dots and the expected hexagon patterns as well as the excited states were observed. Additionally, precious insights into charge and spin states were gained by measuring transport in GQD in magnetic fields [90]. However, the influence of disorder, in particular the edge disorder turned out to be a major limitation for obtaining clean GQDs with a controlled number of electrons, holes and well tunable tunnelling barriers [93]. To overcome this issue, a recent and promising approach have been implemented based on the use of bilayer graphene with its electrostatically induced band gap to fabricate a fully gate-defined device with quantum dots [94], [95], [96].

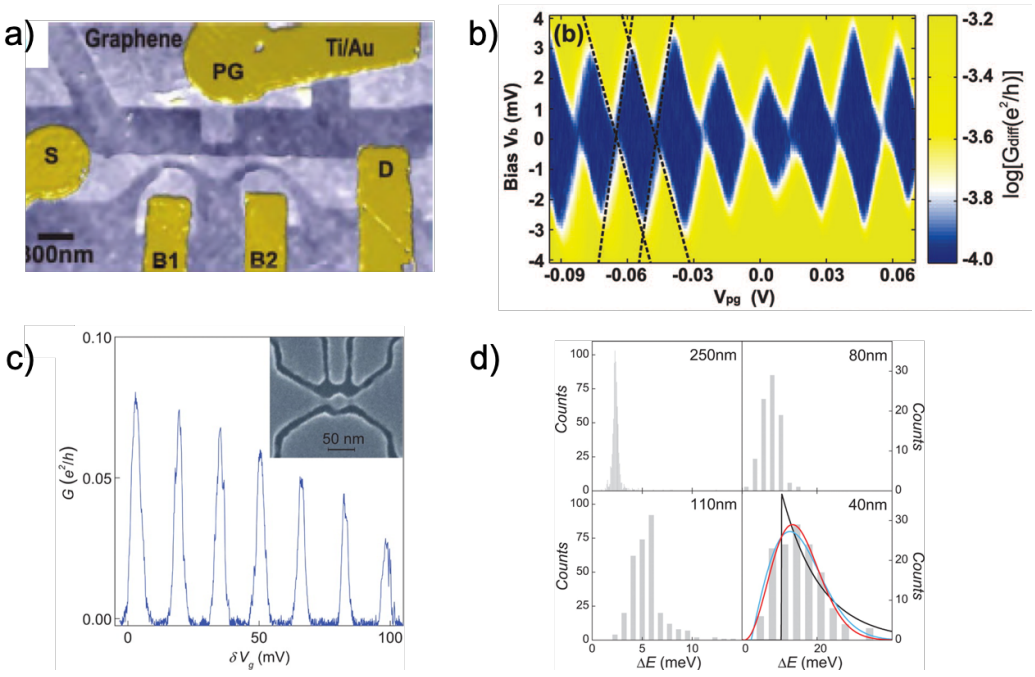


Figure 3.1: *a) Scanning force microscope image of a graphene single electron transistor device. b) Coulomb diamonds in differential conductance, represented in a logarithmic color scale plot. A dc bias with a small ac modulation is applied symmetrically across the dot and the current through the dot is measured. From Reference [97]. c) Conductance of a graphene-based single-electron transistor (image in insert) with the central island of 250 nm in diameter and distant side gates as a function of gate voltage. d) Histograms of the nearest-neighbour level spacing in GQDs of different diameter. The spacing was determined by measuring the size of Coulomb diamonds. From Reference [88].*

Beyond these transport studies, recently, the group of the P. Barbara (Georgetown University) has demonstrated large bolometric effects in quantum dot constrictions nanostructured in epitaxial graphene grown on SiC when illuminated with THz photons. A huge variation of resistance with temperature was obtained, $R > 430\ \mathrm{M\Omega K^{-1}}$ below 6 K, owing to electronic confinement [98]. However, as no gate electrodes were used to isolate the quantum dots from the leads and to control the chemical potential inside the GQDs, the bolometric effect was limited to THz heating [99]. Although many interesting phenomena can be revealed in single electron transport regime, the investigation of the THz response of GQDs in

the Coulomb blockade regime remains elusive. In this thesis chapter, which is part of this general context, we study the dark transport of a GQD-based single electron transistor and its photoresponse in Coulomb blockage regime under incoherent THz illumination.

## 3.2 Fabrication process

### 3.2.1 Challenges overview

The main technological challenge in fabricating graphene-based nanodevices is to limit disorder that hinders the confinement of the Dirac electrons and prevent from achieving low doping values. Previous works have shown that by placing graphene on a hBN layer reduces significantly bulk disorder as compared to Silicon oxide ($SiO_2$), especially for very large GQD ($>$ 200 nm of diameter) [100]. Our strategy to further reduce the disorder of the GQD is to fully encapsulate the graphene with two hBN layers as a first step of the fabrication process [101]. Thus, the GQD is isolated from the substrate (down hBN layer) and is also preserved from chemical contaminations (top hBN layer).

The full encapsulation process required substantial developments, as we started this activity from scratch. From the moment when the assembly process has made it possible to obtain a statistical batch of heterostructures (see 3.2.3), several nanolithographies were performed, with different types of process. We fabricate GQD-based single electron devices in which the leads, the constrictions and the GQD are made of hBN-encapsulated graphene. In this section, we detail the different steps of the fabrication process for three different samples (A1, A2 and B) with iteratively improved fabrication method and geometries. I initiated the technological development by fabricating sample A1; based on this development, Elisa Riccardi, a post doc of our research team, has fabricated the next generation of samples, samples A2 and B.

### 3.2.2 Mechanical exfoliation of hBN and graphene flakes

The fabrication of the hBN/graphene/hBN heterostructure starts with the micromechanical exfoliation of monolayer graphene and hBN flakes from natural graphite and ultra-pure hBN single crystals [102] respectively. For graphene exfoliation, we use a blue tape, which is then put on a $SiO_2$ substrate and annealed around 120°C for few minutes. The blue tape is slowly removed and the potential graphene monolayers (typical size $\sim 20 - 40\ \mu m$) are firstly identified using optical microscope (see Figure 3.2). The monolayer criteria is straightforwardly confirmed using Raman spectroscopy. For hBN exfoliation, we employ a

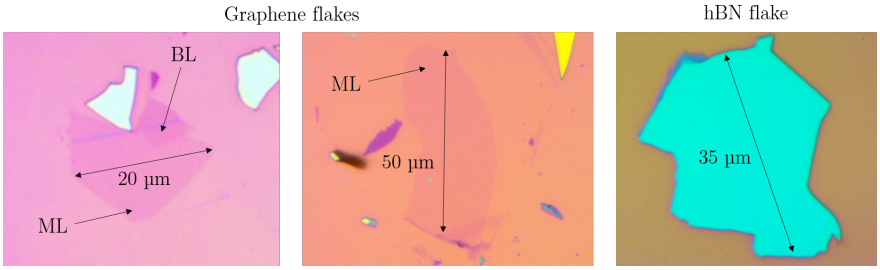


Figure 3.2: *Optical images of graphene and hBN flakes on $SiO_2$ substrate. Monolayer (ML) or bilayer (BL) graphene flakes can be identified by optical contrast after exfoliation.*

reusable Polydimethylsiloxane (PDMS) support, transfer the hBN flakes on a $SiO_2$ substrate,

and select those with few tens of layers using optical microscope. In order to perform a fully encapsulation, the selected hBN flakes have to be larger than the graphene monolayer.

### 3.2.3 Encapsulation

The heterostructure assembly is performed using a Polypropylene carbonate (PPC) coated PDMS block mounted on a glass slide - define as a stamp - to capture (pick-up) and release (drop-down) the 2D materials. First attempts were done at room temperature but the process was time-consuming and the success rate very low. We thus turn onto the hot pick-up technique, which enables the rapid batch fabrication of Van der Waals heterostructure [103], by controlling the temperature during each steps of the assembly (description in Figure 3.3). To this aim, a new setup was implemented in our clean room, composed by a 3D micromanipulator, which holds the stamp, fixed to a heated microscope stage (see Figure 3.4).

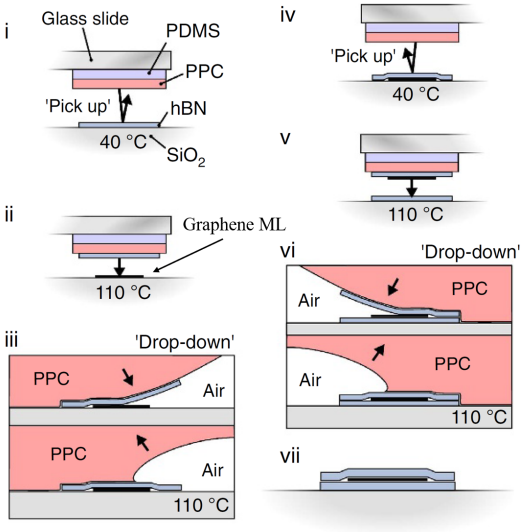


Figure 3.3: *Chronological description (from i to vii) of heterostructure assembly using hot pick-up technique. (i) The top hBN layer is lift from the substrate at 40°. (ii)-(iii) The $SiO_2$ substrate supporting the graphene is heated up to 110° during the drop-down step, and finally covered by an hBN flake. (iv) The top hBN/graphene assembly is captured by the stamp at 40°. (v)-(vi)-(vii) The top hBN/graphene on stamp is finally released on a bottom hBN flake at 110°, leading to a fully hBN-encapsulated graphene. Images taken from Reference [103].*

In addition, we modified the stamp structure used in [103]. It was initially composed by a flat PPC film, mechanically peeled off by a scotch tape, which is curved with an opening window and then attached onto a PDMS cube on a glass slide (Figure 3.5a)). Instead, we put a drop of PDMS on a glass slide, let it dry 24h face-down, clean it with $O_2$ plasma for 10 min, spin coat PPC directly on the dry drop and let the stamp rest for 2 days. The hemispherical profile of the stamp (Figure 3.5b)) improves the capture and the release of the flakes, together with a reduced ripping probability (see images of the heterostructure assembly process in Figure 3.6a). In order to avoid multiple coating/lithography/developing steps on the sample, pre-contact gold electrodes are patterned on an intrinsic Si substrate, with a 500-nm-thick thermal oxide layer, $SiO_2$, for further electrical contacting (see section 3.2.5). The resistivity of the intrinsic Si substrate is >8000 Ω.cm and the small residual doping is type $N$ due to phosphorus impurities. The hBN/graphene/hBN heterostructure is then transferred in the middle of the pre-contact pattern (Figure 3.6b).

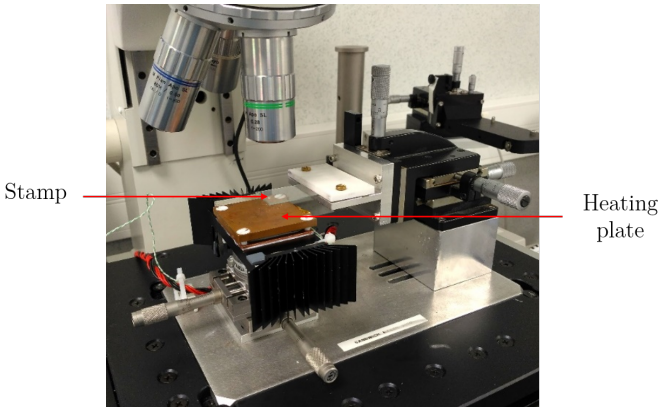


Figure 3.4: *Picture of the heterostructure assembly platform. The substrate with the 2D material we want to pick is put on the heating plate. The stamp is hold by a 3D micromanipulator, allowing an independent displacement with respect to the heating plate. The entire system is positioned on a microscope stage to drive the heterostructure assembly process.*

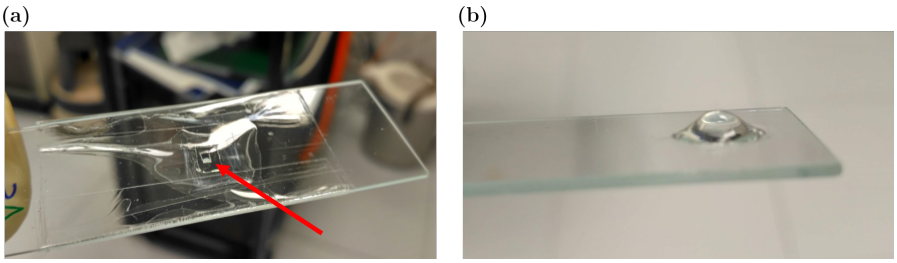


Figure 3.5: *Pictures of the stamp on a glass slide. (a) Initial cubic stamp geometry, pointed by a red arrow, based on reported methods [103]. (b) Stamp used in the present work to perform the heterostructure assembly, composed by an hemispherical PDMS structure covered by PPC.*

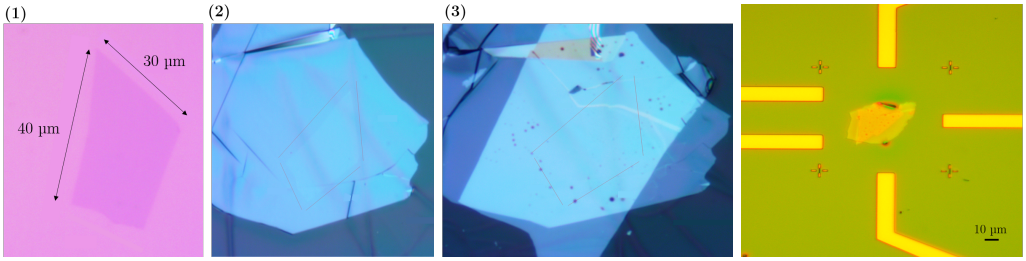


Figure 3.6: *(a):Optical images of the heterostructure assembly process: (1) graphene monolayer, (2) (top)graphene on (botom)hBN layer, (3) hBN(top)/graphene/hBN(bottom). Red lines in (2) and (3) outline the monolayer graphene (1) contour. (b): Optical image of an heterostructure assembly transferred onto a $SiO_2$ substrate. Prior to transfer, pre-contact gold lines are patterned for further electrical contacting.*

### 3.2.4 Electron beam lithography patterning

Using electron-beam lithography (EBL) followed by Reactive Ion Etching (RIE) on the hBN/graphene/hBN heterostructure, we define a GQD-based single electron transistor, as shown in Figure 3.7. It consists in a large central GQD linked to source and drain electrodes by two constrictions and surrounded by three lateral gates. As well as the GQD, all the electrodes and constrictions are made of hBN-encapsulated graphene.

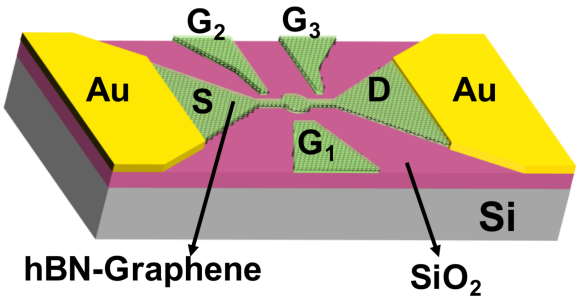


Figure 3.7: *Sketch of the devices made of an hBN/graphene/hBN heterostructure deposited on intrinsic silicon substrate with 500 nm thick $SiO_2$ on top. The central GQD is surrounded by three lateral gates $G_1$,$G_2$ and $G_3$ and linked to source $S$ and drain $D$ electrodes.*

As such fabrication procedure was not mastered, this has required several improvements, which have resulted in two generations of fabricated samples: A and B. A generation is defined by the method used to nanofabricate the GQD-based transistor. Based on the quality of the produced samples, together with transport characterization, the process and the structure design were improved, leading to the next generation.

#### First generation: batch A

As an initial approach, we start using a 150 nm thick positive Poly(methyl methacrylate) (PMMA) resist, spin coated on the $SiO_2$ substrate. The transistor architecture is patterned using EBL, followed after development by a 50 nm thick Aluminium (Al) deposit, which acts as a protecting mask during the etching step. A zigzag shape is drawn on the source/drain and gate electrode extremities in order to increase the electrical contact length during the connecting step (see section 3.2.5). The unprotected heterostructure area is finally etched out by a Fluoroform/Dioxygene ($CHF_3/O_2$)-based plasma etching, leaving only the transistor pattern. The Al mask is subsequently removed using caustic potash (KOH solution). Following this procedure, we produced two samples A1 and A2 with different designs detailed below.

For Sample A1, the GQD diameter is 600 nm and the constrictions width are 160 nm (see Figure 3.8 left). Unfortunately, it made the GQD structure more sensitive to impurities during the process: we can see traces of contaminants on the lower constriction, as well as between the two lateral gates on the right. Taking into account these drawbacks, we lowered the temperatures during the encapsulation process for Sample A2 to avoid contaminants and get a flat surface. We also reduced the GQD diameter to 270 nm, adjusted the constrictions width to 150 nm, increased space between gate electrodes and patterned a digit shape for its extremities (see Figure 3.8 right).

#### Second generation: Sample B

With the aim of reducing the number of fabrication steps, we turn to a negative resist for the EBL patterning, which act as a protecting layer during the plasma etching step. In

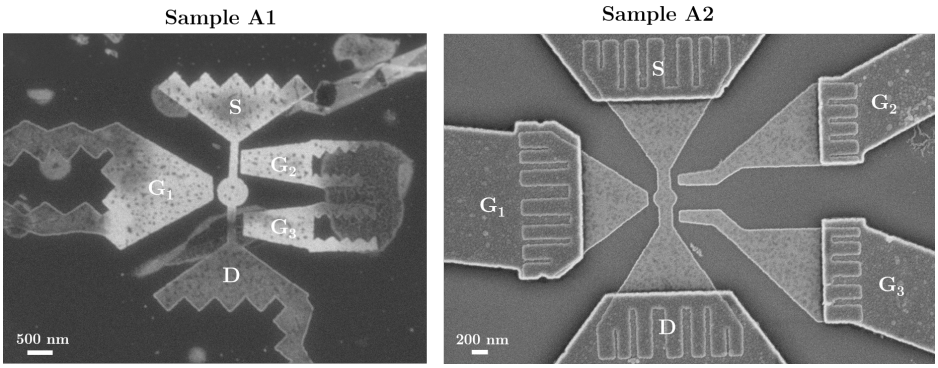


Figure 3.8: *Scanning electron microscopy (SEM) images of Sample A1 and A2, after the etching of the hBN-graphene-hBN heterostructure. The central GQD is surrounded by three portions of hBN-encapsulated graphene, which will play the role of lateral gates G and linked to S and D areas (which will act as source and drain electrodes after electrical connection). For Sample A2, a positive EBL that shape in the resist the electrical contact line has been performed.*

order to remove the electrostatic surface contaminants and get a uniform photoresist over the heterostructure surface, we first spin coat an adhesion promoter (Surpass 3000), followed by a Hydrogen silsesquioxane (HSQ) negative resist spincoating. As HSQ enables a higher resolution nanolithography, we subsequently reduce the GQD diameter. After EBL patterning and resist development, a RIE is performed, removing directly the unprotected heterostructure area.

In Figure 3.9, we present an example of GQD-based transistor produced following this procedure, denoted Sample B. It consists in a large central GQD, with a diameter of 150 nm, linked to source and drain electrodes by two short and narrow constrictions (40 nm). We see that the new protocol allows the realization of an homogeneous structure, with more precise contours, compared to Sample A1 and A2.

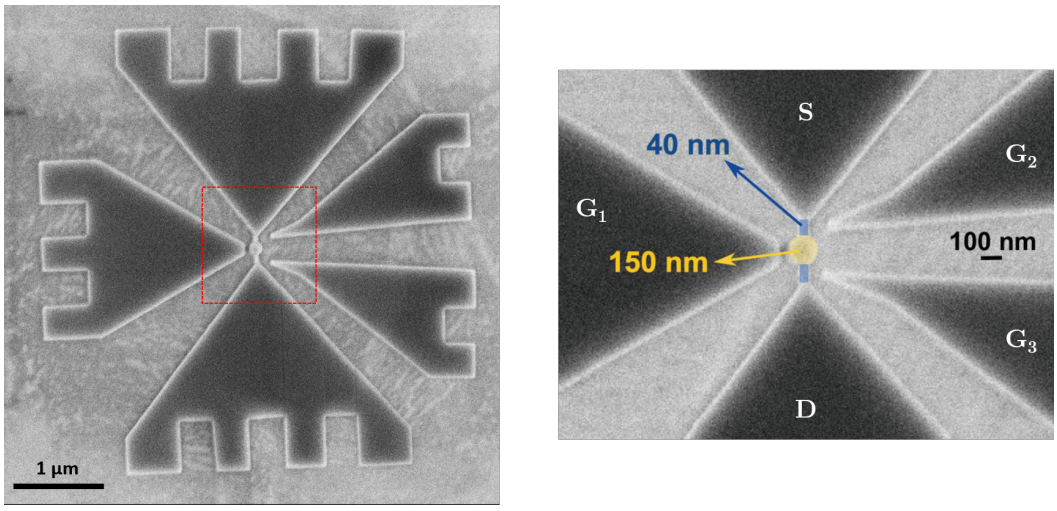


Figure 3.9: *SEM images of Sample B, after the etching of the hBN-graphene-hBN heterostructure at large (left) and reduced (right) scale. The central GQD of diameter 150 nm (yellow disc) is surrounded by three lateral gates G and linked to source S and drain D electrodes by two short and narrow constrictions highlighted in blue.*

### 3.2.5 Electrical contact

The last step consists in connecting source, drain and the three lateral gate electrodes to the surrounding pre-contact lines, using 1D edge-contact techniques [104]. A positive EBL is performed on the GQD-based device, using a 150 nm thick PMMA resist, followed after development by a 2/50 nm thick Chromium/Gold (Cr/au) deposit. The source and drain electrodes are patterned as a THz bow-tie antenna structure with the aim of enhancing the coupling between the single dot and an incident THz electric field for transport spectroscopy measurements under illumination. It can be shown that the bow antenna provides an electric field enhancement on the GQD of ∼4.

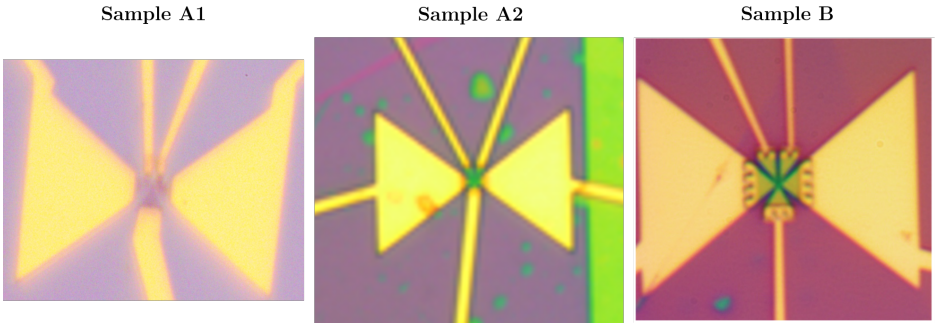


Figure 3.10: *Optical images of the connected devices A1, A2 and B with a* $\sim 20 \times 10$ *µm gold bow-tie antenna.*

From room-temperature DC current measurements, we confirm that the GQD-based samples A2 and B are electrically insulated from the $SiO_2$ substrate. Unfortunately, a short circuit was observed for Sample A1. We thus present in this work the transport spectroscopy measurements performed on Samples A2 and B.

In the transport experiments, we act on the two tunnelling barriers and on the GQD using respectively the three side gates $G_1$, $G_2$ and $G_3$, separated from the two constrictions and the GQD by a distance of ∼60-70 nm. The GQD is surrounded by the hBN layers (∼ 40 nm thickness), the $SiO_2$ oxide of the substrate (∼500 nm) and the vacuum. By neglecting the very thin hBN layers, we assume that the GQD is embedded in a medium with a dielectric constant $\varepsilon_{eff}$ that is calculated as the average between the underlying oxide constant and the vacuum constant $\varepsilon_{eff} = \frac{\varepsilon_{SiO2}+1}{2} \approx 2.5$.

## 3.3 Dark transport measurement

### 3.3.1 Transport spectroscopy principle

In this section, we start by describing the basic properties of electron transport in a quantum dot in Coulomb-blockade regime. We then present transport spectroscopy measurements performed on the GQD-based transistors Sample A2 and B, without external illumination[1].

#### Equivalent circuit diagram

A GQD-based transistor can be depicted by a simple circuit diagram, represented in Figure 3.11. The GQD is capacitively coupled to source and drain leads and to the plunger gate. The GQD can be represented by discrete energy levels, separated by $\delta E \sim meV$ for large

[1]Note that these experiments were carried out jointly with Elisa Riccardi, a postdoc in our team.

diameters, according to Chapter 1. The plunger gate G1 mainly operates via $V_g$ on the chemical potential of the quantum dot, with respect to the reservoirs chemical potential. The two side gates G2 and G3 control, through the two constrictions, the transport between the GQD and the source/drain electrodes that act as electron baths. The constrictions thus act as tunnelling barriers that isolate the GQD from the source and drain reservoirs, with tunnelling rates $\Gamma_{L,R}$ controlled by the side gate voltages $V_{g2} = V_L$ and $V_{g3} = V_R$. Because of Coulomb repulsion, the presence of an additional electron on the GQD will cost a charging energy $E_C$. The interplay between $\delta E$, $\Gamma$, $E_C$ and the thermal energy of the system $k_B T$ determine the transport regime and the conductance features, as function of the gate voltage $V_g$ and bias voltage $V_{SD}$. In this work, we set the different parameters of the system such as the transport is dominated by Coulomb repulsion between electrons, namely the Coulomb blockade regime:

$$\Gamma, k_B T \ll \delta E \leq E_C \tag{3.1}$$

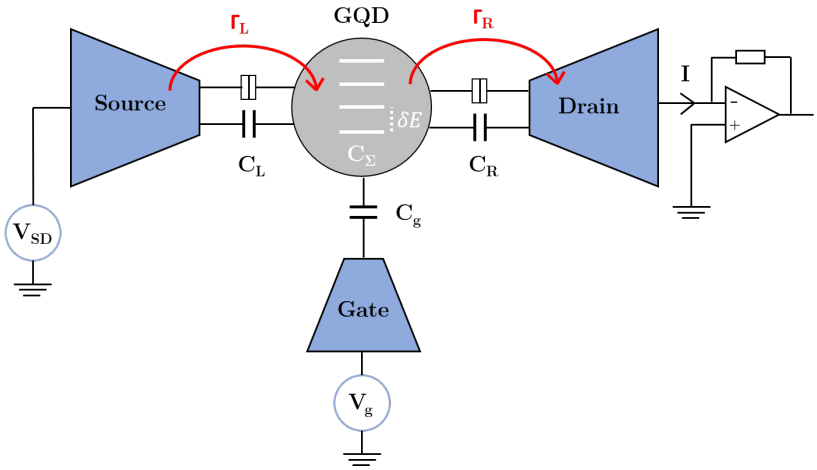


Figure 3.11: *Equivalent circuit diagram of a GQD-based transistor. The GQD (grey area) is described by discrete energy levels, separated by $\delta E$, and connected to source and drain electrodes. Left (L) and right (R) contacts are characterised by their tunnelling rate $\Gamma_{L/R}$ and capacitances $C_{L/R}$. A plunger gate is also capacitively coupled to the dot via a capacitance $C_g$. Transport spectroscopy measurements are performed by acting on $V_g$ and the bias voltage $V_{SD}$ while the current $I$ is amplified and acquired.*

### Coulomb blockade regime

Within this framework, the differential conductance $G = \frac{\partial I}{\partial V_{SD}}$ map in the $(V_g, V_{SD})$ plane, or charge stability diagram, shows diamond-shaped area of suppressed transport called Coulomb diamonds, where the charge number on the dot is fixed (see Figure 3.12). Each diamond corresponds to the N-electron ground state, and the relevant energy scales of the system can be extracted from their dimensions.

To this end, we use the constant interaction model [105] that is based on the two following assumptions. Firstly, the Coulomb interactions between an electron on dot and all the other electrons in the dot and its environment are constant and solely depend on the total capacitance of the dot $C_\Sigma = C_g + C_L + C_R$ where $C_g$ is the capacitance from the GQD to its local gate and $C_{L/R}$ the capacitance from the GQD to left/right leads. Secondly, the single-particle energy level spectrum $\epsilon_i$ is assumed to be independent of electron-electron interactions. The total energy $E(N)$ of the dot with N electrons in the ground state thus

writes [106]:

$$E(N) = \frac{e^2}{2C_\Sigma}\left(N - \frac{C_g V_g + C_L V_L + C_R V_R}{e}\right)^2 + \sum_{i=1}^{N} \epsilon_i \tag{3.2}$$

The energy difference caused by a tunnelling event is composed by two terms: the electrochemical potential $\mu(N+1)$ for adding ($-\mu(N)$ for extracting) one electron to (from) the dot, and the electrostatic energy $eV_i$ for adding ($-eV_i$ for extracting) an electron to (from) the electrode i, with $\mu(N)$ defined as:

$$\mu(N) = E(N) - E(N-1) \tag{3.3}$$

The N-electron ground state is stable if all four aforementioned single-electron transfer processes between the dot and the leads are forbidden, meaning they cost energy. This condition lead to the following set of inequalities, which define the Coulomb blockade regime:

$$\begin{aligned} &\text{left lead} \rightarrow \text{dot} : \mu(N+1) - eV_L > 0 \\ &\text{dot} \rightarrow \text{left lead} : -\mu(N) + eV_L > 0 \\ &\text{right lead} \rightarrow \text{dot} : \mu(N+1) - eV_R > 0 \\ &\text{dot} \rightarrow \text{right lead} : -\mu(N) + eV_R > 0 \end{aligned} \tag{3.4}$$

In our experimental conditions, we set $V_R = 0$ and thus $V_L = V_{SD}$. The conditions (3.4) result in:

$$\begin{aligned} eV_{SD} &< \left(N + \frac{1}{2}\right)\frac{e^2}{C_L} - \frac{C_g}{C_L}eV_g + \frac{C_\Sigma}{C_L}\epsilon_{N+1} \\ eV_{SD} &< -\left(N - \frac{1}{2}\right)\frac{e^2}{C_\Sigma - C_L} + \frac{C_g}{C_\Sigma - C_L}eV_g - \frac{C_\Sigma}{C_\Sigma - C_L}\epsilon_N \\ eV_{SD} &> \left(N - \frac{1}{2}\right)\frac{e^2}{C_L} - \frac{C_g}{C_L}eV_g + \frac{C_\Sigma}{C_L}\epsilon_N \\ eV_{SD} &> -\left(N + \frac{1}{2}\right)\frac{e^2}{C_\Sigma - C_L} + \frac{C_g}{C_\Sigma - C_L}eV_g - \frac{C_\Sigma}{C_\Sigma - C_L}\epsilon_{N+1} \end{aligned} \tag{3.5}$$

From (3.5), we can extract the diamond slopes, as depicted in Figure 3.12.

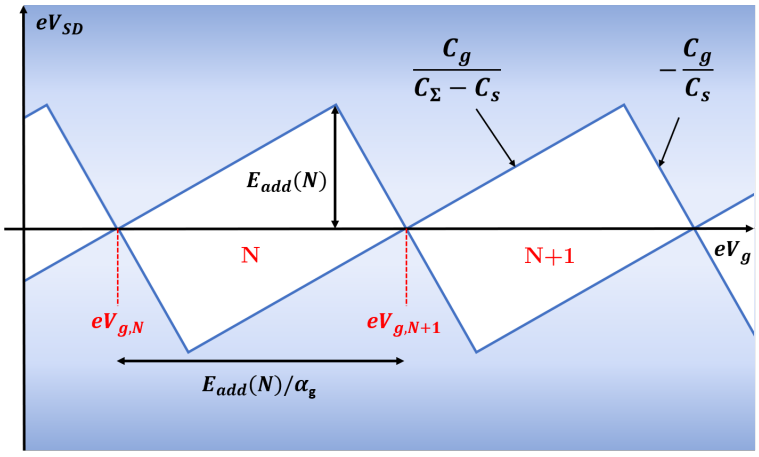


Figure 3.12: *Charge stability diagram of a quantum dot in the Coulomb blockade regime, depending on the gate voltage $V_g$ and bias $V_{SD}$. The blue shaded areas denote the $(V_g, V_{SD})$ region where a current flows through the dot. In white areas, the electron transport is suppressed and the number of electrons $N$ on the dot is fixed.*

The addition energy $E_{add}(N)$ is defined as the energy required to add a $(N+1)^{th}$ electron on the quantum dot:

$$E_{add}(N) = \mu(N+1) - \mu(N) = \frac{e^2}{C_\Sigma} + \epsilon_{N+1} - \epsilon_N = E_C + \delta E(N) \tag{3.6}$$

where $E_C = \frac{e^2}{C_\Sigma}$ is the charging energy and $\delta E(N) = \epsilon_{N+1} - \epsilon_N \simeq \delta E$ the interlevel energy spacing, assumed to be independent of N. The gate voltage $V_{g,N}$ is defined as the zero-bias degeneracy condition between the N-1 and N-electron ground states, that is $\mu(N, V_{g,N}, V_{SD} = 0) = 0$. For each $V_{g,N}$ there is a conductance peak: the difference $e(V_{g,N+1} - V_{g,N})$ corresponds to the distance between consecutive peaks and thus to the zero-bias diamond width. Using Equations (3.2), (3.3) and (3.6), the addition energy in the N-electron state can be extracted from the zero-bias diamond width, as:

$$e(V_{g,N+1} - V_{g,N}) = \frac{E_{add}(N)}{\alpha_g} \tag{3.7}$$

with $\alpha_g = C_g/C_\Sigma$ the gate capacitive lever arm. Additionally, the diamond half-height is found to be equal to $E_{add}(N)$.

**Charge stability diagram description**

Let us now describe the different configurations of the GQD-based transistor, when varying the control knobs $(V_g, V_{SD})$ (Figure 3.13) . At zero-bias voltage $V_{SD} = 0$, the source and drain electrochemical potentials are aligned: $\mu_S = \mu_D$. The gate voltage $V_g$ tunes the electrochemical potential of the dot and a tunnelling transport occurs only if an empty single-energy level of the dot crosses $\mu_{S/D}$. By increasing $V_{SD}$ such as $\delta E \leq eV_{SD} < E_{add}$, it is possible that empty ground and excited states are within the transport windows. Electrons can sequentially tunnel through the dot via these states, resulting in lines of locally enhanced current. If the bias equals the addition energy $V_{SD} = E_{add}$, at least one state is within the transport window and a current can flow through the dot. The Coulomb blockade starts to be completely lifted when $V_{SD} > E_{add}$.
For all the experimental differential conductance maps presented in this chapter, we directly take into account the charge factor for the different voltages: $V_{SD,g} \equiv eV_{SD,g}$.

### 3.3.2 Sample A2

To perform transport measurements, the GQD-based device is placed within a dilution $^4$He-$^3$He cryostat. For Sample A2, we use a cryostat without optical access. The device is cooled down to a temperature of 300 mK. The Coulomb stability diagram of Sample A2, i.e. plots of the differential conductance $G = \frac{\partial I}{\partial V_{SD}}$ as function of $V_{DS}$ and $V_g$, is reported in Figure 3.14a. We observe the presence of numerous Coulomb diamonds over a wide range of $V_g$, thus confirming that the GQD-based transistor is in the Coulomb blockade regime. In specific area of the stability diagram, Coulomb-blockade peaks are observed in the differential conductance as a function of the plunger gate voltage $V_g$, showing a regime of sequential single-electron tunnelling (see Figure 3.14b).

However, we notice that for $V_g \leq 0.43\ V$, successive Coulomb diamonds overlap with each other and exhibit not clearly defined contours. As the diamond width is equal to $E_{add}(N)/\alpha_g$, this behavior might come from a variation of the addition energy as the dot is filled with electrons or from capacitance fluctuations probably arising from the too large constrictions of Sample A2 (see SEM image 3.8). Moreover, we do not observe any excited states through additional lines parallel to the edges of the Coulomb diamond.

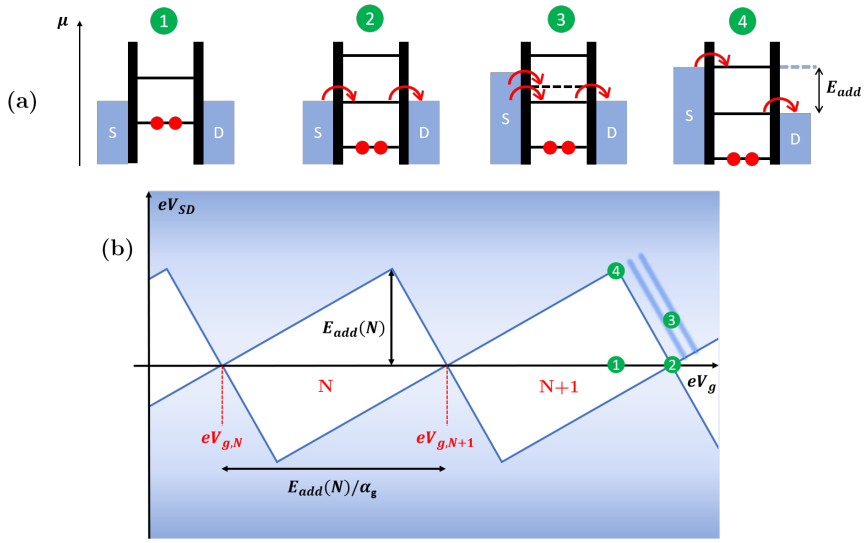


Figure 3.13: *Scheme of four different configurations of the GQD (a) corresponding to different points in the stability diagram (b). Red arrows indicate an electron flux. (1)-(2) When source and drain electrochemical potentials are aligned ($V_{SD} = 0$), a tunnelling transport occurs only if an empty single-energy level crosses $\mu_{S/D}$. (3) Different transport channels lie within the transport window $\mu_S - \mu_D$, resulting in lines of enhanced current (4) The bias equals to the addition energy.*

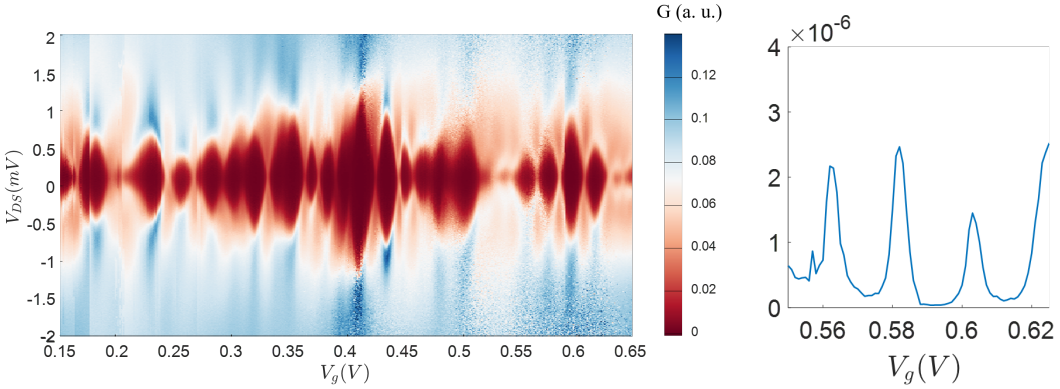


Figure 3.14: *a) Differential conductance G of Sample A2 as function of the source-drain voltage $V_{DS}$ and of the plunger gate voltage $V_g$, exhibiting Coulomb diamonds. b) Differential conductance taken in narrow area of the stability diagram. The two side gates are at $V_{g2} = 1.9$ V and $V_{g3} = 0.2$ V.*

In conclusion of the section, the transport spectroscopy measurements performed on Sample A2 have revealed Coulomb blockade regime in a hBN/graphene/hBN quantum dot heterostructure, with electrodes and constrictions also made of hBN-encapsulated graphene, validating our fabrication process. However, the too large constrictions and the non-negligible capacitive coupling between the different side gates have prevented from a fine analysis of the quantum transport in the sample A2. Process fabrication optimisations have been done to overcome these issues for Sample B. Owing to a different approach for the EBL patterning, the constriction widths have been reduced to $\sim 40$ *nm* as well as the GQD diameter $D = 140$ *nm*. The side gates have been moved away from each other to avoid parasitic coupling, with a reduced width on the vicinity of the quantum dot.

### 3.3.3 Sample B

In this section we present the experimental results obtained with Sample B. The GQD-based device is placed within another dilution $^4$He-$^3$He cryostat, which possesses optical access. We first perform transport measurements with the fridge's window closed to explore the electron confinement and excitation spectrum of the GQD. The device is cooled down to a temperature of 170 mK.

#### Transport spectroscopy

The Coulomb stability diagram of Sample B is reported in Figure 3.15. We observe well-defined and stable Coulomb diamonds, which correspond to the ground state of the GQD. The conductance map is not centered at $V_{DS} = 0$ V due to the offset voltage of the preamplifier on the drain $V_0 = -0.35$ mV. Consequently, the source-drain voltage applied to the GQD is $V^*_{DS} = V_{DS} - V_0$. As observed in Figure 3.16(a), pronounced Coulomb-blockade peaks are observed in the differential conductance as a function of the plunger gate voltage $V_g$, showing the regime of sequential tunnelling where the transport is allowed only if the chemical potential of the source (or drain) crosses one empty level of the quantum dot. In addition, the standard deviation of the normalized peak spacing distribution is found to be $\sim 0.099$, which is 45% and 15% better than a GQD on $SiO_2$ and on bottom hBN, respectively [100]. This result thus confirms that a full hBN encapsulation allows to reduce disorder of the GQD.

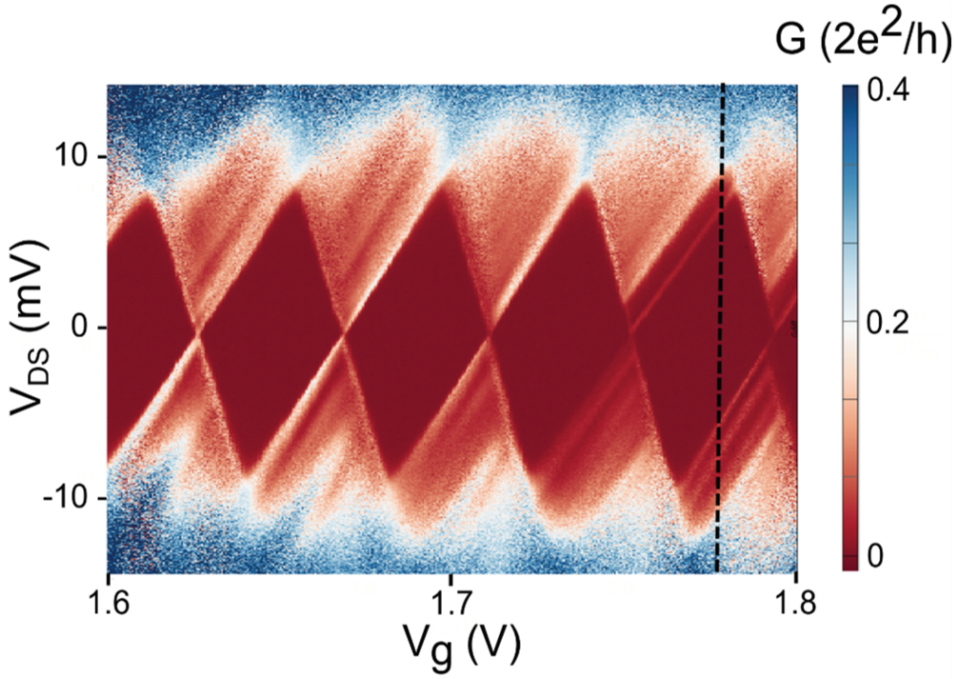


Figure 3.15: *Differential conductance G of Sample B as function of the source-drain voltage $V_{DS}$ and of the plunger gate voltage $V_g$, exhibiting pronounced Coulomb diamonds.*

We also observe quantum confinement effects as lines parallel to the edges of the diamonds in Figure 3.15. The lines evidence the sequential tunnelling of the electrons via the excited states of the GQD. From the vertical cut of the conductance map shown in Figure 3.16(b), we clearly see resonances due to the tunnelling through the excited states around a region where conductance is strongly suppressed. The energy separation of the excited states gives the single particle level spacing of the GQD, $\delta E = 1.7$ meV, corresponding to a frequency

spacing of 0.42 THz. This result confirms that large GQDs (of diameter 150 nm) provide discretization of electronic states with energy spacing in the meV range (i.e THz range). The full-width at half-maximum of the excited state resonance at $V_g = -5$V is 0.48 meV corresponding to a thermal broadening of $T = 1.8$ K that is roughly consistent with the expected electronic temperature in the GQD under bias.

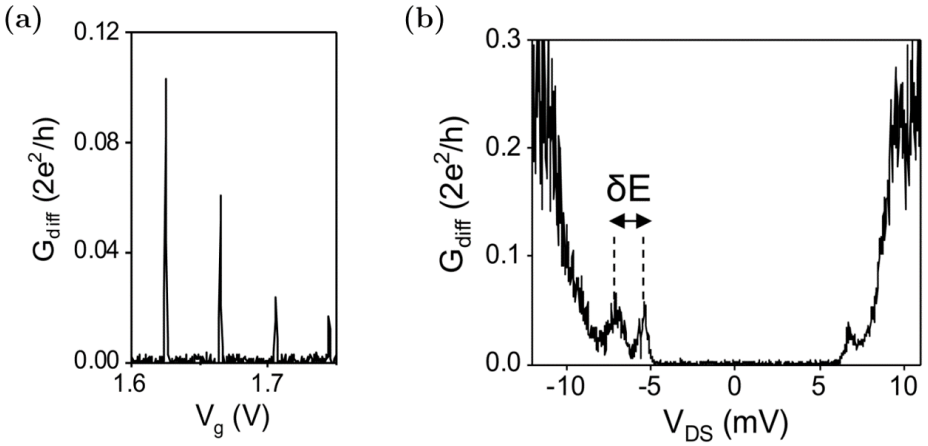


Figure 3.16: *(a) Differential conductance as function of $V_g$ at $V_{DS} = 0$ mV. The two side gates are at $V_{g2} = V_{g3} = 11.5$ V. (b) Differential conductance as function of $V_{DS}$ (vertical cut along the dark dashed line in Figure 3.15. The width of the diamond allows to estimate the addition energy, while the slope of the diamond edge is proportional to the electronic temperature.*

From the half-height of Coulomb diamond, we extract the addition energy $E_{add} = 9$ meV. From $E_{add}$ and $\delta E$, we deduce a charging energy $E_c = E_{add} - \delta E = 7.3$ meV, which is smaller than the charging energy estimated from a metallic disk model $E_c = e^2/C_\Sigma = 12$ meV, with $C_\Sigma = (4\epsilon_0\epsilon_{eff}d)$. We note that this deviation corresponds to an increase of the total disk self capacitance $C_\Sigma$ by a factor $\sim 1.6$. It might indicate that the full hBN encapsulation allows to reduce the capacitive coupling of the GQD to the adjacent gate and leads.

According to the evolution of the single particle level spacing with the GQD diameter developed in Chapter 1, the order of magnitude of $\delta E$ is consistent with a 150 nm diameter GQD. Further study related on the nature of the probed excited states is under investigation [107, 108] .

## 3.4 Transport measurement under THz illumination

We now turn to the transport investigation of the GQD-based device (sample B) under THz light illumination. Figure 3.17 represents a schematic view of the experimental setup[2]. The THz optical access of the fridge is composed by three sapphire windows. The THz light source is a high-pressure mercury plasma arc-discharge lamp. The blackbody radiation emitted by the source is incoherent; it is filtered above 10 THz with a low pass filter so that the incident THz photon energies $\hbar\omega$ are lower than 20 meV. To focus the THz beam onto the GQD-based device, a pair of parabolic mirrors are placed in front of the fridge window. The incoherent incident radiation is mechanically modulated at a frequency of 330 Hz and we record the DC current with and without illumination (i.e. the mean value of the modulated current) and also the photocurrent, $I_{photo}$, using a lock-in amplifier. For optical

[2]Note that these experiments were carried out jointly with Elisa Riccardi, a postdoc in our team.

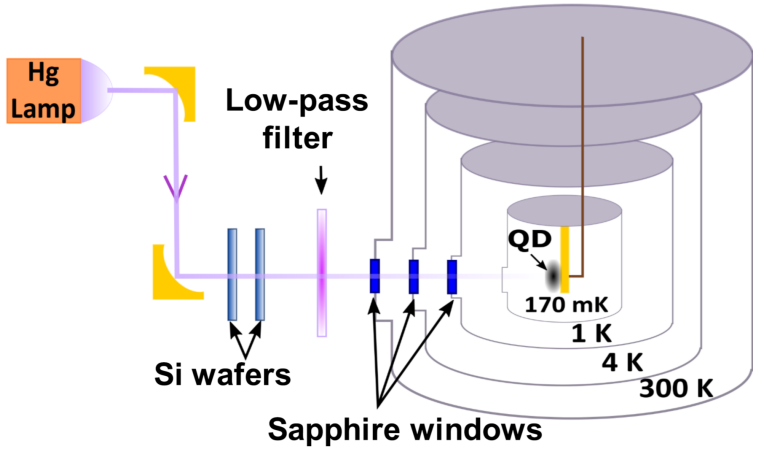


Figure 3.17: *Sketch of the experimental setup: the GQD-based sample B is placed within a dilution cryostat at 170 mK equipped with three sapphire windows. The incoherent THz radiation emitted by a Hg lamp, filtered using a low pass filter to frequencies < 10 THz, is focused on the GQD-based sample. Some high-resistivity silicon wafers are used to attenuate the incident THz radiation.*

power-dependence measurements, we insert Si wafers in the THz beam path to attenuate the incident THz power. Without any Si wafer, the estimated THz optical power of the incident THz radiation onto the GQD-based device is ∼10 pW.

### 3.4.1 DC current response

We first focus on the effect of the THz illumination on the current flowing through the GQD at fixed $V_{DS}$. Figures 3.18 (a) and (b) show Coulomb blockade peaks in the DC current measured as a function of $V_g$ with ($I_{on}$, red line) and without ($I_{off}$, black line) illumination for $P_0 = 10\ pW$, $V_{DS} = 2$ meV and $V_{DS} = -2$ meV, respectively. The magnitude of the Coulomb blockade peaks reach a few nA. Note that the Coulomb peaks are significantly broadened when opening the fridge's window even without THz illumination. This broadening may be due to the sensitivity of the GQD-based device to the electromagnetic environment.

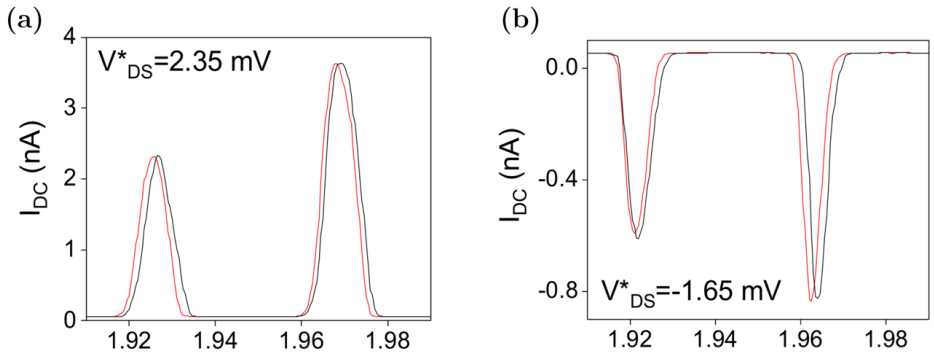


Figure 3.18: *(a) DC current Coulomb peaks as a function of $V_g$ at $V^*_{DS} = 2.35\ mV$ (a) and $V^*_{DS} = -1.65\ mV$ (b) with (red) and without (black) THz illumination. We defined $V^*_{DS}$ as the source-drain voltage applied to the GQD after subtracting the preamplifier offset voltage $V_0 = -0.35\ mV$.*

We observe that the magnitude and the shape of the Coulomb current peaks are not affected by the incoming THz photons. However, the current peaks are shifted to lower $V_g$ when the THz radiation is switched on. The shift, $\delta V_g$, is about ∼1 mV and gives rise to a difference $I_{on} - I_{off}$ in the nA range, as shown in 3.19 (a) and (b). The $I_{on} - I_{off}$ traces show consistently a bipolar behavior with a positive and a negative peak as a result of the peak current

shift to lower $V_g$.

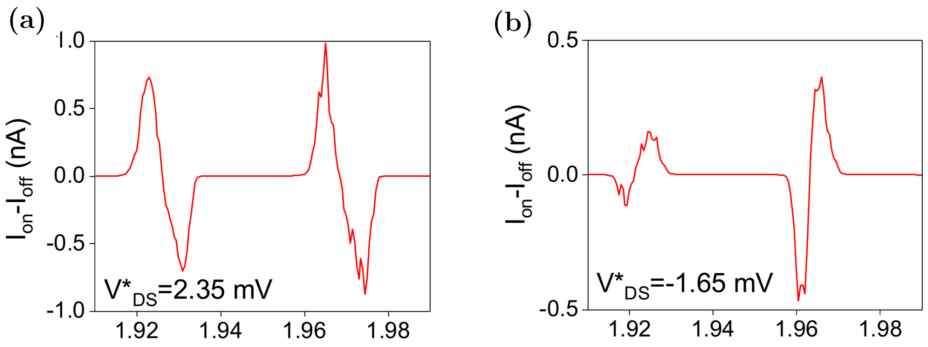


Figure 3.19: *The difference $I_{on} - I_{off}$ as a function of $V_g$ at $V^*_{DS} = 2.35$ mV (a) and $V^*_{DS} = -1.65$ mV (b).*

In order to get a more quantitative insight in the detection process of the incoming THz photons, we calculate the net current through left and right leads assuming that $\Gamma_R, \Gamma_L < k_B T$ with $\Gamma_R, \Gamma_L$ representing the tunnelling rate between the quantum dot and the left and right leads respectively. Using the probabilistic master equations in the stationary regime [106], the current $I$ without illumination is expressed as:

$$I = -eA[f_{FD}(\alpha_1 V_g - eV^*_{DS}) - f_{FD}(\alpha_2 V_g - eV^*_{DS})] \tag{3.8}$$

with $A = \frac{\Gamma_L \Gamma_R}{\Gamma_L + \Gamma_R}$, $\alpha_1 = \frac{C_g}{C_\Sigma - C_L}$, $\alpha_2 = -\frac{C_g}{C_L}$, using capacitance definitions of section 3.3.1 and $f_{FD}(E) = \frac{1}{e^{E/(k_B T_e)}+1}$ the Fermi-Dirac distribution. As described in section 3.3.1, we extract the variables $\alpha_1 = 0.89$ and $\alpha_2 = 0.85$ from the Coulomb diamond slopes obtained with a closed window (Figure 3.15). If we select the dark current peaks around $V_g = 1.97$ V at $V_{DS} = 1$ meV and $V_{DS} = 3$ meV, we see that the experimental DC current curves without THz illumination (black symbols) are well reproduced using equation (3.8) for $T_e = 10$ K (black lines), as shown in Fig. 3.20(a) and (b). The parameter $A$ only is adjusted between $V_{DS} = 1$ meV and $V_{DS} = 3$ meV since the tunneling rates depend on $V_{DS}$. The good agreement between theoretical curves and measured dark DC current validate our description of the current flow through the GQD.

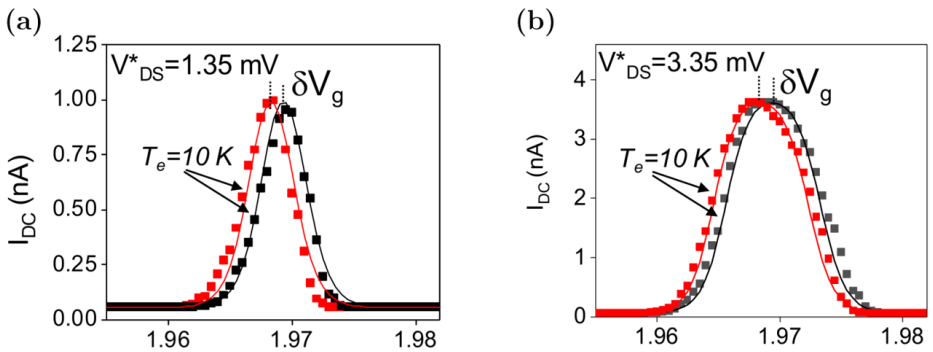


Figure 3.20: *DC current Coulomb peaks around $V_g = 1.97$ V at $V^*_{DS} = 1.35$ mV (a) and $V^*_{DS} = 3.35$ mV (b) with (red) and without (black) THz illumination. Data are reported by diamond symbols, and theoretical fits using equation* (3.8) *are represented by plain lines.*

Additionally, by replacing $V_g$ with $V_g - \delta V_g$ in equation (3.8), the experimental DC current peaks under THz light illumination (red symbols) are also remarkably well fitted (red lines)

without changing any other parameters (see Fig. 3.20(a) and (b)). This indicates that $\delta V_g$ is independent of $V_{DS}$. Moreover, $T_e$ is kept constant with and without illumination, pointing out the fact that the electronic temperature in the GQD is not significantly changed by the incoming THz photons, in contrast with previous works on GQD illuminated by THz photons [98]. This analysis confirms that the THz detection process is fully described by an additional gate voltage $\delta V_g$. Furthermore, using expression 3.3 at fixed $V_{DS}$ and fixed number of electrons:

$$\mu(N) = \frac{e^2}{C_\Sigma}\left(N - \frac{1}{2}\right) - e\alpha_g V_g - e\frac{C_L}{C_\Sigma}V_{DS} + \epsilon_N \tag{3.9}$$

we understand that the additional gate voltage $\delta V_g$ results in a reduction of the GQD electrochemical potential $\mu_{dot}$ with respect to those of the leads.

### 3.4.2 Photocurrent

We further investigate the photoresponse of the GQD-based device as a function of both $V_{DS}$ and $V_g$ reported as a $I_{photo}$ map in Fig. 3.21(b), for an incident THz power $P_0 = 10$ pW. For comparison, we also report in Fig. 3.21(a) the differential conductance stability diagram measured without THz illumination but with fridge's window open.

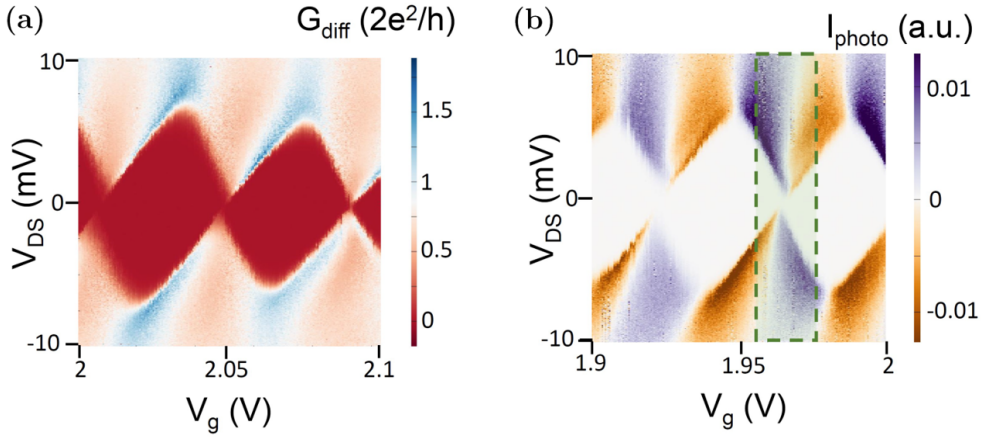


Figure 3.21: *(a) Dark differential conductance G as a function of $V_{DS}$ and $V_g$ with fridge's window open. (b) Map of $I_{photo}$ as a function of $V_{DS}$ and $V_g$.*

We note that the Coulomb diamonds of the dark differential conductance are smaller than those with the window closed (Fig. 3.15), which may be due to the sensitivity of the addition energy and also the capacitance of the GQD-based device to the electromagnetic environment. The dark differential conductance and $I_{photo}$ maps show very similar features such as common diamond-shaped structures. In addition, the absence of any additional photocurrent lines induced by THz light into or out of the Coulomb blockaded regions on Figure2b suggests that any intersublevel transition in the GQD or any photon-assisted tunnelling effect (electrons exchange photons in the quantum dot) are driven by the incident photons. We attribute this absence to the incoherence of the incident THz radiation. The bipolar features observed only in the $I_{photo}$ map, emphasized by the positive and negative slopes of the Coulomb diamonds edges, point out significant modification of the resonance conditions induced by THz illumination for charging and discharging the GQD to the respective leads. Regarding our previous analysis on the DC current response, the photocurrent $I_{photo}$ map thus reflects the tuning $\Delta\mu_{dot}$, induced by THz light illumination, of the chemical potential in the GQD, $\mu_{dot}$, with respect to those of the leads.

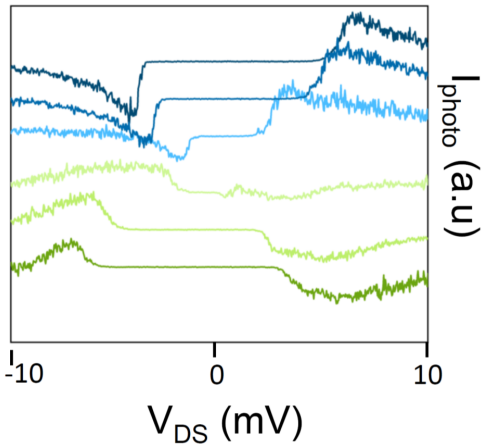


Figure 3.22: *Vertical cuts of $I_{photo}$ taken in the dashed box of the photocurrent map (b). The spectra, as a function of $V_{DS}$, exhibit a change in sign when the sign of $V_{DS}$ is changed, and this trend is inverted when the system pass from the left side (green) to the right side (blue) of the Coulomb diamonds.*

In order to illustrate this effect, we also plot few $I_{photo}$ profiles in the axis of $V_{DS}$, taken from the dashed box of the photocurrent map (Figure 3.22). The spectra, as a function of $V_{DS}$, exhibit a change in sign when the sign of $V_{DS}$ is changed and this trend is inverted when the system pass from the left side (green) to the right side (blue) of the Coulomb diamonds. We attribute the asymmetry of $I_{photo}$ with respect to $V_{DS}^{*}$ to different capacitances from the GQD to the left and right leads. We note that no distortion of the Coulomb diamonds is observed in the $I_{photo}$ map, thus indicating that the chemical potential shift $\Delta\mu_{dot}$ is independent of $V_g$ and $V_{DS}$, i.e., that is constant over the whole charge stability diagram. Using the lever arm of 0.15 extracted from the dark differential conductance map with open fridge window, we deduce that a $\delta V_g$ of $1 \pm 0.2$ mV corresponds to a $\Delta\mu_{dot}$ of $\sim 0.15 \pm 0.03$ meV. Thus, illuminating the GQD-based device with incoherent THz photons results in a renormalization of the chemical potential of the GQD $\Delta\mu_{dot} \sim 0.15 \pm 0.03$ meV. This very low-energy physical effect is clearly observable here owing to the extremely high-energy resolution provided by the low temperature experiment.

### 3.4.3 GQD chemical potential renormalization

Let us now discuss the physical mechanism responsible for the renormalization of the chemical potential of the GQD. THz photons, incoming from the incoherent and broadband source, are absorbed by both the whole graphene area (including the quantum dot, the leads and gate electrodes that are made in encapsulated graphene) and by the silicon substrate. Let us first consider if the absorption of THz radiation by the graphene area could be responsible for the $\mu_{dot}$ renormalization.

#### Graphene THz absorption

THz photons are preferentially coupled to the leads due to their larger size and their linear dispersion relation (in contrast to the quantum dot) that provides stronger absorption of the broad THz radiation. At these frequencies the absorbed energy results in an increase of the electronic temperature and consequently, the chemical potentials of the graphene leads are reduced [51]. The observed gate renormalization in the stability diagram could then reflect a relative shift between the quantum dot discrete levels and the chemical potential

of the graphene leads (see Figure 3.23). Since the absorption process in the graphene leads

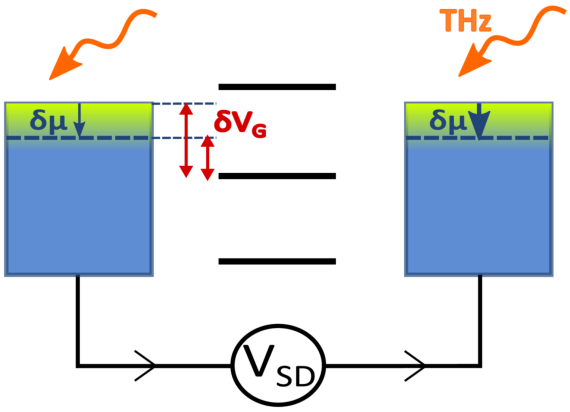


Figure 3.23: *Sketch of the energy renormalization due to the incident THz field. The chemical potential renormalization $\delta\mu$ of the electron baths results in a shift of the gate voltage $\delta V_g$.*

relies only on intraband transitions ($\hbar\omega < 2\mu_{S,D}$), it conserves the total carrier density $N$, expressed as:

$$N_{S,D} = \int_{\infty}^{0} D(E)\left[f_{FD}(E-\mu_{S,D}) - f_{FD}(E+\mu_{S,D})\right] dE \tag{3.10}$$

with $D(E) = 2|E|/(\pi(\hbar v_F)^2)$ the density of states of graphene [70]. Such intraband absorption results in an energy transfer to the thermalized electron population in the leads. Owing to the ultrafast electronic thermalization in graphene, this excess energy raises the electronic temperature in the leads spreading their Fermi-Dirac distribution [51]. This effect is balanced by a decrease of the chemical potential of the leads to verify $N_{S,D}$ conservation[57], resulting in a renormalization of the chemical potential in the GQD with respect to those of the leads. Quantitatively, the chemical potential in the leads is expressed by the implicit function:

$$\frac{1}{2}\frac{T_F}{T_e} = F_1\left(\frac{\mu_{S,D}}{k_B T_e}\right) - F_1\left(-\frac{\mu_{S,D}}{k_B T_e}\right) \tag{3.11}$$

with $F_1(x) = \int_0^{\infty} \frac{t}{1+e^{t-x}} dt$, $T_F = E_F/k_B$ and $E_F$ the Fermi level.

In the limit of low temperature $T << k_B\mu(0)$, it exists an analytical solution for the chemical potential renormalization:

$$\mu(T) = \mu(0)\left(\frac{\pi^2}{6}\frac{k_B^2 T^2}{\mu(0)^2}\right) \tag{3.12}$$

In Figure 3.24, we trace the $\mu$ renormalization in the function of the temperature increase. We perform the same plot for different values of Fermi energy (10, 25, 100 meV).
Even if the $\mu$ renormalization depends on the Fermi level position, we cannot obtain an energy shift of 0.15 meV without a significant temperature increase. As shown in Figure 3.24, we estimate from (3.12) that a renormalization of the chemical potential in the GQD $\Delta\mu_{dot} = 0.15meV$ corresponds to an increase of the electronic temperature $\Delta T_e > 17$ K.
However, our data are qualitatively and quantitatively inconsistent with such temperature increase. Indeed, the current peaks with and without illumination are well reproduced using equation (3.8) for a constant temperature $T_e = 10$ K. Increasing $T_e$ up to >17 K would significantly broaden the current peak under THz illumination. Moreover, by resolving the heat flow using the Wiedemann-Franz law, Simon Messelot, a PhD of our research team, has estimated a $\Delta T_e$ lower than 0.2 K in our experimental condition. Consequently, even if a renormalization of the GQD chemical potential is expected from the absorption of the THz

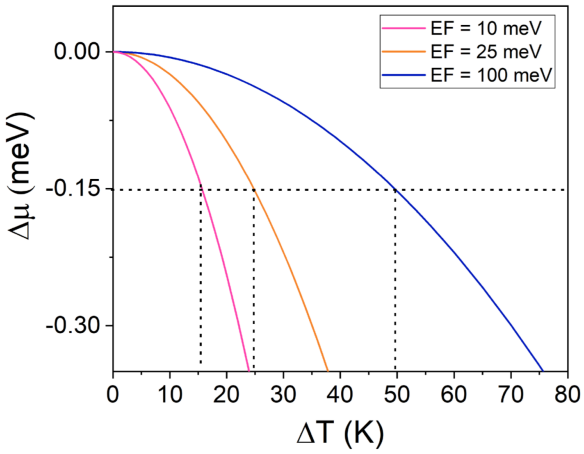


Figure 3.24: *Chemical potential renormalization as function of the temperature rise for different values of Fermi Energy. In all cases, to obtain a $\delta\mu$ of 0.15 meV, we need a rise in temperature between 15 and 50 K.*

photons by the graphene leads, its magnitude would be significantly lower than 0.15 meV and thus could not account for the large photocurrent response of the GQD-based device.

### Photogating effect

Another effect that can be pointed out is the photogating effect [109, 110]. It relies on the absorption of THz photons in the silicon substrate. Absorption of typically $0.2 - 0.4$ cm$^{-1}$ in the THz spectral range have been recorded in high-resistivity silicon due to shallow impurity absorption (since silicon bandgap energy is high compared to the THz photon energy) [111, 112, 113]. This absorption process creates photoexcited carriers in silicon from the ground states of impurities into the valence and conduction bands [114]. This is in contrast with free carrier absorption that does not create free carriers and is extremely low in high-resistivity silicon ($\alpha_{Drude} = 0.011 cm^{-1}$ due to the low free carrier concentration, $n = 10^{11} cm^{-3}$). The photogating effect relies also on the existence of a band bending at the $SiO_2$/Si interface due to charges in the oxide (fixed-oxide charge, oxide-trapped charge and mobile ionic charge) and traps at the interface (interface-trapped charge) [115].

In our case of the silicon substrate with residual N-type doping, the energy bands in silicon bend upward, leading to a triangular potential well for the holes at the interface and a built-in electric field near the interface. The electric field can separate the photoexcited carriers absorbed in silicon, electrons diffuse toward the bulk silicon, and holes accumulate at the interface[116, 117]. Holes are moreover trapped in the potential well. This accumulation of photon-generated holes at the $SiO_2$/Si interface provides an additional positive gate voltage by capacitive coupling. In other words, the photogating effect would cause a negative shift in the $I_{DS}$-$V_G$ characteristic under laser illumination. This interfacial photogating effect is qualitatively fully consistent with our observations. Indeed, we observe a negative shift of the $I_{DS}$-$V_G$ characteristic under THz illumination, independent of $V_{DS}$ and $V_G$, remembering that the photocurrent is the difference between the source-drain currents in dark and illumination regime.

Several other mechanisms can be responsible for the conversion of absorbed THz photons into a photocurrent in graphene-based devices such as the photovoltaic effect, the photothermoelectric effect and the bolometric effect [118]. However, all these mechanisms generate

photocurrents or photovoltages without any shift in gate voltage. Moreover, photothermoelectric and bolometric effects rely on an increase of the electronic temperature that is extremely weak in this work due to the low incident power as discussed previously. Consequently, we attribute the photocurrent originating from the gate voltage shift measured when the GQD-based device is illuminated by THz photons to the interfacial photogating effect. Since the Coulomb blockade current at low temperature is extremely sensitive to the gate voltage, the GQD acts as a very sensitive electrometer operating in the THz spectral range.

### 3.4.4 THz power influence on the photoresponse

To further investigate the properties of the THz photoresponse, we measure $I_{photo}$ and $\Delta\mu_{dot}$ as a function of $P_0$, as displayed in Figure 3.25. The same set of measurements is repeated at several positions of the Coulomb diamonds map, i.e., for 4 different values of $V_g$.

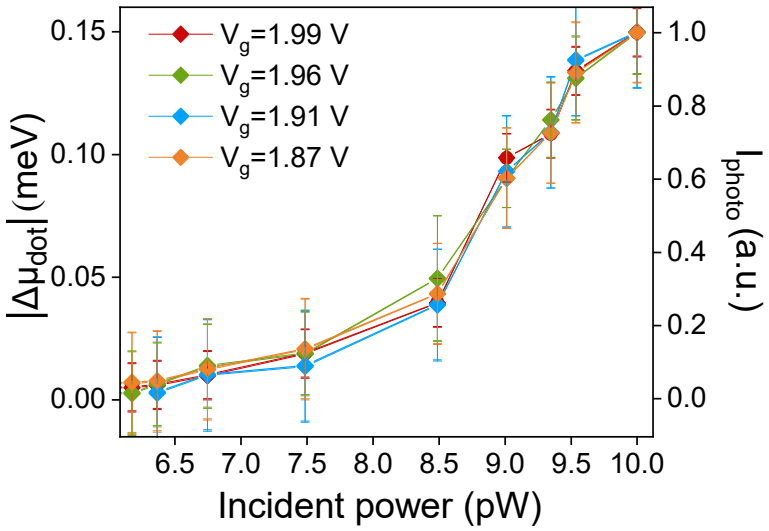


Figure 3.25: *$|\Delta\mu_{dot}|$ and $I_{photo}$ as a function of the incident power $P_0$ onto the GQD-based device for $V_{DS} = 2$ mV and $V_g = 1.99$ V; $V_g = 1.96$ V,$V_g = 1.91$ V and $V_g = 1.87$ V.*

We observe that $I_{photo}$ and $|\Delta\mu_{dot}|$ increase monotonously as $P_0$ is increasing with a nonlinear dependence. $I_{photo}$ and $|\Delta\mu_{dot}|$ also start to saturate at high power. We found a very robust nonlinear dependency between $\Delta\mu$, $I_{photo}$ and the incident power for all $V_g$. These tendencies are not compatible with a $\Delta\mu_{dot}$ induced by the intraband absorption of the THz photons in the graphene leads since, at such low incident THz electric field and low temperature [57], as $\Delta\mu_{dot} \propto T_e^2$ according to (3.12) and $T_e^2 \propto P_0$, $\Delta\mu_{dot}$ is expected to evolve linearly with $P_0$. On the contrary, both the nonlinearity and saturation features are consistent with interfacial photogating effect. Indeed, as trapped photocarrier lifetime in silicon depends on the incident optical power [119], the photoexcited carrier density in the steady-state regime contributing to the photogating effect is expected to evolve nonlinearly with $P_0$. The observed saturation can be attributed to a decrease of the height of the potential well at the $SiO_2$/Si interface as the THz incident power is increased. This feature has been observed in several previous works in graphene-based photodetectors dominated by the photogating effect [120] and attributed to the trapped charges at the interface that induce an opposite build-in electric field. Thus, these power-resolved measurements provide an additional evidence that interfacial photogating is the main physical mechanism involved in the THz photoresponse of the GQD-based device.

### 3.4.5 Conclusion and perspectives

In conclusion, we have investigated the electronic transport properties in hBN-encapsulated GQD based devices in Coulomb blockade regime at low temperature. The transport measurements on the first sample have shown Coulomb blockage regime in the fully encapsulated graphene quantum dot transistor structure. From transport measurements on the second generation of sample, we have shown that the full hBN encapsulation allows to reduce the disorder potential in the GQD, thus enabling the measurement of very stable and well-defined Coulomb-diamonds, with a lowered standard deviation characteristics. It additionally allowed the direct observation of the GQD excited states of energy $\sim 1.7$ meV (i.e. 0.4 THz) by low-temperature transport experiments.

Moreover, we have uniquely investigated the photoresponse of GQD in Coulomb blockade regime under incoherent THz illumination. We have demonstrated a large photocurrent, in the nA range, originating from a renormalization of the chemical potential of the GQD with respect to those of the leads. We have shown that this effect evolves nonlinearly with the incident power and attribute it to interfacial photogating effect. Besides, we have evidenced the absence of thermal effects in the Coulomb blockade regime, paving the way for probing photon assisted tunnelling transport by exciting the GQD device with coherent THz photons [121] and THz light-matter coupling by the insertion of the GQD in a THz resonator.

As a perspective of this work, we will investigate the photoresponse of the GQD under coherent THz illumination. In this way, very interesting preliminary results have been already obtained by Simon Messelot, which show assisted photo-tunnelling features in the photocurrent response. Moreover, we will tune the frequency of the THz source to the predicted large intraband absorption to probe the interaction of the THz photons with the excited states of the GQD. As a more long term perspective, we will insert the GQD based devices in a high quality factor THz microcavity to investigate (ultra)strong THz light-matter coupling.

# General conclusion

The goal of my thesis was to explore the electronic and optical properties of graphene quantum dots in the THz spectral range. To this end, I have carried out distinct approaches which, although different, are complementary and present a global view of the physics of these materials.

In **Chapter 1**, we have first calculated the electronic state distribution and the associated wavefunctions of GQDs within the nearest-neighbour tight-binding model. The strategy was to not impose any condition on the edge shape of the GQDs, and follow the evolution of their complex electronic structure while varying their dimension. From this study, I have identify three main types of energy states: edge states, mixed states and bulk states. The edge states concentrate on the edges of the dot and are almost zero-energy. The bulk states correspond to the normal modes of the GQD due to its finite size. The mixed states are the more numerous, they spatially extend on all the GQD surface and thus dominate the energy spectrum. From the calculation of the absorption probability spectrum for large GQDs, we found that very efficient intraband transitions between mixed and bulk states can be induced by low energy photons, i.e. THz photons. The main result is that the absorption can reach more than 20% and 40 % at room temperature for doping levels of $E_F = 200\ meV$ and 300 $meV$ respectively. That is 10 to 20 times higher than in bulk graphene, and the resonance frequency tunability remains robust no matter the edge structure of the GQD.

Then I presented in **Chapter 2** the experimental investigation of the optical properties of GQDs at THz frequencies. Using THz time-domain spectroscopy, in-depth transmittance characterisations of a multilayer epitaxial graphene have been carried out. This material was then nanostructured in a $\sim 10^7$ GQDs array and I probed its optical properties at THz frequencies by THz-TDS. My results show that the THz response of GQDs with diameters of few tens of nm is characterised by a deep absorption around 6 THz at low and room temperature. Additionnal weak absorption resonances at lower frequency are also observed at low temperature. These original outcomes are supported by the theoretical analysis developed in Chapter 1 and are strongly different from what is observed in MEG.

Finally, I focused in **Chapter 3** on the electronic transport properties of a single graphene quantum dot in the Coulomb-blockade regime. A full encapsulation of monolayer graphene has been done with hBN layers and processed in a GQD-based single electron device coupled to a bow-tie antenna. Jointly with a post doc of my team (Elisa Riccardi), transport spectroscopy measurements were performed. Owing to the hBN encapsulation, we observed very stable and well-defined Coulomb diamonds at low temperature, as well as GQD excited states of energy $\sim 1.7\ meV$ (0.4 THz). Furthermore, the photoresponse of a GQD in Coulomb blockade regime under incoherent THz illumination has been investigated. Under a ∼10 pW THz radiation, the photocurrent response is in the nA range, resulting from a renormalization of the chemical potential of the GQD. We have shown that this effect evolves

nonlinearly with the incident power and attribute it to interfacial photogating effect.

To conclude, I would like to mention that these interesting results open very exciting perspectives. Our theory suggests that we can also play on the GQD asymmetry to get a polarization-dependent absorption. Further experimental developments are appealing: a silicon lens added on the surface of a GQDs array, combined with transparent electrods would enhance its THz absorption and enable to control their Fermi level. Finally, very interesting preliminary results have been obtained in my group by Simon Messelot on the photoresponse of a single GQD under coherent THz illumination. These results show the high potential of graphene nanostructures for the developement of GQD-based devices operating in the THz range.

# Appendix

## Fermi level determination of MEG

In this appendix, we present the magnetospectroscopy measurements performed by M. Krizman and L.A. De Vaulchier on the initial 30-layer MEG used to fabricate sample C1. We first start by a brief description of magnetospectroscopy princple.

The application of a perpendicular magnetic field to a two-dimensional electron gas confines the carriers in the plane, replacing the energy band dispersion by a scale of discrete energy levels, the Landau levels. In usual semi-conductors, the Landau levels evolve linearly with the magnetic field $B$ due to the parabolic band dispersion. In graphene however, because of the relativistic nature of the electrons, the Landau levels $E_n$ evolve as $\sqrt{B}$ [122]:

$$E_n = sign(n) v_F \sqrt{2e\hbar B|n|} = sign(n) E_1 \sqrt{|n|} \tag{13}$$

with $n = 0, \pm 1, \pm 2, ..$ and $v_F$ the Fermi velocity which is the only ajustable parameter.

The MEG sample is cooled down to $T = 4.2$ K and its relative transmittance to infrared radiation is measured as function of the magnetic field. An optical transition is allowed only if the Landau levels below/above the Fermi level $E_F$ is (at least partially) occupied/empty. One way to get the Fermi level of the MEG sample is therefore to follow a given intraband transition (between two states of Landau level index $n$ of same sign) and identify the magnetic field from which it disappears.
Figure 26 shows the relative transmittance of the MEG sample to photons of various energies (10-620 meV), while varying the magnetic field from 15 to 0.25 T. The investigated spectral range covers the spectral area from mid-infrared (MIR) to far-infrared (FIR).
Dark and red arrows point the intraband absorption between Landau levels such as $n \rightarrow n+1$. The corresponding transition energy observed at a given magnetic field $B$ is subsequently reported as function of $B$ on Figure 27 (dark and red dots). From the clear MIR-signature of Landau transitions 1-2 and 2-3 at high magnetic field, we can extract a Fermi velocity of 1.02 $10^6$ $m.s^{-1}$ and thus plot the expected evolution of $E_{n+1} - E_n$ as function of $B$ using equation (13) (solid lines).
The red arrows on Figure 26 follow the Landau transitions 0-1 as function of the magnetic field. The red star on Figure 26 and 27 (b) denote the magnetic field at which this transition disapears. From the related energy, we extract a Fermi level of $E_F = 20$ meV.

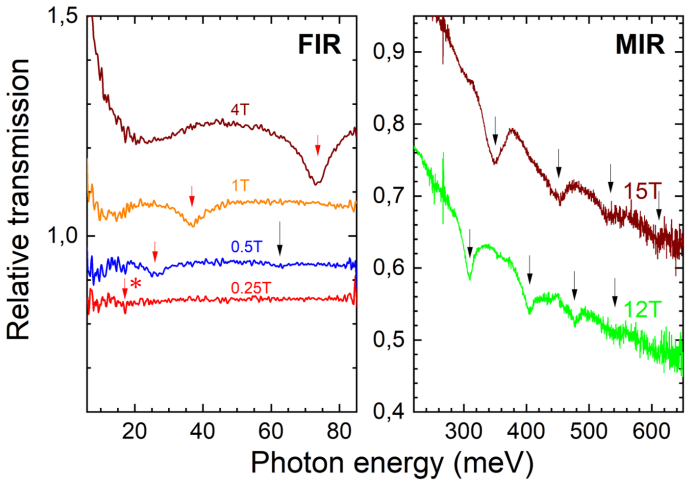


Figure 26: *Relative transmission spectra in FIR and MIR energy range for different values of the magnetic field.*

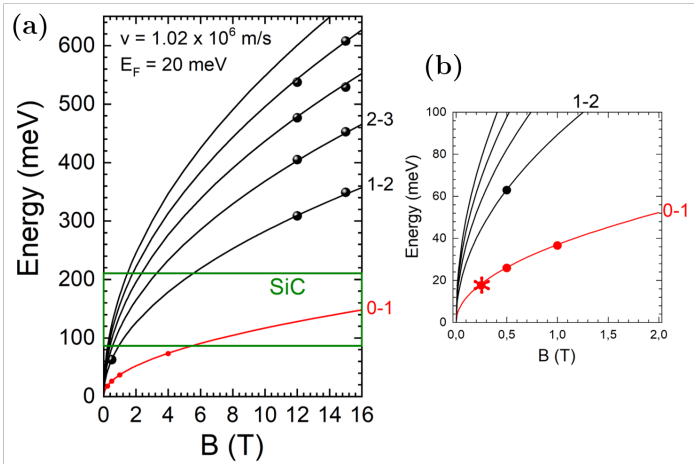


Figure 27: *Energy of intraband transitions between Landau levels, as function of the magnetic field $B$, over a large (a) and reduced (b) scale. Red and black spots correspond to the energy/magnetic field couples denoted by red and black arrows in Figure 26, respectively. Dark and red solid lines correspond to the expected evolution of $E_{n+1} - E_n$ as function of $B$, plotted using equation* (13).

# Bibliography


[1] P. R. Wallace, "The Band Theory of Graphite," *Phys. Rev.*, vol. 71, pp. 622–634, May 1947.

[2] D. P. DiVincenzo and E. J. Mele, "Self-consistent effective-mass theory for intralayer screening in graphite intercalation compounds," *Phys. Rev. B*, vol. 29, pp. 1685–1694, Feb. 1984.

[3] G. W. Semenoff, "Condensed-Matter Simulation of a Three-Dimensional Anomaly," *Phys. Rev. Lett.*, vol. 53, pp. 2449–2452, Dec. 1984.

[4] K. S. Novoselov, "Electric Field Effect in Atomically Thin Carbon Films," *Science*, vol. 306, pp. 666–669, Oct. 2004.

[5] P. R. Somani, S. P. Somani, and M. Umeno, "Planer nano-graphenes from camphor by CVD," *Chemical Physics Letters*, vol. 430, pp. 56–59, Oct. 2006.

[6] C. Berger, Z. Song, T. Li, X. Li, A. Y. Ogbazghi, R. Feng, Z. Dai, A. N. Marchenkov, E. H. Conrad, P. N. First, and W. A. de Heer, "Ultrathin Epitaxial Graphite: 2D Electron Gas Properties and a Route toward Graphene-based Nanoelectronics," *J. Phys. Chem. B*, vol. 108, pp. 19912–19916, Dec. 2004.

[7] C. Lee, X. Wei, J. W. Kysar, and J. Hone, "Measurement of the Elastic Properties and Intrinsic Strength of Monolayer Graphene," *Science*, vol. 321, pp. 385–388, July 2008.

[8] K. S. Novoselov, A. K. Geim, S. V. Morozov, D. Jiang, M. I. Katsnelson, I. V. Grigorieva, S. V. Dubonos, and A. A. Firsov, "Two-dimensional gas of massless Dirac fermions in graphene," *Nature*, vol. 438, pp. 197–200, Nov. 2005.

[9] Y. Zhang, Y.-W. Tan, H. L. Stormer, and P. Kim, "Experimental observation of the quantum Hall effect and Berry's phase in graphene," *Nature*, vol. 438, pp. 201–204, Nov. 2005.

[10] C. Berger, "Electronic Confinement and Coherence in Patterned Epitaxial Graphene," *Science*, vol. 312, pp. 1191–1196, May 2006.

[11] M. I. Katsnelson, K. S. Novoselov, and A. K. Geim, "Chiral tunnelling and the Klein paradox in graphene," *Nature Phys*, vol. 2, pp. 620–625, Sept. 2006.

[12] D. E. Sheehy and J. Schmalian, "Optical transparency of graphene as determined by the fine-structure constant," *Phys. Rev. B*, vol. 80, p. 193411, Nov. 2009. arXiv: 0906.5164.

[13] K. J. Tielrooij, J. C. W. Song, S. A. Jensen, A. Centeno, A. Pesquera, A. Z. Elorza, M. Bonn, L. S. Levitov, and F. H. L. Koppens, "Photoexcitation cascade and multiple hot-carrier generation in graphene," *Nature Physics*, vol. 9, no. 4, p. 248, 2013. Publisher: Nature Publishing Group.

[14] A. Tomadin, D. Brida, G. Cerullo, A. C. Ferrari, and M. Polini, "Nonequilibrium dynamics of photoexcited electrons in graphene: Collinear scattering, Auger processes, and the impact of screening," *Phys. Rev. B*, vol. 88, p. 035430, July 2013.

[15] S. Zhao, J. Lavie, L. Rondin, L. Orcin-Chaix, C. Diederichs, P. Roussignol, Y. Chassagneux, C. Voisin, K. Mullen, A. Narita, S. Campidelli, and J. S. Lauret, "Single photon emission from graphene quantum dots at room temperature," *Nature Communications*, vol. 9, p. 3470, 2018. Publisher: Nature Publishing Group.

[16] Y. Sun, Y. Zheng, H. Pan, J. Chen, W. Zhang, L. Fu, K. Zhang, N. Tang, and Y. Du, "Magnetism of graphene quantum dots," *npj Quant Mater*, vol. 2, p. 5, Dec. 2017.

[17] C. Mansilla Wettstein, F. P. Bonafé, M. B. Oviedo, and C. G. Sánchez, "Optical properties of graphene nanoflakes: Shape matters," *The Journal of Chemical Physics*, vol. 144, p. 224305, June 2016.

[18] L. Vicarelli, M. S. Vitiello, D. Coquillat, A. Lombardo, A. C. Ferrari, W. Knap, M. Polini, V. Pellegrini, and A. Tredicucci, "Graphene field-effect transistors as room-temperature terahertz detectors," *Nature materials*, vol. 11, no. 10, p. 865, 2012. Publisher: Nature Publishing Group.

[19] A. El Fatimy, R. L. Myers-Ward, A. K. Boyd, K. M. Daniels, D. K. Gaskill, and P. Barbara, "Epitaxial graphene quantum dots for high-performance terahertz bolometers," *Nature Nanotech*, vol. 11, pp. 335–338, Apr. 2016.

[20] M. Wimmer, A. R. Akhmerov, and F. Guinea, "Robustness of edge states in graphene quantum dots," *Phys. Rev. B*, vol. 82, p. 045409, July 2010.

[21] S. Caneva, M. Hermans, M. Lee, A. García-Fuente, K. Watanabe, T. Taniguchi, C. Dekker, J. Ferrer, H. S. J. van der Zant, and P. Gehring, "A Mechanically Tunable Quantum Dot in a Graphene Break Junction," *Nano Lett.*, vol. 20, pp. 4924–4931, July 2020.

[22] S. Chung, R. A. Revia, and M. Zhang, "Graphene Quantum Dots and Their Applications in Bioimaging, Biosensing, and Therapy," *Adv. Mater.*, p. 1904362, Dec. 2019.

[23] W. Chen, G. Lv, W. Hu, D. Li, S. Chen, and Z. Dai, "Synthesis and applications of graphene quantum dots: a review," *Nanotechnology Reviews*, vol. 7, pp. 157–185, Apr. 2018.

[24] W. Sheng, M. Korkusinski, A. D. Güçlü, M. Zielinski, P. Potasz, E. S. Kadantsev, O. Voznyy, and P. Hawrylak, "Electronic and optical properties of semiconductor and graphene quantum dots," *Frontiers of Physics*, vol. 7, no. 3, pp. 328–352, 2012. Publisher: Springer.

[25] R. Pohle, E. G. Kavousanaki, K. M. Dani, and N. Shannon, "Symmetry and optical selection rules in graphene quantum dots," *Phys. Rev. B*, vol. 97, p. 115404, Mar. 2018.

[26] P. Bugajny, L. Szulakowska, B. Jaworowski, and P. Potasz, "Optical properties of geometrically optimized graphene quantum dots," *Physica E: Low-dimensional Systems and Nanostructures*, vol. 85, pp. 294–301, Jan. 2017.

[27] T. Espinosa-Ortega, I. A. Luk'yanchuk, and Y. G. Rubo, "Density of states in randomly shaped graphene quantum dots," *Superlattices and Microstructures*, vol. 49, pp. 283–287, Mar. 2011.

[28] T. Basak, H. Chakraborty, and A. Shukla, "Theory of linear optical absorption in diamond-shaped graphene quantum dots," *Phys. Rev. B*, vol. 92, p. 205404, Nov. 2015.

[29] A. D. Güçlü, P. Potasz, and P. Hawrylak, "Excitonic absorption in gate-controlled graphene quantum dots," *Phys. Rev. B*, vol. 82, no. 15, p. 155445, 2010. Publisher: American Physical Society.

[30] F. Libisch, S. Rotter, J. Güttinger, C. Stampfer, and J. Burgdörfer, "Transition to Landau levels in graphene quantum dots," *Phys. Rev. B*, vol. 81, p. 245411, June 2010.

[31] Z. Z. Zhang, K. Chang, and F. M. Peeters, "Tuning of energy levels and optical properties of graphene quantum dots," *Phys. Rev. B*, vol. 77, p. 235411, June 2008.

[32] M. Zarenia, A. Chaves, G. A. Farias, and F. M. Peeters, "Energy levels of triangular and hexagonal graphene quantum dots: A comparative study between the tight-binding and Dirac equation approach," *Phys. Rev. B*, vol. 84, p. 245403, Dec. 2011.

[33] S. Schnez, K. Ensslin, M. Sigrist, and T. Ihn, "Analytic model of the energy spectrum of a graphene quantum dot in a perpendicular magnetic field," *Phys. Rev. B*, vol. 78, p. 195427, Nov. 2008.

[34] Q.-R. Dong and C.-X. Liu, "The optical selection rules of a graphene quantum dot in external electric fields," *RSC Adv.*, vol. 7, no. 37, pp. 22771–22776, 2017.

[35] F. Qi and G. Jin, "Strain sensing and far-infrared absorption in strained graphene quantum dots," *Journal of Applied Physics*, vol. 114, p. 073509, Aug. 2013.

[36] A. Grüneis, C. Attaccalite, L. Wirtz, H. Shiozawa, R. Saito, T. Pichler, and A. Rubio, "Tight-binding description of the quasiparticle dispersion of graphite and few-layer graphene," *Phys. Rev. B*, vol. 78, p. 205425, Nov. 2008.

[37] A. H. Castro Neto, F. Guinea, N. M. R. Peres, K. S. Novoselov, and A. K. Geim, "The electronic properties of graphene," *Rev. Mod. Phys.*, vol. 81, pp. 109–162, Jan. 2009.

[38] P. A. Maksimov, A. V. Rozhkov, and A. O. Sboychakov, "Localized electron states near the armchair edge of graphene," *Phys. Rev. B*, vol. 88, p. 245421, Dec. 2013.

[39] Y. Zhao, W. Li, and R. Tao, "A rigorous proof for non-existence of edge state in the semi-infinite armchair edged graphene," *Physica B: Condensed Matter*, vol. 407, pp. 724–728, Feb. 2012.

[40] A. Matulis and F. M. Peeters, "Quasibound states of quantum dots in single and bilayer graphene," *Phys. Rev. B*, vol. 77, p. 115423, Mar. 2008.

[41] S. Huppert, *Nonlinear transport and Terahertz generation in two-dimensional systems under strong optical irradiation*. Theses, Université Pierre et Marie Curie - Paris VI, Sept. 2014. Issue: 2014PA066217.

[42] K. F. Mak, L. Ju, F. Wang, and T. F. Heinz, "Optical spectroscopy of graphene: From the far infrared to the ultraviolet," *Solid State Communications*, vol. 152, pp. 1341–1349, Aug. 2012.

[43] C. Lee, J. Y. Kim, S. Bae, K. S. Kim, B. H. Hong, and E. J. Choi, "Optical response of large scale single layer graphene," *Appl. Phys. Lett.*, vol. 98, p. 071905, Feb. 2011.

[44] J. M. Dawlaty, S. Shivaraman, J. Strait, P. George, M. Chandrashekhar, F. Rana, M. G. Spencer, D. Veksler, and Y. Chen, "Measurement of the optical absorption spectra of epitaxial graphene from terahertz to visible," *Appl. Phys. Lett.*, vol. 93, p. 131905, Sept. 2008.

[45] J. Lloyd-Hughes and T.-I. Jeon, "A Review of the Terahertz Conductivity of Bulk and Nano-Materials," *J Infrared Milli Terahz Waves*, vol. 33, pp. 871–925, Sept. 2012.

[46] J. L. Tomaino, A. D. Jameson, J. W. Kevek, M. J. Paul, A. M. van der Zande, R. A. Barton, P. L. McEuen, E. D. Minot, and Y.-S. Lee, "Terahertz imaging and spectroscopy of large-area single-layer graphene," *Opt. Express*, vol. 19, p. 141, Jan. 2011.

[47] J. D. Buron, D. H. Petersen, P. Bøggild, D. G. Cooke, M. Hilke, J. Sun, E. Whiteway, P. F. Nielsen, O. Hansen, A. Yurgens, and P. U. Jepsen, "Graphene Conductance Uniformity Mapping," *Nano Lett.*, vol. 12, pp. 5074–5081, Oct. 2012.

[48] J. D. Buron, F. Pizzocchero, B. S. Jessen, T. J. Booth, P. F. Nielsen, O. Hansen, M. Hilke, E. Whiteway, P. U. Jepsen, P. Bøggild, and D. H. Petersen, "Electrically Continuous Graphene from Single Crystal Copper Verified by Terahertz Conductance Spectroscopy and Micro Four-Point Probe," *Nano Lett.*, vol. 14, pp. 6348–6355, Nov. 2014.

[49] I. Maeng, S. Lim, S. J. Chae, Y. H. Lee, H. Choi, and J.-H. Son, "Gate-Controlled Nonlinear Conductivity of Dirac Fermion in Graphene Field-Effect Transistors Measured by Terahertz Time-Domain Spectroscopy," *Nano Lett.*, vol. 12, pp. 551–555, Feb. 2012.

[50] L. Ren, Q. Zhang, J. Yao, Z. Sun, R. Kaneko, Z. Yan, S. Nanot, Z. Jin, I. Kawayama, M. Tonouchi, J. M. Tour, and J. Kono, "Terahertz and Infrared Spectroscopy of Gated Large-Area Graphene," *Nano Lett.*, vol. 12, pp. 3711–3715, July 2012.

[51] Z. Mics, K.-J. Tielrooij, K. Parvez, S. A. Jensen, I. Ivanov, X. Feng, K. Müllen, M. Bonn, and D. Turchinovich, "Thermodynamic picture of ultrafast charge transport in graphene," *Nat Commun*, vol. 6, p. 7655, Nov. 2015.

[52] C. J. Docherty and M. B. Johnston, "Terahertz Properties of Graphene," *J Infrared Milli Terahz Waves*, vol. 33, pp. 797–815, Aug. 2012.

[53] P. R. Whelan, V. Panchal, D. H. Petersen, D. M. A. Mackenzie, C. Melios, I. Pasternak, J. Gallop, F. W. Østerberg, P. U. Jepsen, W. Strupinski, O. Kazakova, and P. Bøggild, "Electrical Homogeneity Mapping of Epitaxial Graphene on Silicon Carbide," *ACS Appl. Mater. Interfaces*, vol. 10, pp. 31641–31647, Sept. 2018.

[54] P. R. Whelan, X. Zhao, I. Pasternak, W. Strupinski, P. U. Jepsen, and P. Bøggild, "Non-contact mobility measurements of graphene on silicon carbide," *Microelectronic Engineering*, vol. 212, pp. 9–12, May 2019.

[55] V. Clericò, J. A. D. Notario, N. Campos, D. Gómez, E. Diez, J. E. Velazquez, and Y. M. Meziani, "Terahertz spectroscopy of a multilayers flake of graphene," *J. Phys.: Conf. Ser.*, vol. 647, p. 012040, Oct. 2015.

[56] I. Ivanov, Y. Hu, S. Osella, U. Beser, H. I. Wang, D. Beljonne, A. Narita, K. Müllen, D. Turchinovich, and M. Bonn, "Role of Edge Engineering in Photoconductivity of Graphene Nanoribbons," *J. Am. Chem. Soc.*, vol. 139, pp. 7982–7988, June 2017.

[57] H. A. Hafez, S. Kovalev, J. C. Deinert, Z. Mics, B. Green, N. Awari, M. Chen, S. Germanskiy, U. Lehnert, J. Teichert, and others, "Extremely efficient terahertz high-harmonic generation in graphene by hot Dirac fermions," *Nature*, vol. 561, no. 7724, p. 507, 2018. Publisher: Nature Publishing Group.

[58] M. Tani, S. Matsuura, K. Sakai, and S.-i. Nakashima, "Emission characteristics of photoconductive antennas based on low-temperature-grown GaAs and semi-insulating GaAs," *Appl. Opt.*, vol. 36, p. 7853, Oct. 1997.

[59] P. J. Hale, J. Madeo, C. Chin, S. S. Dhillon, J. Mangeney, J. Tignon, and K. M. Dani, "20 THz broadband generation using semi-insulating GaAs interdigitated photoconductive antennas," *Opt. Express*, vol. 22, p. 26358, Oct. 2014.

[60] G. Gallot and D. Grischkowsky, "Electro-optic detection of terahertz radiation," *J. Opt. Soc. Am. B*, vol. 16, p. 1204, Aug. 1999.

[61] P. C. M. Planken, H.-K. Nienhuys, H. J. Bakker, and T. Wenckebach, "Measurement and calculation of the orientation dependence of terahertz pulse detection in ZnTe," *J. Opt. Soc. Am. B*, vol. 18, p. 313, Mar. 2001.

[62] Q. Wu and X.-C. Zhang, "7 terahertz broadband GaP electro-optic sensor," *Appl. Phys. Lett.*, vol. 70, pp. 1784–1786, Apr. 1997.

[63] M. Baillergeau, *Dynamique térahertz des nanotubes de carbone*. Theses, Université Pierre et Marie Curie - Paris VI, Dec. 2015. Issue: 2015PA066464.

[64] R. Fastampa, L. Pilozzi, and M. Missori, "Cancellation of Fabry-Perot interference effects in terahertz time-domain spectroscopy of optically thin samples," *Phys. Rev. A*, vol. 95, p. 063831, June 2017.

[65] W. A. de Heer, C. Berger, M. Ruan, M. Sprinkle, X. Li, Y. Hu, B. Zhang, J. Hankinson, and E. Conrad, "Large area and structured epitaxial graphene produced by confinement controlled sublimation of silicon carbide," *Proceedings of the National Academy of Sciences*, vol. 108, pp. 16900–16905, Oct. 2011.

[66] J. Hass, F. Varchon, J. E. Millán-Otoya, M. Sprinkle, N. Sharma, W. A. de Heer, C. Berger, P. N. First, L. Magaud, and E. H. Conrad, "Why Multilayer Graphene on 4 H - SiC ( 000 1 $^{-}$ ) Behaves Like a Single Sheet of Graphene," *Phys. Rev. Lett.*, vol. 100, p. 125504, Mar. 2008.

[67] M. Sprinkle, D. Siegel, Y. Hu, J. Hicks, A. Tejeda, A. Taleb-Ibrahimi, P. Le Fèvre, F. Bertran, S. Vizzini, H. Enriquez, S. Chiang, P. Soukiassian, C. Berger, W. A. de Heer, A. Lanzara, and E. H. Conrad, "First Direct Observation of a Nearly Ideal Graphene Band Structure," *Phys. Rev. Lett.*, vol. 103, p. 226803, Nov. 2009.

[68] M. Orlita, C. Faugeras, P. Plochocka, P. Neugebauer, G. Martinez, D. K. Maude, A.-L. Barra, M. Sprinkle, C. Berger, W. A. de Heer, and M. Potemski, "Approaching the Dirac Point in High-Mobility Multilayer Epitaxial Graphene," *Phys. Rev. Lett.*, vol. 101, p. 267601, Dec. 2008.

[69] D. Sun, C. Divin, C. Berger, W. A. de Heer, P. N. First, and T. B. Norris, "Spectroscopic Measurement of Interlayer Screening in Multilayer Epitaxial Graphene," *Phys. Rev. Lett.*, vol. 104, p. 136802, Apr. 2010.

[70] A. J. Frenzel, C. H. Lui, Y. C. Shin, J. Kong, and N. Gedik, "Semiconducting-to-Metallic Photoconductivity Crossover and Temperature-Dependent Drude Weight in Graphene," *Phys. Rev. Lett.*, vol. 113, no. 5, p. 6, 2014. Publisher: American Physical Society.

[71] I. Crassee, M. Orlita, M. Potemski, A. L. Walter, M. Ostler, T. Seyller, I. Gaponenko, J. Chen, and A. B. Kuzmenko, "Intrinsic Terahertz Plasmons and Magnetoplasmons in Large Scale Monolayer Graphene," *Nano Lett.*, vol. 12, pp. 2470–2474, May 2012.

[72] M. T. Mihnev, F. Kadi, C. J. Divin, T. Winzer, S. Lee, C.-H. Liu, Z. Zhong, C. Berger, W. A. de Heer, E. Malic, A. Knorr, and T. B. Norris, "Microscopic origins of the terahertz carrier relaxation and cooling dynamics in graphene," *Nat Commun*, vol. 7, p. 11617, Sept. 2016.

[73] M. Orlita, C. Faugeras, R. Grill, A. Wysmolek, W. Strupinski, C. Berger, W. A. de Heer, G. Martinez, and M. Potemski, "Carrier Scattering from Dynamical Magnetoconductivity in Quasineutral Epitaxial Graphene," *Phys. Rev. Lett.*, vol. 107, p. 216603, Nov. 2011.

[74] T. Stauber, N. M. R. Peres, and F. Guinea, "Electronic transport in graphene: A semiclassical approach including midgap states," *Phys. Rev. B*, vol. 76, p. 205423, Nov. 2007.

[75] S. Das Sarma, S. Adam, E. H. Hwang, and E. Rossi, "Electronic transport in two-dimensional graphene," *Rev. Mod. Phys.*, vol. 83, pp. 407–470, May 2011.

[76] T. O. Wehling, S. Yuan, A. I. Lichtenstein, A. K. Geim, and M. I. Katsnelson, "Resonant Scattering by Realistic Impurities in Graphene," *Phys. Rev. Lett.*, vol. 105, p. 056802, July 2010.

[77] S. Massabeau, M. Baillergeau, T. Phuphachong, C. Berger, W. A. de Heer, S. Dhillon, J. Tignon, L. A. de Vaulchier, R. Ferreira, and J. Mangeney, "Evidence of Fermi level pinning at the Dirac point in epitaxial multilayer graphene," *Phys. Rev. B*, vol. 95, p. 085311, Feb. 2017.

[78] S. Winnerl, F. Göttfert, M. Mittendorff, H. Schneider, M. Helm, T. Winzer, E. Malic, A. Knorr, M. Orlita, M. Potemski, M. Sprinkle, C. Berger, and W. A. de Heer, "Time-resolved spectroscopy on epitaxial graphene in the infrared spectral range: relaxation dynamics and saturation behavior," *J. Phys.: Condens. Matter*, vol. 25, p. 054202, Feb. 2013.

[79] J. H. Strait, H. Wang, S. Shivaraman, V. Shields, M. Spencer, and F. Rana, "Very Slow Cooling Dynamics of Photoexcited Carriers in Graphene Observed by Optical-Pump Terahertz-Probe Spectroscopy," *Nano Lett.*, vol. 11, pp. 4902–4906, Nov. 2011.

[80] S. Winnerl, M. Orlita, P. Plochocka, P. Kossacki, M. Potemski, T. Winzer, E. Malic, A. Knorr, M. Sprinkle, C. Berger, W. A. de Heer, H. Schneider, and M. Helm, "Carrier Relaxation in Epitaxial Graphene Photoexcited Near the Dirac Point," *Phys. Rev. Lett.*, vol. 107, p. 237401, Nov. 2011.

[81] T. Winzer, R. Jago, and E. Malic, "Experimentally accessible signatures of Auger scattering in graphene," *Phys. Rev. B*, vol. 94, p. 235430, Dec. 2016.

[82] I. Ozfidan, M. Korkusinski, A. D. Güçlü, J. A. McGuire, and P. Hawrylak, "Microscopic theory of the optical properties of colloidal graphene quantum dots," *Phys. Rev. B*, vol. 89, p. 085310, Feb. 2014.

[83] V. I. Klimov, "Quantization of Multiparticle Auger Rates in Semiconductor Quantum Dots," *Science*, vol. 287, pp. 1011–1013, Feb. 2000.

[84] E. Riccardi, S. Massabeau, F. Valmorra, S. Messelot, M. Rosticher, J. Tignon, K. Watanabe, T. Taniguchi, M. Delbecq, S. Dhillon, R. Ferreira, S. Balibar, T. Kontos, and J. Mangeney, "Ultrasensitive Photoresponse of Graphene Quantum Dots in the Coulomb Blockade Regime to THz Radiation," *Nano Lett.*, vol. 20, pp. 5408–5414, July 2020.

[85] J. S. Bunch, Y. Yaish, M. Brink, K. Bolotin, and P. L. McEuen, "Coulomb Oscillations and Hall Effect in Quasi-2D Graphite Quantum Dots," *Nano Lett.*, vol. 5, pp. 287–290, Feb. 2005. Publisher: American Chemical Society.

[86] C. Stampfer, J. Güttinger, F. Molitor, D. Graf, T. Ihn, and K. Ensslin, "Tunable Coulomb blockade in nanostructured graphene," *Appl. Phys. Lett.*, vol. 92, no. 1, p. 012102, 2008.

[87] T. Ihn, J. Güttinger, F. Molitor, S. Schnez, E. Schurtenberger, A. Jacobsen, S. Hellmüller, T. Frey, S. Dröscher, C. Stampfer, and K. Ensslin, "Graphene single-electron transistors," *Materials Today*, vol. 13, pp. 44–50, Mar. 2010.

[88] L. A. Ponomarenko, F. Schedin, M. I. Katsnelson, R. Yang, E. W. Hill, K. S. Novoselov, and A. K. Geim, "Chaotic Dirac billiard in graphene quantum dots," *Science*, vol. 320, no. 5874, pp. 356–358, 2008. Publisher: American Association for the Advancement of Science.

[89] S. Schnez, F. Molitor, C. Stampfer, J. Güttinger, I. Shorubalko, T. Ihn, and K. Ensslin, "Observation of excited states in a graphene quantum dot," *Applied Physics Letters*, vol. 94, no. 1, p. 012107, 2009. Publisher: AIP.

[90] J. Güttinger, F. Molitor, C. Stampfer, S. Schnez, A. Jacobsen, S. Dröscher, T. Ihn, and K. Ensslin, "Transport through graphene quantum dots," *Rep. Prog. Phys.*, vol. 75, p. 126502, Dec. 2012.

[91] D. Bischoff, A. Varlet, P. Simonet, T. Ihn, and K. Ensslin, "Electronic triple-dot transport through a bilayer graphene island with ultrasmall constrictions," *New J. Phys.*, vol. 15, p. 083029, Aug. 2013.

[92] C. Volk, C. Neumann, S. Kazarski, S. Fringes, S. Engels, F. Haupt, A. Muller, and C. Stampfer, "Probing relaxation times in graphene quantum dots," *Nature Communications*, vol. 103, no. 7, p. 073113, 2013. Publisher: AIP.

[93] D. Bischoff, A. Varlet, P. Simonet, M. Eich, H. C. Overweg, T. Ihn, and K. Ensslin, "Localized charge carriers in graphene nanodevices," *Applied Physics Reviews*, vol. 2, p. 031301, Sept. 2015.

[94] M. Eich, R. Pisoni, H. Overweg, A. Kurzmann, Y. Lee, P. Rickhaus, T. Ihn, K. Ensslin, F. Herman, M. Sigrist, K. Watanabe, and T. Taniguchi, "Spin and Valley States in Gate-Defined Bilayer Graphene Quantum Dots," *Phys. Rev. X*, vol. 8, p. 031023, July 2018.

[95] A. Kurzmann, H. Overweg, M. Eich, A. Pally, P. Rickhaus, R. Pisoni, Y. Lee, K. Watanabe, T. Taniguchi, T. Ihn, and K. Ensslin, "Charge Detection in Gate-Defined Bilayer Graphene Quantum Dots," *Nano Lett.*, vol. 19, pp. 5216–5221, Aug. 2019.

[96] A. Kurzmann, M. Eich, H. Overweg, M. Mangold, F. Herman, P. Rickhaus, R. Pisoni, Y. Lee, R. Garreis, C. Tong, K. Watanabe, T. Taniguchi, K. Ensslin, and T. Ihn, "Excited States in Bilayer Graphene Quantum Dots," *Phys. Rev. Lett.*, vol. 123, p. 026803, July 2019.

[97] C. Stampfer, E. Schurtenberger, F. Molitor, J. Güttinger, T. Ihn, and K. Ensslin, "Tunable Graphene Single Electron Transistor," *Nano Lett.*, vol. 8, pp. 2378–2383, Aug. 2008.

[98] A. E. Fatimy, R. L. Myers-Ward, A. K. Boyd, K. M. Daniels, D. K. Gaskill, and P. Barbara, "Epitaxial graphene quantum dots for high-performance terahertz bolometers," *Nature nanotechnology*, vol. 11, no. 4, p. 335, 2016. Publisher: Nature Publishing Group.

[99] A. E. Fatimy, A. Nath, B. D. Kong, A. K. Boyd, R. L. Myers-Ward, K. M. Daniels, M. M. Jadidi, T. E. Murphy, D. K. Gaskill, and P. Barbara, "Ultra-broadband photodetectors based on epitaxial graphene quantum dots," *Nanophotonics*, vol. 7, no. 4, p. 735, 2018. Publisher: De Gruyter.

[100] S. Engels, A. Epping, C. Volk, S. Korte, B. Voigtländer, K. Watanabe, T. Taniguchi, S. Trellenkamp, and C. Stampfer, "Etched graphene quantum dots on hexagonal boron nitride," *Applied Physics Letters*, vol. 103, no. 7, p. 073113, 2013. Publisher: AIP.

[101] P. Huang, E. Riccardi, S. Messelot, H. Graef, F. Valmorra, J. Tignon, T. Taniguchi, K. Watanabe, S. Dhillon, B. Plaçais, R. Ferreira, and J. Mangeney, "Ultra-long carrier lifetime in neutral graphene-hBN van der Waals heterostructures under mid-infrared illumination," *Nature Communications*, vol. 11, no. 1, p. 863, 2020. Publisher: Nature Publishing Group.

[102] C. R. Dean, A. F. Young, I. Meric, C. Lee, L. Wang, S. Sorgenfrei, K. Watanabe, T. Taniguchi, P. Kim, K. L. Shepard, and J. Hone, "Boron nitride substrates for high-quality graphene electronics," *Nature Nanotech*, vol. 5, pp. 722–726, Oct. 2010.

[103] F. Pizzocchero, L. Gammelgaard, B. S. Jessen, J. M. Caridad, L. Wang, J. Hone, P. Bøggild, and T. J. Booth, "The hot pick-up technique for batch assembly of van der Waals heterostructures," *Nat Commun*, vol. 7, p. 11894, Sept. 2016.

[104] L. Wang, I. Meric, P. Y. Huang, Q. Gao, Y. Gao, H. Tran, T. Taniguchi, K. Watanabe, L. M. Campos, D. A. Muller, J. Guo, P. Kim, J. Hone, K. L. Shepard, and C. R. Dean, "One-Dimensional Electrical Contact to a Two-Dimensional Material," *Science*, vol. 342, pp. 614–617, Nov. 2013.

[105] L. P. Kouwenhoven, C. M. Marcus, P. L. McEuen, S. Tarucha, R. M. Westervelt, and N. S. Wingreen, "Electron Transport in Quantum Dots," in *Mesoscopic Electron Transport* (L. L. Sohn, L. P. Kouwenhoven, and G. Schön, eds.), pp. 105–214, Dordrecht: Springer Netherlands, 1997.

[106] L. Bruhat, *Microwaves as a probe of quantum dot circuits: from Kondo dynamics to mesoscopic quantum electrodynamics.* Theses, Université de recherche Paris Sciences Lettres, Apr. 2016.

[107] D. Bischoff, F. Libisch, J. Burgdörfer, T. Ihn, and K. Ensslin, "Characterizing wave functions in graphene nanodevices: Electronic transport through ultrashort graphene constrictions on a boron nitride substrate," *Phys. Rev. B*, vol. 90, p. 115405, Sept. 2014.

[108] G. Hackenbroich, W. D. Heiss, and H. A. Weidenmüller, "Deformation of Quantum Dots in the Coulomb Blockade Regime," *Phys. Rev. Lett.*, vol. 79, pp. 127–130, July 1997.

[109] M. Shimatani, N. Yamada, S. Fukushima, S. Okuda, S. Ogawa, T. Ikuta, and K. Maehashi, "High-responsivity turbostratic stacked graphene photodetectors using enhanced photogating," *Applied Physics Express*, vol. 12, no. 12, p. 122010, 2019. Publisher: Japan Society of Applied Physics.

[110] H. Fang and W. Hu, "Photogating in Low Dimensional Photodetectors," *Advanced Science*, vol. 4, no. 12, p. 1700323, 2017.

[111] J. Dai, J. Zhang, W. Zhang, and D. Grischkowsky, "Terahertz time-domain spectroscopy characterization of the far-infrared absorption and index of refraction of high-resistivity, float-zone silicon," *J. Opt. Soc. Am. B*, vol. 21, no. 7, p. 1379, 2004. Publisher: Optical Society of America.

[112] E. D. Palik, *Handbook of Optical Constants of Solids*. New York: Academic, 1998. Publication Title: Academic Press.

[113] Y. Jiang, K. Vijayraghavan, S. Jung, F. Demmerle, G. Boehm, M. C. Amann, and M. A. Belkin, "External cavity terahertz quantum cascade laser sources based on intracavity frequency mixing with 1.2–5.9 THz tuning range," *Journal of Optics*, vol. 16, no. 9, p. 094002, 2014. Publisher: IOP Publishing.

[114] H.-W. Hubers, S. G. Pavlov, M. H. Rummeli, R. K. Zhukavin, E. E. Orlovab, H. Riemann, and V. N. Shastin, "Terahertz emission from silicon doped by shallow impurities," *Physica B: Condensed Matter*, vol. 308-310, no. 1, p. 232, 2001. Publisher: Elsevier.

[115] X. Guo, W. Wang, H. Nan, Y. Yu, J. Jiang, W. Zhao, J. Li, Z. Zafar, N. Xiang, Z. Ni, and others, "High-performance graphene photodetector using interfacial gating," *Optica*, vol. 3, no. 10, p. 1066, 2016. Publisher: OSA.

[116] Y. Liu, Q. Xia, J. He, and Z. Liu, "Direct Observation of High Photoresponsivity in Pure Graphene Photodetectors," *Nanoscale Research Letters*, vol. 12, no. 1, p. 93, 2017. Publisher: Springer.

[117] S. Ogawa, M. Shimatani, S. Fukushima, S. Okuda, Y. Kanai, T. Ono, and K. Matsumoto, "Broadband photoresponse of graphene photodetector from visible to long-wavelength infrared wavelengths," *Optical Engineering*, vol. 58, no. 5, p. 1, 2019. Publisher: SPIE.

[118] F. H. L. Koppens, T. Mueller, P. Avouris, A. C. Ferrari, M. S. Vitiello, and M. Polini, "Photodetectors based on graphene, other two-dimensional materials and hybrid systems," *Nature Nanotechnology*, vol. 9, no. 10, p. 780, 2014. Publisher: Nature Publishing Group.

[119] N. Q. Vinh, B. Redlich, A. F. G. v. d. Meer, C. R. Pidgeon, P. T. Greenland, S. A. Lynch, G. Aeppli, and B. N. Murdin, "Time-Resolved Dynamics of Shallow Acceptor Transitions in Silicon," *Phys. Rev. X*, vol. 3, no. 1, p. 011019, 2013. Publisher: American Physical Society.

[120] F. Luo, M. Zhu, Y. Tan, H. Sun, W. Luo, G. Peng, Z. Zhu, X.-A. Zhang, and S. Qin, "High responsivity graphene photodetectors from visible to near-infrared by photogating effect," *AIP Advances*, vol. 8, no. 11, p. 115106, 2018.

[121] Y. Kawano, T. Fuse, S. Toyokawa, T. Uchida, and K. Ishibashi, "Terahertz photon-assisted tunneling in carbon nanotube quantum dots," *Journal of Applied Physics*, vol. 103, no. 3, p. 034307, 2008. Publisher: AIP.

[122] M. L. Sadowski, G. Martinez, M. Potemski, C. Berger, and W. A. de Heer, "Landau Level Spectroscopy of Ultrathin Graphite Layers," *Phys. Rev. Lett.*, vol. 97, p. 266405, Dec. 2006.

# Résumé

Le graphène est un matériau bidimensionnel composé d'une couche monoatomique formée d'atomes de carbone dont l'ordonnancement se fait sous la forme d'un réseau hexagonal en nid d'abeille. Sa production contrôlée par exfoliation mécanique de cristaux de graphite en 2004 par Geim and Novoselov, qui fut récompensée par le prix Nobel de Physique en 2010, et complétée par la suite par d'autres techniques de fabrication (dépôt chimique en phase vapeur, croissance épitaxiale sur du carbure de silicium) permit d'explorer expérimentalement les propriétés exceptionnelles du graphène.

La grande variété des propriétés physiques de ce matériau provient en grande partie de sa structure cristalline. Outre une résistance mécanique très élevée (module d'Young $\sim$ 1 TPa), la structure de bande du graphène est linéaire à basse énergie. Les électrons qui composent cette bande se comportent ainsi comme des particules relativistes de masse quasi-nulle, i.e. des Fermions de Dirac, qui peuvent se déplacer à une vitesse proche de celle des photons ($v_F = c/300 \sim 10^6\ m.s^{-1}$). Cela se traduit par l'observation d'un certain nombre de propriétés particulières telles que l'effet Hall quantique fractionnaire, un transport électronique balistique à l'échelle du $\mu$m ou bien encore l'effet tunnel de Klein.

Le graphène a également une réponse optique très large bande. Une seule couche monoatomique de graphène conduit à une absorption de 2,3% de la lumière du visible à l'infrarouge. L'absence de bande interdite dans le graphène et la dispersion linéaire des électrons de faible énergie impliquent également que des transitions interbandes peuvent être induites par un rayonnement Térahertz (THz), c'est-à-dire par des photons de quelques meV. La gamme spectrale Térahertz s'étend typiquement de 0.1 THz à 10 THz, soit de 0.4 meV à 41 meV en énergie. Par conséquent, le graphène correspond de manière unique au modèle de laser à semi-conducteur pour la génération THz. Cela fait en fait un matériau très prometteur pour soutenir le développement de technologies THz qui manquent cruellement de sources puissantes et compactes. Cette perspective a stimulé de nombreux travaux expérimentaux et théoriques, qui ont conduit à la démonstration d'une inversion de population et d'un gain optique dans le graphène sous excitation optique intense, suggérant qu'une émission laser THz est possible. Cependant, la durée de vie du gain optique d'une monocouche de graphène est limitée à quelques centaines de femtosecondes en raison de processus de recombinaison non radiatifs, en particulier la recombinaison Auger qui domine la dynamique des porteurs. La recombinaison Auger est un processus de diffusion dans lequel la recombinaison d'une paire électron-trou pousse un autre électron aux énergies plus élevées. Ce gain optique de courte durée dans le graphène est préjudiciable pour le développement de lasers THz. Néanmoins, ce processus peut être réduit en limitant les états finaux disponibles pour l'électron diffusé.

La stratégie menée par mon équipe de recherche est de réaliser la discrétisation complète des états électroniques du graphène dans le but d'inhiber les processus de recombinaison Auger. La discrétisation des niveaux électroniques est obtenue en réduisant l'extension spatiale du graphène à quelques dizaines de nanomètres dans toutes les directions du plan, définissant ainsi une boite quantique de graphène (BQG). Une BQG est un nano-objet de dimension

quasi-nulle, parfois appelé "atome artificiel" de par la nature discrète de son spectre électronique. Les BQG ont suscité un intérêt considérable pour la nanoélectronique et l'optique. En effet, le graphène est un semi-métal, ce qui constitue une limitation sévère pour de nombreuses applications. Ce problème peut être résolu dans les BQG car une bande interdite s'ouvre en raison du confinement quantique. Enfin, leurs propriétés sont ajustables. Pour une BQG de dimension $D$, les conditions aux limites de la fonction d'onde permettent d'obtenir une estimation de l'espacement $\Delta E$ entre les niveaux d'énergie $\Delta E \propto \hbar v_F/D$. Ainsi, on peut varier la dimension d'une BQG de quelques nanomètres à plusieurs dizaines de nanomètres afin d'obtenir un $\Delta E \sim 1\ eV - 1\ meV$ et étudier son interaction (absorption, émission) avec des photons d'énergies couvrant tout le spectre électromagnétique.

Le but de cette thèse est d'étudier les propriétés optiques et électroniques dans la gamme spectrale THz de boîtes quantiques de graphène de diamètre de quelques dizaines de nanomètres.

Le **Chapitre 1** porte sur l'étude théorique des propriétés électroniques et optiques des boîtes quantiques de graphène. Ce projet a été réalisé en étroite collaboration avec Robson Ferreira et Nicolas Regnault (groupe Théorie de la matière condensée au LPENS).

Dans un premier temps, on calcule les niveaux d'énergie discrets et les fonctions d'onde associées de BQG de diamètre de 6 nm à 50 nm, en utilisant le formalisme des liaisons fortes. Une BQG de diamètre $D$ est définie en gardant les atomes de carbone du graphène contenus dans un cercle de diamètre $D$. Les atomes de carbone n'ayant qu'un seul voisin (liaisons pendantes) sur les bords ne sont pas conservés, en supposant qu'ils ne survivent probablement pas lors du processus de fabrication (lithographie électronique). De ce fait, aucune condition particulière n'est imposée sur les bords de la nanostructure. Comme le processus de fabrication des BQG ne permet pas le contrôle exact de la forme des bords, cette définition est très importante pour mieux décrire un système réel composé de BQG.

Par la suite, on se propose d'analyser les différents types d'états électroniques qui composent le spectre des BQG. La nature des états et leur dispersion en énergie va dépendre de la dimension de la nanostructure de graphène, ainsi que de la structure de ses bords. Deux types de structures sont possibles sur les bords : zigzag et chaise (armchair). Comme des BQG de différentes tailles contiennent une fraction aléatoire de chaque type, ces systèmes sont difficiles à décrire analytiquement. Différentes approches sont donc développées, ce qui permet de classer les états électroniques des BQG en trois familles : des états de bords, des états massifs et des états "mixtes". Les états massifs correspondent à des fonctions d'onde qui s'étendent sur toute la surface de la nanostructure, et sont identifiés en utilisant un modèle continu à basse énergie qui permet d'obtenir une expression analytique de leur dispersion en énergie. Les états de bords sont d'énergie quasi-nulle et leurs fonctions d'onde sont très localisées sur les bords des BQG, majoritairement au voisinage des bords zigzag, ce qui est conforme à la littérature existante sur les nanostructures de graphène (boîtes quantiques, nanotubes de carbone et nanorubans de graphène). Les états "mixtes" sont caractérisés par une fonction d'onde qui s'étend sur les bords ainsi que sur le massif. Ces bords particuliers sont majoritairement de type chaise. De plus, les états mixtes sont les plus nombreux et dominent donc le spectre en énergie des BQG de quelques dizaine de nanomètres de diamètre. Ces observations sont obtenues en traçant la densité de probabilité des BQG et en définissant un paramètre qui permet d'évaluer l'extension spatiale des fonctions d'onde pour une énergie donné. Cette approche permet également de discriminer les états massifs dans le spectre en énergie.

Dans la dernière partie du chapitre, on s'intéresse au couplage des photons THz avec les états électroniques variés des BQG de quelques dizaines de nanomètres. Le formalisme de

la réponse linéaire d'un matériau à une excitation optique basse énergie permet d'obtenir la probabilité d'absorption des nanostructures de graphène. Dans un premier temps, le couplage avec la lumière entre tous les niveaux d'énergie discrets est étudié, sans considérer l'occupation de ces états. Cette étude montre que des transitions interbandes, similaires à celles observées dans le graphène, sont possibles et d'efficacité non-négligeable. Cependant, ce sont des transitions de type intrabande qui sont dominantes et très efficaces. En sélectionnant des exemples parmi les différentes familles d'état, on observe que les états de bords ne jouent aucun rôle dans l'absorption. Ce sont principalement les états mixtes, très nombreux, ainsi que les états massifs, dans une moindre mesure, qui conduisent à des transitions intrabande très efficaces via des photons de basse énergie.

Enfin, on étudie l'influence des dimensions de la BQG ainsi que de l'occupation des niveaux électroniques (niveau de dopage et température) sur la probabilité d'absorption. Les transitions intrabandes efficaces sont présentes pour toutes les BQG de diamètre de quelques dizaines de nanomètres. Ces transitions peuvent être activées en fonction du niveau de dopage et de la température. Un résultat important est que les transitions intrabande conduisent à un large pic absorption aux fréquences THz. Notamment, l'absorption atteint plus de 20% et 40% lorsque le niveau de Fermi (dopage) des BQG est respectivement de 200 meV et 300 meV, à température ambiante. De manière remarquable, la fréquence correspondant à ce pic d'absorption est définie par les dimensions de la BQG et non par les détails (bords) de sa structure. Une large et robuste absorption aux fréquences THz est ainsi extrêmement prometteuse pour le développement de dispositifs optoélectroniques et photoniques fonctionnant dans le domaine spectral THz.

Le **Chapitre 2** est consacré à la fabrication de réseaux de boîtes quantiques de graphène et à l'investigation expérimentale de leur propriétés d'absorption aux fréquences THz, en utilisant un système de spectroscopie temporelle THz. Comme les BQG sont fabriquées à partir de graphène épitaxial multicouches (GEM) développée sur un substrat de carbure de silicium (SiC), nous commençons les expériences en sondant la réponse THz intrabande et interbande du GEM.

Le système de spectroscopie THz dans le domaine temporel (THz-TDS) utilisé dans cette thèse permet de mesurer la transmittance complexe d'un matériau aux fréquences THz. De par la grande longueur d'onde du rayonnement THz (300 $\mu$m à 1 THz), il n'est pas possible de mesurer la transmittance d'une seule BQG. Nous avons donc fabriqué un réseau de BQG sur une surface de 1 mm$^2$. Il est cependant crucial de réduire au maximum la taille du faisceau THz pour mesurer la transmittance de nos échantillon. Dans ce but, une approche originale basée sur le contrôle du front d'onde THz a récemment été développée dans mon équipe (Matthieu Baillergeau), ce qui permet de réduire la taille du faisceau THz du dispositif THz-TDS à la limite de diffraction pour des fréquences supérieures à 3 THz.

Le GEM utilisé comporte quelques couches au contact du substrat de SiC fortement dopées, ainsi que quelques dizaines de couche quasi-neutres. Les mesures de spectroscopie THz sur cette échantillon permettent d'extraire la conductivité complexe de ce matériau à différentes températures. L'évolution des spectres en transmission en fonction de la température, comparés aux modèles de conductivités inter et intrabande du graphène multicouches permet de montrer que des états "midgap" conduisent à un accrochage du niveau de Fermi des couches quasi-neutres au point de Dirac ($\sim$0 meV).

A partir de ces échantillons de GEM, plusieurs réseaux de BQG sont fabriqués par lithographie électronique suivie d'une gravure ionique réactive. Après de nombreuses améliorations du procédé de fabrication, une lithographie d'environ 60 heures permet d'obtenir un réseau comportant $\sim 10^7$ BQG de plusieurs dizaines de nanomètres de diamètre.

Dans un premier temps, on mesure la transmittance de ce réseau de BQG (noté C1) par spectroscopie THz, à basse température (4 K) et température ambiante. Aux deux températures, on observe un large pic d'absorption autour de 6 THz. A basse température, des résonances de plus faibles amplitudes apparaissent à plus basse fréquence. La faible taille de l'échantillon contraint cependant le protocole expérimental car il faut mesurer le signal transmis à travers le réseau de BQG et à travers une zone de référence (le substrat de SiC) sur le même échantillon. De plus, des observations de l'état de surface de la référence, sur l'échantillon de GEM initial après le procédé de lithographie/gravure, montrent que son aspect est différent d'un substrat de SiC sur lequel aucune croissance de graphène n'a été effectuée.

Afin d'améliorer la précédente mesure, le montage expérimental a d'une part été optimisé. D'autre part, un autre réseau de BQG a été fabriqué (noté C2) à partir d'un GEM contenant un nombre de couches de graphène plus modéré afin de réduire la modification de l'état de surface du SiC, qui provient du procédé de croissance épitaxial. Ce nouvel échantillon C2 présente lui aussi un large pic d'absorption autour de 6 THz à basse température et température ambiante. L'absorption est plus grande à basse température. Un résultat important est que la réponse d'un réseau de BQG aux fréquences THz est très différente de celle d'un GEM. C'est de plus la première fois, à notre connaissance, que la transmission d'un réseau de BQG est mesurée expérimentalement aux fréquences THz. Pour démontrer la validité des résultats, de nouvelles mesures sont réalisées en utilisant comme référence un substrat de SiC sur lequel aucune croissance de graphène n'a été effectuée. Les mesures de transmittance avec les deux types de référence se superposent de manière remarquable, ce qui élimine d'une part les possibles biais expérimentaux, et d'autre part confirme que la réponse observée ne provient pas du substrat de SiC mais bien du réseau de BQG.

Enfin, les mesures expérimentales des échantillons C1 et C2 sont comparées au modèle théorique du Chapitre 1. Des mesures de spectroscopie THz sur les échantillons de GEM avant le processus de lithographie, couplées à des mesures de magnétospectroscopie permettent d'obtenir la constitution des échantillons C1 et C2 : nombre de couches ainsi que leur niveau de dopage. Ces paramètres permettent de modéliser finement la probabilité d'absorption d'une BQG multicouches, et la formule de Tinkham permet de relier cette quantité à la transmittance mesurée expérimentalement. La modélisation théorique reproduit assez fidèlement les mesures expérimentales. Les différentes contributions des couches dopées/non dopées en fonction de la température sont mises en lumière en faisant varier différents paramètres de la modélisation, comme par exemple le temps de vie des niveaux électroniques.

Dans la dernière partie du chapitre, on s'intéresse à la dynamique des porteurs de charge excités. Afin de pouvoir mesurer le temps de vie des niveaux électroniques des BQG, une ligne de pompe optique - sonde THz a été implémentée sur le montage intial de THz-TDS. La variation de transmission du signal THz des échantillons de BQG, induite par une excitation optique, est a priori faible. Dans le but d'extraire ces petits signaux, il important d'avoir un rapport signal à bruit élevé. Le signal est donc obtenu par détection homodyne en utilisant un mixeur de fréquence développé au laboratoire, ce qui permet d'obtenir un rapport signal à bruit élevé. La dynamique des porteurs hors équilibre dans du graphène multicouches est obtenue, et le résultat est consistant avec la littérature. Plusieurs tentatives de mesures ont été réalisées sur les BQG. De très petits signaux ont été mesurés et sont en cours d'optimisation afin d'extraire la dynamique des porteurs de charge. En conclusion, nos mesures et analyses montrent que des transitions aux fréquences THz peuvent être induites dans BQG à basse température et à température ambiante et que leurs propriétés peuvent être ajustées par le dopage et la taille des BQG. Par conséquent, les BQG de diamètre de quelques dizaines de nanomètres sont des nanomatériaux très attractifs pour le développe-

ment de dispositifs THz tels que les lasers THz compacts et les détecteurs THz à faible bruit.

Le **Chapitre 3** est dédié à la mesure du transport quantique électronique dans une boîte quantique unique de graphène, ainsi qu'à la mesure du photo-transport sous illumination de photons THz non-cohérents. Ce projet a été réalisé en étroite collaboration avec Takis Kontos et Sébastien Balibar (groupe de Physique mésoscopique au LPENS).

L'objectif de ce travail est de s'affranchir de la dispersion en diamètre des BQG constituant les réseaux étudiés dans le chapitre précédent, en s'intéressant à une BQG unique. L'étude permet également d'obtenir d'autres informations sur les propriétés électroniques et optiques d'une BQG de plusieurs dizaines de nanomètres. Dans un premier temps, on présente le procédé de fabrication d'une boîte quantique de graphène insérée dans un transistor à électron unique et couplée à une antenne THz en forme de noeud papillon. La BQG ainsi que les électrodes qui l'entourent sont constitués d'une monocouche de graphène entièrement encapsulée par des couches de nitrure de bore hexahonal (hBN). La monocouche de graphène est obtenue par exfoliation mécanique de cristaux de graphite, ce qui permet d'obtenir un graphène de très haute qualité (faible désordre, grande mobilité électronique), ce qui est indispensable pour l'étude d'un BQG unique. Les couches de hBN sont également obtenues par exfoliation mécanique de cristaux de hBN ultra purs. Ces couches protègent le graphène de désordre cristallin, de l'influence électrostatique du substrat (oxyde de silicium sur silicium) ainsi que des contaminations chimiques (qui peuvent doper le graphène) lors de la fabrication. L'hétérostructure est réalisée en contrôlant la température lors de l'assemblage ("hot pick-up technique"). Des mesures de transport électronique sur un premier échantillon permettent d'observer des effets de confinement quantiques dans la BQG, mais ces mesures sont limitées par la géométrie de l'échantillon. Après optimisations, un deuxième échantillon est fabriqué. Il est constitué d'une BQG encapsulée, de diamètre 150 nm, reliée aux électrodes (source et drain) par des contacts étroits d'environ 40 nm de largeur.

Après avoir décrit le protocole de fabrication, on présente le principe de la mesure d'un transistor à électron unique, puis les résultats expérimentaux de spectroscopie par transport électronique. La BQG unique est modélisée par un système d'énergies discrètes, et est couplée de manière capacitive aux différentes électrodes qui l'entourent. En appliquant une tension entre la source et le drain, un électron unique peut être injecté dans la BQG par effet tunnel, et le courant est mesuré. Une électrode latérale, qui joue le rôle de grille, permet d'ajuster le potentiel chimique de la BQG et ainsi contrôler le transport dans la boîte. Le transport est aussi contrôlé par l'énergie de charge, qui décrit la répulsion Coulombienne des électrons dans l'hétérostructure. Les différents paramètres du système sont ajustés de sorte que le transport soit dominé par la répulsion Coulombienne, c'est-à-dire un transport électronique dans le régime du blocage de Coulomb.

L'échantillon est placé dans un cryostat à accès optique (fermé dans un premier temps) et refroidit à très basse température (170 mK). Les mesures de la conductivité différentielle en fonction de la tension drain-source et de grille permettent d'obtenir ce qu'on appelle un diagramme de stabilité de Coulomb. On y observe des zones en forme de diamant, appelé diamants de Coulomb, où le courant est nul. Les diamants de Coulomb sont caractéristiques du régime de blocage de Coulomb, et représentent les conditions dans lesquelles le transport électronique dans la BQG est bloqué, et où le nombre d'électrons dans la boîte est fixé. Les dimensions de ces diamants permettent d'extraire les capacités électriques des éléments du système d'une part, ainsi que l'énergie nécessaire pour ajouter un électron dans la boîte. Cela permet d'évaluer l'énergie de charge de la BQG à environ 7.3 meV. Cette valeur est inférieure à l'énergie de charge estimée dans le cas du modèle d'un disque métallique, ce qui indique que l'encapsulation par des couches de hBN permet de réduire le couplage capacitif de la

boîte avec les électrodes environnantes. La faible température et la très grande stabilité des diamants de Coulomb permettent également d'observer directement des résonances autour des diamants, provenant du transport des électrons par effet tunnel dans les états excités de la BQG. On mesure une séparation en énergie entre états excités de 1.7 meV, soit 0.42 THz. Ce résultat confirme que des grandes BQG (150 nm de diamètre) conduisent à une discrétisation de ses niveaux électroniques de l'ordre du meV, et donc dans la gamme spectrale THz.

Par la suite, on ouvre l'accès optique afin d'étudier l'effet d'une illumination THz sur le transport électronique. L'échantillon est soumis à des photons THz non-cohérents. Dans un premier temps, on s'intéresse à la différence de courant dans la BQG avec et sans illumination lorsque la tension source-drain est fixe. On observe qu'un rayonnement THz de $\sim$ 10 pW induit une différence de courant dans la BQG de l'ordre du nanoampère. Lorsque la tension source-drain varie, on observe que les photons THz induisent une renormalisation du potentiel chimique de la BQG de $\sim$0.15 meV. Cet effet physique de très faible énergie est clairement observable en raison de l'extrême résolution à haute énergie du dispositif expérimental à très basse température, et montre qu'une BQG répond de manière ultra-sensible à une excitation THz. Dans un second temps, on étudie l'origine physique de la renormalisation du potentiel chimique de la BQG. Les modélisations de l'absorption des photons THz par notre système, ainsi que de la température des électrons montrent l'absence d'effet thermique du rayonnement THz dans le régime de blocage de Coulomb. La renormalisation du potentiel chimique de la BQG est donc attribuée à un effet de "photogating' de surface: les photons THz induisent des paires électron-trou dans le substrat de silicium. Le champ électrique sépare ces paires, et des trous s'accumulent à l'interface oxyde de silicium/silicium, ce qui conduit à un décalage de la tension de grille sur la BQG et donc à une renormalisation du potentiel chimique de la boîte. Lorsque l'on mesure cette renormalisation ainsi que le photocourant en fonction de la puissance THz incidente, on observe une évolution non-linéaire, ce qui appuie notre hypothèse. Enfin, des mesures sont en cours afin d'étudier le transport d'électrons par effet tunnel assisté par des photons THz cohérents. En raison de leur grande photo-sensibilité aux fréquences THz, les large boîtes quantiques de graphène sont très prometteuses pour le développements d'émetteurs et détecteurs THz.